EFFECT OF PROCESS VARIABLES ON RESIDUAL STRESS AND MICROSTRUCTURE IN LASER ADDITIVE MANUFACTURING OF γ-TiAl ALLOY

Thesis

Submitted in partial fulfillment of the requirements for the degree of

DOCTOR OF PHILOSOPHY

by

MALLIKARJUNA

DEPARTMENT OF MECHANICAL ENGINEERING

NATIONAL INSTITUTE OF TECHNOLOGY KARNATAKA,

SURATHKAL, MANGALURU – 575 025

OCTOBER, 2020

D E C L A R A T I O N

I hereby *declare* that the Research Thesis titled **" EFFECT OF PROCESS VARIABLES ON RESIDUAL STRESS AND MICROSTRUCTURE IN LASER ADDITIVE MANUFACTURING OF γ-TiAl ALLOY"** which is being submitted to the **National Institute of Technology Karnataka, Surathkal** in partial fulfillment of the requirements for the award of the Degree of **Doctor of Philosophy** in the **Department of Mechanical Engineering** is a *Bonafide report of the research work carried out by me.* The material contained in this Research Thesis has not been submitted to any University or Institution for the award of any degree.

Register Number   : **145087 ME14F10**

Name of the Research Scholar   : **MALLIKARJUNA**

Signature of the Research Scholar :

<div align="center">

Department of Mechanical Engineering

NITK, Surathkal

</div>

Place: Surathkal

Date: 26/10/2020

C E R T I F I C A T E

This is to *certify* that the Research Thesis titled **"EFFECT OF PROCESS VARIABLES ON RESIDUAL STRESS AND MICROSTRUCTURE IN LASER ADDITIVE MANUFACTURING OF γ-TiAl ALLOY"** submitted by **Mr. MALLIKARJUNA (Register Number: 145087 ME14F10)** as the record of the research work carried out by him, is *accepted as the Research Thesis submission* in partial fulfillment of the requirements for the award of degree of **Doctor of Philosophy.**

Research Guides

Dr. Srikanth Bontha   **Dr. Prasad Krishna**

Associate Professor   Professor

Department of Mechanical Engineering

NITK, Surathkal

Chairman - DRPC

Date:

ACKNOWLEDGEMENTS

(**MALLIKARJUNA**)

ABSTRACT

Laser Metal Deposition (LMD) is used to fabricate intricate three-dimensional parts from metal powder by fusing material in a layer-by-layer manner of a digital Computer Aided Drawing (CAD) model. LMD process employed for processing of various materials such as metals, alloys, functionally graded materials, and repairing purpose. The LMD process involved numerous process conditions, mainly laser power, travel speed, and the powder flow rate. Effect on a layerwise variation of melt pool size, thermal cycle, the cooling rate is required to understand for producing a successful sound part. Experimentally determination of the effect of these process conditions on melt pool, thermal cycle, the cooling rate is extremely difficult. A remedy is to achieve a quantitative understanding of the process through computational modeling approaches. In this work, Laser Engineered Net Shaping (LENS), one of the LMD techniques is used to fabricate inherently brittle γ-TiAl alloy thin-wall structures at various processing conditions. These deposits are expected to develop residual stresses due to the rapid heating and cooling cycles involved in the LMD process. Towards this end, a 3-D nonlinear thermomechanical finite element analysis is performed to simulate the process under various process conditions. A commercially available ANSYS software utilized in conducting a sequentially coupled thermomechanical analysis. The melt pool, thermal gradients, and residual stresses are predicted from the developed FE models. Results indicate that laser absorption coefficient (α_A) of γ-TiAl is obtained by a laser surface melting study, and an α_A value is 0.13.

The simulated thin-wall results show that thermal gradients increased with an increase in the number of deposited layers i.e., from the substrate to the last layer. Cooling rates decreased with increase in the number of deposited layers i.e., from the substrate to the last layer. Along the build direction, tensile stresses are generated at the edges and compressive stresses are generated at the centre region of the thin-wall which increase with increase in distance from the substrate. Along the laser travel direction maximum compressive stresses are observed at the centre of the wall and these stresses decrease

in magnitude with increase in distance from the centre. Higher laser power input yields higher residual stresses due to high-thermal gradients, and hence, laser power has a significant impact on the development of residual stresses in the thin-walls. Residual stresses in the deposited thin-wall samples are measured using the X-ray diffraction technique. Reasonable agreement observed between the predicted and measured values of residual stresses.

The microstructure, phases, and hardness of the LMD γ-TiAl alloy thin-walls are also analyzed. The microstructure analysis shows fine lamellar structure comprised of γ and α_2 phases, which are matches with the existing studies. Microhardness in the bottom area is found higher than the middle and top areas of the thin-wall. The hardness values increased marginally (5%) with the increase in travel speed.

Further, melt pool dimensions (length, width, and depth) increased with increase in laser power and decreased with increase in travel speed. During deposition of a layer (which consists of six tracks) the maximum temperature in the melt pool is observed in track 1. Maximum tensile residual stresses are observed in track 1 and these are lower than the yield strength of the material. The magnitude of these stresses decreased from track 2 to 6. Trends of residual stress are found to be independent of the scan strategy (Unidirectional and bidirectional) considered in this study. The state and magnitude of residual stress distribution in the thin-walls and plate are attributes to the transient thermal gradients encountered during deposition.

CONTENTS

LIST OF FIGURES

x

LIST OF TABLES

ABBREVIATIONS

Al- Aluminium

AM- Additive Manufacturing

APDL- ANSYS Parametric Design Language

ASTM- American Society for Testing and Materials

BCC- Body Centered Cubic

BSE-Back-scattered Electrons

Cr- Chromium

CR- Cooling Rates

CP- Commercially Pure

DLF-Direct Laser Fabrication

EBM-Electron Beam Melting

EBF^3-Electron Beam Freeform Fabrication

EIGA- Electrode Induction Melting Gas Atomization

EPMA -Electron Probe Micro Analyzer

FCC- Face Centered Cubic

GE- General Electric

HCP- Hexagonal Closed Packed

HIP- Hot-Isostatic Pressing

HPT- High Pressure Turbine Blades

IM- Ingot Metallurgy

LMD- Laser Metal Deposition

LENS- Laser Engineered Net Shaping

LPT - Low Pressure Turbine Blades

LOM-Laminated Object Manufacturing

L1- L2: Layer 1 to Layer 2

MIM-Metal Injection Molding

MS- Magnetic Sputtering

MPD_c- Melt Pool Depth at The Centre

MPD_e-Melt Pool Depth at The Edge

MPL_c-Melt Pool Length at The Centre

MPL_e-Melt Pool Length at The Edge

Nb- Niobium

OM- Optical Microscopy

PM- Powder Metallurgy

P1- First Principal Stress

RP-Rapid Prototyping

RS- Residual Stress

SEM- Scanning Electron Microscopy

SLM- Selective Laser Melting

SLA-Stereolithography Apparatus

SPS- Spark Plasma Sintering

SE- Secondary Electron

TEM- Transmission Electron Microscopy

Ti- Titanium

Ti-48Al-2Cr-2Nb- (48-2-2)

γ-TiAl- Gamma Titanium Aluminide-Intermetallic Compound

Ti_3Al- Titanium Aluminide-Intermetallic Compound

TG Temperature Gradient

T1-T6: Track 1 to Track 6

VM- Von Mises Stress

XRD- X Ray Diffraction

NOMENCLATURE

ρ Density

C_p Specific Heat

k Thermal Conductivity

$\dot{q}$ Rate of Heat Generation

L_f Latent Heat fusion

E Young's Modulus

μ Poisson's Ratio

σ_s Yield Strength

α Coefficient of Thermal Expansion

α_A Laser Absorption Coefficient

γ Gamma Phase, Face-Centred Tetragonal Structure in TiAl

α_2 Alpha 2 Phase, Hexagonal Structure in Ti_3Al

CHAPTER 1

1   INTRODUCTION

1.1   Background

Additive manufacturing (AM) is a relatively new technology as the first AM processed "Stereolithography" was developed in the year 1986. In the early stages of its development, it was primarily referred to as "Rapid Prototyping" technology. This is because, in the initial stages, it was predominantly used for producing prototypes for visualization and proof of concept models. In the last three decades, several new technologies were developed at different places and were referred to by different names such as Layer Manufacturing, Desktop Manufacturing, Rapid Manufacturing, 3D printing, etc. Continuous research and development has resulted in the development of AM technologies that can now produce fully functional parts for load-bearing applications.

In spite of these continuous developments of the AM processes, there was no effort for standardization until the year 2009. In 2009, the ASTM F42 Committee was formed to develop standards for additive manufacturing.

According to the Committee, additive manufacturing is defined as:

"*A process of joining materials to make objects from 3D model data, usually layer upon layer as opposed to traditional processes based on subtractive manufacturing technologies*".

1.2   Classification of AM processes

The ASTM F42 Committee classified all the AM processes into seven different categories, as given in Table 1.1.

Table 1.1 Classification of AM processes (Gao et al. 2015)

CATEGORIES	TECHNOLOGIES	PRINTED "INK"	POWER SOURCE	STRENGTHS / DOWNSIDES
Material Extrusion	Fused Deposition Modeling (FDM)	Thermoplastics, Ceramic slurries, Metal pastes	Thermal Energy	• Inexpensive extrusion machine • Multi-material printing • Limited part resolution • Poor surface finish
	Contour Crafting			
Powder Bed Fusion	Selective Laser Sintering (SLS)	Polyamides /Polymer	High-powered Laser Beam	• High Accuracy and Details • Fully dense parts • High specific strength & stiffness • Powder handling & recycling • Support and anchor structure • Fully dense parts • High specific strength and stiffness
	Direct Metal Laser Sintering (DMLS)	Atomized metal powder (17-4 PH stainless steel, cobalt chromium, titanium Ti6Al-4V), ceramic powder		
	Selective Laser Melting (SLM)			
	Electron Beam Melting (EBM)		Electron Beam	
Vat Photopolymerization	Stereolithography (SLA)	Photopolymer, Ceramics (alumina, zirconia, PZT)	Ultraviolet Laser	• High building speed • Good part resolution • Overcuring, scanned line shape • High cost for supplies and materials
Material Jetting	Polyjet / Inkjet Printing	Photopolymer, Wax	Thermal Energy / Photocuring	• Multi-material printing • High surface finish • Low-strength material
Binder Jetting	Indirect Inkjet Printing (Binder 3DP)	Polymer Powder (Plaster, Resin), Ceramic powder, Metal powder	Thermal Energy	• Full-color objects printing • Require infiltration during post-processing • Wide material selection • High porosites on finished parts
Sheet Lamination	Laminated Object Manufacturing (LOM)	Plastic Film, Metallic Sheet, Ceramic Tape	Laser Beam	• High surface finish • Low material, machine, process cost • Decubing issues
Directed Energy Deposition	Laser Engineered Net Shaping (LENS) Electronic Beam Welding (EBW)	Molten metal powder	Laser Beam	• Repair of damaged / worn parts • Functionally graded material printing • Require post-processing machine

Only the processes relevant to the current research work (directed energy deposition) will be described in brief in the following sections.

1.3 Directed Energy Deposition

From a 4 or 5 axis servo control nozzle material powder or wire fed into the surface of the substrate where material is melted using laser, electron beam or plasma upon deposition. Directed Energy Deposition (DED) includes Laser Engineered Net Shaping (LENS), Direct Metal Deposition (DM3D) technology, Electron Beam Freeform Fabrication (EBF3), etc. In this thesis, all the laser based DED processes will be considered, henceforth referred to as Laser Metal Deposition (LMD) processes.

1.3.1 Laser Metal Deposition

Laser Metal Deposition (LMD) or LENS is a technology to fabricate three-dimensional metallic components directly from CAD solid models. The LMD has the potential to process a variety of metals. The schematic arrangement of the LMD is shown in Figure

1.1. The process starts with a high-intensity Nd: YAG laser beam, which targets a tiny spot on the metal substrate producing a molten pool. Then from either side of the laser nozzles, a precise amount of metal powder is blown into the melt pool to increase the size of the material.
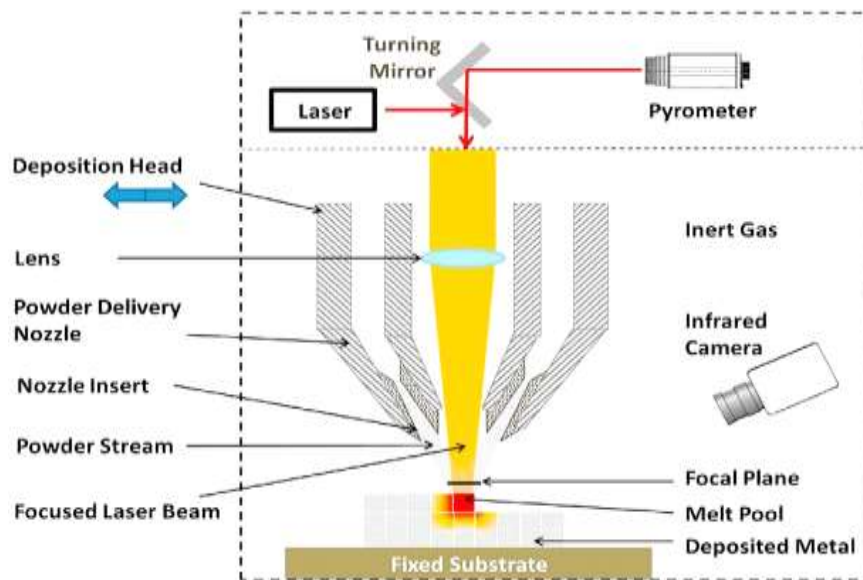
Figure 1.1 Schematic of LMD process (Azarniya et al. 2019)

The laser beam builds the part layer-by-layer according to the CAD model as the system moves the substrate under the beam in the XY plane, and the material deposition head moves up one-layer thickness in the Z direction. This lasing and powder deposition process is repeated until the generated tool path is completed. The action takes place in a sealed chamber, where the restricted environment variables can be tightly controlled. The oxygen level controlled should be less than 10 ppm in an argon atmosphere.

1.3.2 Advantages of LMD process

The LMD process can be used to produce near net shape components with good metallurgical properties. It can also be used to repair and recondition expensive items such as jet engine components. It is possible to control the shape, size, and internal architecture of the components and obtain a fine-grained homogeneous microstructure. The wastage of material is minimal and can be recycled. This process helps for green, clean manufacturing because the machine operates in a controlled environment and produces less residue.

3

1.3.3 Disadvantages of LMD process

The LMD process can build parts with overhangs and undercuts with the help of a support structure that may cause secondary operations. The built part needs to be cut from the substrate and may lead to damages. Additional machining is required to finish the rough surfaces. The LMD machines are generally expensive and involve high maintenance costs.

1.3.4 Materials

The LMD process can be applied to fabrication of components from a wide variety of metals and alloys, nickel-base superalloy (Inconel designations 625, 600, 718, 690), Stainless steels alloys (316, 303L, 309), Ti alloys and tool steels. All of which are commercially available in powder form. Hereafter, the term LENS and LMD will be interchanged in this thesis.

1.3.5 Applications of LMD process

The LMD process can be used to fabricate a variety of metal and alloy components. For example, the fabrication of titanium and other exotic metal parts for aerospace applications. It can repair by precisely adding the material to worn or damaged blisk and any other complex parts to restore their profile. On-demand, a wear-resistant coating for industrial components and medical devices. The LMD process is a metallurgical playback and can be used for new material development.

1.4 Titanium and its alloys

William Gregor, the mineralogist and chemist discovered titanium (Ti). It is classified as a non-ferrous and light metal. It has a low density (4510 kg/m^3) and a high melting point (1668 °C) (Leyens and Peter 2003). It is not available in pure form, and its extraction process makes the metal expensive. It has gained significant attention in several applications due to its high strength and excellent corrosion resistance. At present, the aerospace industry is still the primary consumer of titanium and its alloys, while in other areas such as architecture, chemical, biomedical, power generation, marine and offshore, sports, leisure, and transportation, the usage of titanium and its alloys is continually growing.

At low temperature, Ti has a Hexagonal Closed Packed (HCP), commonly referred to as α titanium, while at high temperatures, it has a BCC structure, referred to as β titanium. The complete transformation from one crystal structure into another is called allotropic transformation. The respective transformation temperature is called the transus temperature. The β-transus temperature for pure titanium is 882±2 ℃.

1.4.1 Classification of titanium alloys

Titanium alloys are classified based on β transus temperature as α alloys, β alloys, α+β alloys and Intermetallics. Apart from the alpha and beta phases other phases are also present, which are called intermetallics. At low volume fractions of β-eutectic elements such as Cr, Nb, Fe and Si can lead to formation of intermetallic compound (Leyens and Peter 2003). Present research work focused on intermetallic based titanium aluminide (TiAl) alloy. The details of intermetallic TiAl is presented in the following subsection.

1.4.1.1 α-alloys

Alpha alloys are single-phase alloys. Elements such as Al, O, stabilize the α-phase and are called alpha stabilizers. Alpha alloys exhibit high corrosion resistance. These alloys are non-heat-treatable and are easily weldable. Applications of these alloys are in chemical and process engineering industry. Commercially pure (CP) Ti and Ti-5Al-2.5Sn are the most important alloys of this class. Alpha alloys exhibit medium strength, reasonably fairly ductility and excellent mechanical properties at very low temperatures.

1.4.1.2 β-alloys

In beta alloys, the β phase is stabilized at room temperature by the addition of ~30% of β stabilizers such as Nb, Ta, V, Mo, etc. The β alloys are employed in burn-resistant applications. Ti-10V-2Fe-3Al, Ti-15Mo, and Ti-13V-11Cr-3Al are some of the prominent alloys of this class. These alloys exhibit high strength, excellent formability, and is heat treatable and weldable (Joshi 2006).

1.4.1.3 α+β alloys

Alloys containing 4 to 6% of beta stabilizers are called α+β alloys. If the proportion of the β-stabilizing elements is increased, then β no longer changes to martensite upon

rapid quenching, and the alloys will still be in the two-phase field, and a class of metastable β alloys are developed. Examples of α+β alloys include Ti-6Al-4V and Ti-6Al-6V-2Sn. The aerospace industry is the largest consumer of Ti-6Al-4V alloy.

1.4.1.4 Intermetallics

Gamma-Titanium Aluminides (γ-TiAl) fall within the category of materials referred to as intermetallics. Intermetallics are compounds formed from two different metals. Their crystal structure and properties are totally different from their parent metals. During the formation of an intermetallic alloy, a long-range ordering is developed within material. Long-range ordering means they have a regularly repeating pattern and places constraints on the deformation modes. These constraints result in increased strength (at high temperatures) and fracture toughness (Appel et al. 2011). γ-TiAl material exhibits low ductility at room temperature and hence processing is a challenging task (Appel et al. 2011).

In the recent past, TiAl has received a lot of attention because of the following properties:

1. High melting point,
2. Low density,
3. High elastic modulus,
4. Good structural stability, and
5. Good oxidation and corrosion resistance.

The γ-TiAl based Ti-48Al-2Cr-2Nb alloy is developed and certified by GE and used in their turbofan engines (Kelly et al. 2003). Figure 1.2 (a) and (b) show how the specific modulus and specific strength of γ-TiAl alloys compare with other materials. The high specific modulus and strength of γ-TiAl alloys is the reason for its wide range of applications in automotive and aerospace industries (Appel et al 2011).
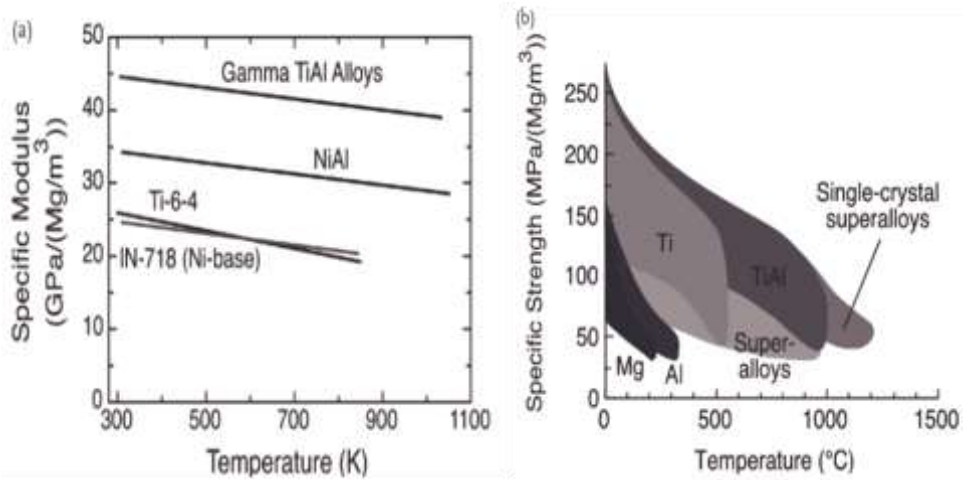
Figure 1.2 Graphs showing the (a) Specific modulus, and (b) Specific strengths of γ-TiAl alloys (Appel et al. 2011)

1.4.1.5 Phase diagram

The binary TiAl phase diagram and crystal structure for α_2-Ti_3Al and the crystal structure for γ-TiAl are shown in Figure 1.3. Titanium aluminide (TiAl) is an intermetallic chemical compound that comprises of several phases, which include: α_2-Ti_3Al, γ-TiAl, $TiAl_2$ and $TiAl_3$. Among these phases only α_2-Ti_3Al, γ-TiAl phases have got technical importance. $TiAl_2$ and $TiAl_3$ phases are highly brittle in nature (Kothari et al. 2012). Current research work deals with the α_2-Ti_3Al, γ-TiAl phases.
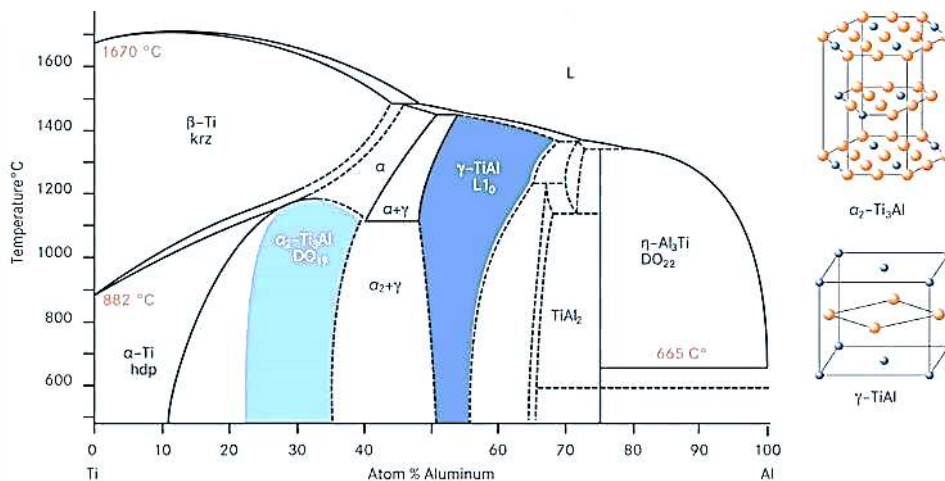
Figure 1.3 Ti-Al phase diagram (Schuster and Palm 2006)

1.4.1.6 Microstructure of γ-titanium aluminide

In γ-TiAl alloy, phases vary with Al composition. If the Al composition is between 46-52 (at. %), the microstructure consists of either a single-phase microstructure (γ phase) or a two-phase system (γ and α_2 phase). In γ-TiAl, the different microstructures that are formed are equiaxed, duplex and lamellar depending on the cooling rates and post-heat treatments (Franzen 2010).

a. Equiaxed

Equiaxed microstructure is formed, as shown in Figure 1.4 (a). It comprises of a single-phase and has good high-temperature properties and low density. However, at room temperature, it has poor fracture toughness and low ductility. Hence, it is not suitable for structural applications (Franzen 2010).

b. Duplex

The duplex microstructure, as shown in Figure 1.4 (b). Duplex microstructure is formed at right amount of Al concentrations i.e. 45-51 at % in the phase diagram. Duplex microstructure consists of two phases: α_2 and γ and the average grain size is about 10 μm (Franzen 2010).
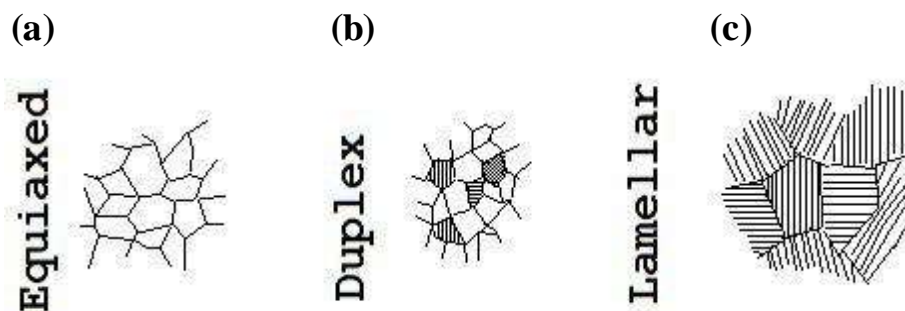
Figure 1.4 Microstructure of the γ-TiAl alloys (a) Equiaxed (b) Duplex (c) Lamellar (Franzen 2010)

c. Lamellar

The lamellar microstructure is columnar in nature, as shown in Figure 1.4 (c). This microstructure is formed by alternating γ and α_2 phases stacking up into lamellae. The lamellar structure is more ductile than the equiaxed microstructure. It will give good ductility if the grain size varies between 10-30 μm (Franzen 2010).

1.4.1.7 Applications of γ-TiAl

γ-TiAl alloys has high specific strength and specific modulus and hence are used in aerospace and automotive sectors (Appel et al. 2011). For example, lower-pressure turbine (LPT) and high-pressure turbine (HPT) blades, stator vanes, combustor casings, radial diffusers, exhaust components, turbocharger wheel etc. are made from these alloys.

1.5 Conventional manufacturing techniques of γ-TiAl alloys

Conventional manufacturing techniques such as casting and powder metallurgy methods are used to produce γ-TiAl parts. Some of the limitations of the casting and powder metallurgy methods are as follows.

Limitations of the ingot metallurgy process:

1. Large coarse columnar grains,
2. Chemical inhomogeneity and segregation,
3. Time and cost for finishing the γ-TiAl part is high,
4. High thermomechanical heat treatment temperature which ranges from 1200 to 1350 °C,
5. Centerline porosity, and
6. Regions of varying density and microstructure.

Limitations of the powder metallurgy process:

1. Presence of impurities in the powders will form interstitial elements leading to porosity,
2. The Hot Isostatic Pressing requires exposures to high temperatures for several hours, which can lead to grain growth,
3. Porosity and contamination,
4. During gas atomization, the liquid metal interacts with the inert gas environment leading to the entrapment of the gas within the particles as spherical pores, and
5. A series of post-processing operations are required to finish the final part.

Processing of γ-TiAl materials using any of the above conventional manufacturing processes is difficult and a series of secondary operations are required to obtain desired

microstructure and mechanical properties (Kothari et al. 2012). These processes also induce harmful tensile residual stresses. Further, Laser Metal Deposition processes develop residual stresses due to rapid heating and cooling cycles (Zhang et al. 2001). These residual stresses must be measured to prevent premature failures or to ensure safe operation of components. Hence, a brief introduction to residual stress and its measurement are discussed in next section.

1.6 Residual stress and its measurements

Residual stresses are locked-in stresses present in the engineering components, even when there is no external load. These develop primarily due to non-uniform volumetric change in the manufacturing processes (machining, mechanical deformation, casting, welding, coating, heat treatment, etc.). When the developed residual stress exceeds the yield strength, it leads to plastic deformation.

Residual stress can be tensile or compressive depending on the location and type of non-uniform volumetric change taking place due to differential heating and cooling during processes like welding and heat treatment. Compressive residual stresses are sometimes intentionally induced to enhance the mechanical properties, while tensile residual stresses are harmful to the component and need to be relieved.

Thermal stress can be caused by restricting thermal expansion. Thermal stress can be calculated as,

$$\sigma = E\,\varepsilon$$

$$\sigma = E\,\alpha\,dt \tag{1.1}$$

Where σ is the stress due to thermal expansion (N/m^2), E is Young's modulus of the material (N/m^2), ε is the strain, α is the thermal expansion coefficient of the material, and dt is the temperature difference.

1.6.1 Effect of residual stress

The Residual stress, whether tensile or compressive, predominantly affect the soundness, dimensional stability, mechanical performance and may cause premature failures (Withers and Bhadeshia 2001). Hence, measurement of residual stresses in the

body is necessary. The next section discusses about various destructive and non-destructive techniques available to measure the residual stresses in the parts.

1.6.2   Measurement techniques

Measurement of residual stresses is challenging because of their in-component locked-in character. Stresses are caused by external loads, while measurements are indirect such as strain or displacement measurement. Then stresses are subsequently interpreted. A typical procedure of comparative measurements is used on the structure with and without external load and then evaluated based on the difference between the two measurements. Techniques used to measure residual stress are broadly categorized as destructive, semi-destructive, and non-destructive, as shown in Figure 1.5. In this work, X-ray diffraction technique was used to measure residual stress present in the LMD of γ-TiAl samples.
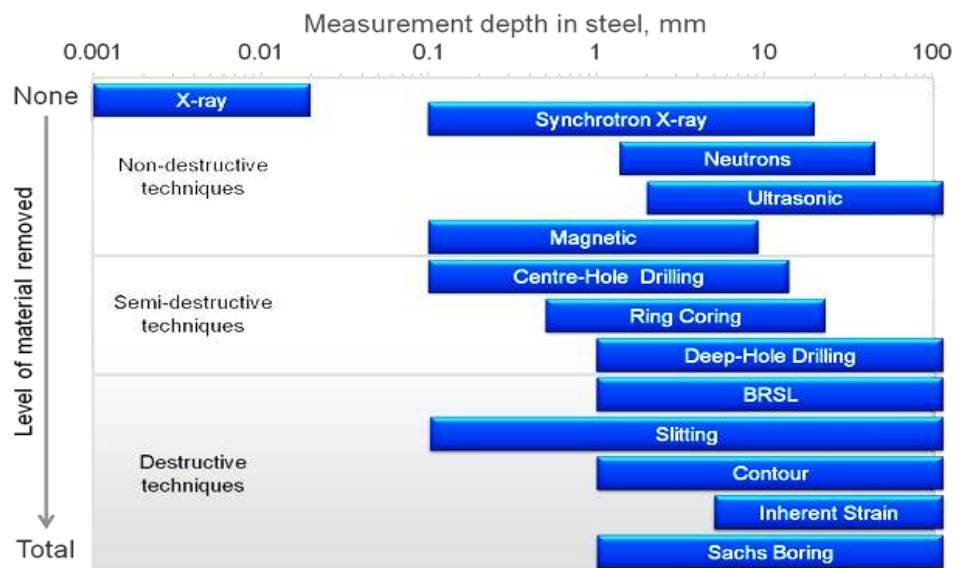
Figure 1.5 Comparing of residual stress measurement techniques (Schajer 2013)

1.7   Layout of thesis

This thesis is divided into eight chapters the details are hereunder:

Chapter 1 presents an introduction to the thesis;

Chapter 2 includes a critical review of the published literature relevant to the current research. The literature review focuses on conventional manufacturing of γ-TiAl alloys, additive manufacturing of γ-TiAl alloys, and thermomechanical modeling and measurement of residual stresses in LMD parts;

Chapter 3 presents the numerical modeling procedures used for simulating the deposition of γ-TiAl thin-wall and plate geometries using LMD. This chapter also includes the numerical modeling procedures used for the evaluation of laser absorption coefficient that was determined by laser surface melting;

Chapter 4 describes the experimental methodology used for the deposition of the samples, microstructural analysis and measurement of residual stresses in the deposited samples. Also, the experimental work carried out as part of the laser surface melting study to estimate α is presented;

Chapter 5 presents and discusses the results of the laser surface melting study. Results of the both numerical modeling and experimental studies are discussed in the sub-sections;

Chapter 6 presents and discusses the results of the numerical and experimental study of laser metal deposited γ-TiAl alloy thin-wall structures;

Chapter 7 presents and discusses the results of the numerical modeling of the laser metal deposited γ-TiAl alloy plate geometries;

Chapter 8 presents conclusions and future work of the present research.

CHAPTER 2

2   LITERATURE SURVEY

This chapter presents a literature review on the following topics:

1. Conventional manufacturing of γ-TiAl alloys
2. Additive manufacturing of γ-TiAl alloys
3. Thermomechanical modeling and measurement of residual stresses in LMD parts.

2.1   Conventional manufacturing of γ-TiAl alloys

Sakamoto et al. (1992) studied the contamination in TiAl ingots using three different melting processes, such as vacuum induction, cold crucible induction and electron beam melting (EBM). This study reported that vacuum induction increased the oxygen contamination in the ingot; there was no change in oxygen contamination with cold crucible induction and EBM showed decreased oxygen contamination due to Al evaporation. However, combined process of electron beam-cold crucible melting (EBM-CCM) gave a homogeneous ingot having low oxygen and thereby is suitable for producing the cleanest TiAl ingots. Loretto et al. (2005) investigated the traditional manufacturing methods like casting, powder metallurgy etc., for preparing TiAl alloys. Sarkar et al. (2005) investigated the optimum process parameters for machining γ-TiAl using wire electric discharge machining. Their goal was to obtain a good surface finish and dimensional accuracy. In this study, they used constrained optimization and Pareto optimization algorithms to optimize the process parameters. Lasalmonie (2006) reviewed the applications of TiAl alloys along with the processing challenges. This study reported that even though casting and powder metallurgy techniques are suitable for fabricating TiAl alloy components, secondary operations are definitely required to obtain desired properties. The secondary operations increase the cost of processing, which limits the applications of this material. Lapin (2009), as discussed that depending on the chemical composition and heat treatments, TiAl alloys exhibit four different types of microstructures: near-gamma, duplex, near lamellar and fully lamellar microstructures.

Wang et al. (2011) investigated the Ti-47Al-2Cr-2Nb-0.2W-0.15B (at.%) alloys fabricated by pre-alloyed powder metallurgy. An electrode induction melting gas atomization (EIGA) was used to produce the pre-alloyed powder, which was then compressed into a rectangular can, and degassed 12h at 450 $^{\circ}$C. These were next hot isostatic pressed for 4h at 1260 $^{\circ}$C/170 MPa and finally heated for 2h at 1280 $^{\circ}$C. The cylindrical specimens were cut using electric discharge machining. Deformation and compression studies revealed the optimum processing conditions. Rao et al. (2011) carried out a study to synthesize TiAl alloy by powder metallurgy. The composition of the TiAl alloy powders is 46Ti-46Al-4Nb-2Cr-2Mn. In this work, the mixing of element powders was followed by hot isostatic pressing (HIP) of the cylindrical specimens. The microstructure and deformation rates in these samples were studied. Kothari et al. (2012) in a review paper, presented a detailed overview of TiAl applications, properties, microstructure and manufacturing challenges and opportunities. This work reported that γ-TiAl alloy displays the properties such as light weight, creep and good oxidation resistance at elevated temperatures. However, low ductility of the material at room temperature results in difficulties in processing the material. This paper also discussed the traditional manufacturing methods such as casting, ingot metallurgy and powder metallurgy. Currently, the PM is a novel method to produce TiAl parts. The problem with PM techniques is post-processing required to obtain the desired microstructure and properties. Thus, increase lead time in manufacturing. However, with advances in manufacturing technologies and a deeper understanding of the microstructure and deformation mechanisms in TiAl, led to the following commercial applications of TiAl alloys. Exhaust valves made of titanium aluminides have been used to replace the existing Ti-6242, Ti-1100, and IMI 834 alloys. The turbocharger wheels made from TiAl alloy, have been prototyped and tested to replace Ni-based superalloys. Semiatin et al. (2012) reported the manufacture of thin-gage material of superalloy and γ-TiAl alloy using magnetic sputtering (MS) and electron-beam physical vapor deposition (EBPVD) processes. MS gives very fine uniform microstructures, a uniform composition in thin-gage γ-titanium aluminide. EBPVD technique has the potential to produce large-plan-area foils of single and two-phase γ-TiAl alloys. Dong et al. (2014) studied the microstructure and tensile properties of Ti-44A-l6Nb-1.0Cr-2.0V alloy ingot manufactured by vacuum consumable melting.

As-cast samples showed micro-cracks, which lead to deterioration of the tensile properties resulting in premature fracture. The addition of Nb, Cr and V can decrease stacking fault energy (SFE) so as to enhance the ductility of the alloy. Kun et al. (2014) reported the powder metallurgy of Ti-45Al-7Nb-0.5W subjected to post thermal treatments such as isochronal annealing and isothermal annealing to refine the microstructure. In this work, they reported no significant change in the microstructure of the alloy with prolonged annealing time. Cegan et al. (2015) studied three TiAl-based alloys with nominal compositions: Ti-47Al-8Nb, Ti-47Al-8Ta, and Ti-47Al--8Ta-0.3Y (at.%). These alloys were prepared by induction melting in graphite crucibles and then centrifugally cast into graphite molds. The graphite crucibles and graphite cast molds showed best microstructure and mechanical properties. Graphite is a good material for both mold and crucibles in the processing of TiAl based alloys. Du et al. (2016) reported the manufacturing of porous titanium aluminide via Spark Plasma Sintering (SPS) and different post processing methods. The spark plasma sintering was conducted at 600 ºC/10 MPa, which was followed by water dissolution to remove the NaCl (space holder to create porous). This was followed by two post-heat treatment: pressure less spark plasma sintering and vacuum annealing utilized to achieve the final porous TiAl. They reported the formation of γ and α_2 phases. Voisin et al. (2015) used the powder metallurgy technique to manufacture γ-TiAl based (Ti48-Al48-Cr2-Nb2) alloy and then used SPS technique to fabricate the near net shape blade. SPS method produced the TiAl turbine blade in a single step without post-treatment and with properties that cannot be obtained using conventional techniques. Castellanos et al. (2018) reported the surface integrity issues such as residual stress, surface cracks and surface roughness induced during machining of TiAl alloy. They have shown that the optimal processing parameters, machining conditions and coolants. Which offers the good machinability and reduce surface defects of TiAl alloys. Wimler et al. (2019) reported the sintering of third-generation alloy (Ti-43.5Al-4Nb-1Mo-0.1B in at. %) using SPS technique. The sintered TiAl samples were analyzed for microstructure. They have found that lamellar colonies comprising of γ and α_2 phases. In another study, Jeje et al. (2019) 52Ti-48Al samples were sintered using SPS method at various temperatures. It was reported that samples have major phases such as $TiAl_2$, Ti and Ti_2Al_5 and minor phases such as γ and α_2.

2.1.1 Summary of literature review on conventional manufacturing of TiAl alloys

The literature survey of the conventional manufacturing techniques used to manufacture γ-TiAl alloys reveals that TiAl alloy is an intermetallic material having low density, high melting point, and good oxidation resistance. Due to low ductility, the processing and machining are cumbersome at room temperature. Many researchers have attempted new processing routes for γ-TiAl alloy to reduce the fabrication cost. One of the biggest drawbacks of the conventional manufacturing techniques (casting, powder metallurgy etc.,) is the need for secondary operations to achieve desired microstructure and properties, which increases cost of processing. Therefore, there is a need to identify new processing routes to fabricate γ-TiAl alloys components.

2.2 Additive manufacturing of γ-TiAl alloys

Dave et al. (1995) used Electron Beam Freeform Fabrication (EBF³) technique to produce large-size complex near net shape parts in minimal time, unlike conventional processes such as casting, forging and machining process. This work reported that EBF³ technique can easily process materials such as reinforced composites, intermetallic compounds, and materials with composition gradients that are difficult to process by traditional means. Liu and DuPont (2004) investigated carbide particle reinforced TiAl matrix composites (TiC & Ti-48Al-2Cr-2Nb) fabricated using Laser Engineered Net Shaping (LENS) technique. Solid-state cracking was reported due to high thermal stresses generated during process. They reported that these cracks can be reduced by preheating the substrate to a temperature in the range of 450-500 ℃. Srivastava (2002) studied the effect of laser process parameters and heat treatments on resulting microstructure in laser-deposited γ-TiAl material (Ti48-Al48-Mn2-Nb2). Micrograph analysis of the samples revealed heterogeneous microstructures. This study reported that laser power and scan speed greatly dominated the microstructure evolution. This study also reported that annealing followed by air cooling ability to produce near net shape TiAl parts. Cormier et al. (2007) utilized Electron Beam Melting (EBM) technique to produce γ-TiAl (Ti-48Al-2Cr-2Nb) samples. They used pre-alloyed powder. It was reported that the EBM process has the ability to produce the near net shape TiAl parts. Qu and Wang (2007) reported the fabrication of γ-TiAl intermetallic

alloy in laser melting deposition process. The microstructure was characterized by OM, SEM and tensile test. It was found that the full dense parts and columnar grain with fully lamellar structure. Further, tensile strength obtained was 650 MPa along the longitudinal direction. Qu et al. (2009), in another study fabricated intermetallic alloys using laser metal deposition process. As-deposited and heat-treated specimens were characterized to understand the microstructure and mechanical properties of deposited components. They reported fully dense columnar grains with a fully lamellar structure.

Murr et al. (2009) studied the Ti-47Al-2Cr-2Nb alloy fabricated by EBM process. Deposited samples were characterized using Scanning Electron Microscope (SEM), Transmission Electron Microscope (TEM) and optical microscope (OM). They reported a large number of dislocations in the TEM images, which contribute to the residual hardness, which is a result of high cooling rates. Further reported that the precursor powder had the HCP Ti_3Al, α_2 rich phase, while the EBM samples displayed FCC γ-TiAl with lamellar colony structure. Loeber et al. (2011) investigated the feasibility of two processing routes Selective Laser Melting (SLM) and Electron Beam Melting (EBM) for TiAl based Ti-(46-48)Al-2Cr-2Nb alloy. This work mainly focused on microstructure and mechanical properties. The study reported that EBM deposited specimens showed a bimodal microstructure. The density up to 99% was achieved by subjecting the EBM samples to hipping. Comparison test results on two processes, EBM produced TiAl parts showed better properties than the SLM process. Porter et al. (2011) fabricated a complex γ-TiAl turbine using EBM technique. They evaluated the microstructure and mechanical properties of EBM produced samples to compare conventional processed parts. They have found that dendritic $\alpha_2+\gamma$ in an as-deposited sample, after the heat-treatment which is transformed to lamellar colonies of fine $\alpha_2+\gamma$. Mahamood et al. (2013) reported the fabrication of Ti alloy using laser metal deposition (LMD). They showed that processing parameters influence greatly on microstructure, hardness and surface roughness in LMD specimens. Ma et al. (2014) investigated the in-situ fabrication of TiAl alloy by feeding the separate wire of Titanium and Aluminum wires in the gas tungsten arc welding (GTAW) process. They successfully produced full density of TiAl samples using GTAW process. Results reveal large microsegregation in different regions. Different regions displayed different

microstructure and properties due to solidification rate and improper feeding system. Filippini et al. (2014) studied the fatigue behavior of Ti-48Al-2Cr-2Nb alloy produced by electron beam melting (EBM). Their study concluded that unfavorable oriented lamellar colonies are responsible for the fatigue failure of the γ-TiAl alloy. Tang et al. (2015) studied the deposition of high niobium TiAl alloy (Ti-47Al-7Nb-0.3W) using EBM technique. They reported microstructural defects due to Al vaporization, which is dependent on the processing parameters. The base was heated to a higher preheating temperature to avoid the micro-macro cracks. The study reported that fabricated samples showed a fine fully lamellar structure and outstanding compression strength. They also concluded that high incident energy causes inhomogeneous microstructure and that processing parameters to be optimized to obtain a desired structure and properties. Balla et al. (2016b) studied Laser Engineered Net Shaping (LENS) technique to fabricate the γ-TiAl alloy samples. They investigated the influence of laser power and scan speed on fabrication ability, microstructure, tribological and corrosion properties of LENS deposited TiAl alloy. Their study reported that low wear rate was demonstrated by specimens at laser power 200 W and scan speed 10 mm/s. The finest corrosion resistance obtained with samples deposited at 350 W and 10 mm/s. They also reported that near net shape and defect-free parts can be produced by using laser incident energy between 40 and 50 J/mm^2. Thomas et al. (2017a) carried out a study to optimize the process parameters for laser metal deposition of Ti-48Al-2Cr-2Nb alloy. They carried out a large number of experiments at different processing conditions under a controlled atmosphere. High cooling rates during cooling induces high residual stresses eventually defect part. They have controlled thermal gradients by adjusting the laser heat source and produced the defect-free parts. The fast cooling rates results in fine grain structure and produce higher hardness. Further, post-heat-treatments of the as-deposited samples obtained the homogeneous structure and relieved residual stresses. Sharman et al. (2018) LENS process used to fabricate TiAl samples under various process conditions. They built crack free intermetallic TiAl parts by changing laser focusing position and thereby controlling of cooling rates during deposition. Tlotleng (2018) studied that in situ alloying of binary Ti and Al elemental powder using LENS technique for deposition of cube samples. It was reported that the as-deposited sample exhibits micropores and cracks. Seidel et al. (2019) studied the effect of surface

roughness in EBM and hybrid LMD processed γ-TiAl (TNM-B1) samples. They have reported that hybrid LMD sample has lesser surface roughness than the EBM sample.

2.2.1 Summary of literature review on additive manufacturing of γ-TiAl alloys

γ-TiAl alloys are difficult to process using conventional techniques due to its low ductility and higher processing cost of secondary operations. Researchers have attempted to fabricate TiAl parts using Additive Manufacturing techniques. AM techniques for the processing of TiAl components include:

1. Selective Laser Melting (SLM),
2. Laser Engineered Net Shaping (LENS),
3. Electron Beam Melting (EBM), and
4. Electron Beam Freeform Fabrication (EBF[3]).

Of these different processes listed above, considerable research work has been reported for EBM fabrication of TiAl alloys. However, very little work has been reported on the laser metal deposition of γ-TiAl alloys. Also, in the case of LMD processes, cracks were reported on as-deposited samples due to development of residual stress exceeding yield strength of the material. Hence, there is a need to systematically analyse thermomechanical behaviour of laser metal deposited γ-TiAl alloys so as to produce defect-free components.

2.3 Thermomechanical modeling and measurement of residual stresses in LMD parts

Dave et al. (1995) reported that modeling of moving volumetric heat source developed to understand and control the EBF3 process by solving Green's function. Griffith et al. (1999) investigated temperature behaviour during LENS deposition of H13 tool steel samples. They measured the temperatures of H13 tool steel samples using a thermocouple, infrared imaging, and high-speed visible imaging. It was found that the significant influence of temperature on microstructure in LENS deposition. Bontha et al. (2006) used a combination of analytical and FEM approaches to investigate the effect of process variables and size-scale in laser deposited Ti-6Al-4V. The analytical approach was based on the Rosenthal solution for a moving point source. This work focused on the development of the thermal process maps to predict the trends in the

solidification microstructure. In this work, the cooling rates and thermal gradients extracted from analytical and FEM approaches were plotted on the existing maps for Ti-6Al-4V. They reported agreement between modeling and experimental results and also concluded that size-scale is important. Ye et al. (2006) carried out the numerical simulation of laser metal deposition process to understand thermal behaviour during deposition. Roberts et al. (2009) used a 3-D finite element model to predict the transient temperature field in each layer during the laser deposition process. They used the element birthing and deathing technique and the laser heat source as Gaussian distribution TEM$_{00}$ mode to simulate multiple layers.

Table 2.1 Different heat source models

Types of heat flux	Heat flux equations
Surface (2D) heat flux	$q(r) = \dfrac{2P}{\Pi r_0^2}\exp\left(\dfrac{-2r^2}{r_0^2}\right)$
	$I(r,w) = \dfrac{2AP}{\Pi w^2}\exp\left(\dfrac{-2r^2}{w^2}\right)$
	$q(r) = \dfrac{4.55P}{\Pi R^2}\exp\left(\dfrac{-4.5r^2}{R^2}\right)$
Volumetric (3D) heat flux	$f_{laser} = \dfrac{A \times I_0(X,Y)}{\delta}\exp\left(\dfrac{-|z-z_{surface}|}{\delta}\right)$

Fu and Guo (2014) studied the effect of the process parameters on melt pool geometry and dimensions during the Selective Laser Melting (SLM) process. An element activation and deactivation method was used to simulate the physical build-up of the geometry layer-by-layer. They also reported various heat flux models (as shown in Table 2.1) using in the simulation to approximate the moving laser beam. The developed finite element model was used to predict the effect of the process parameters on melt pool configuration during the SLM process of the Ti-6Al-4V alloy. The FEA results compared well with the experimental data. Wang et al. (2007) used the 3-D finite element model of the laser deposition process to predict the size of the molten pool and its temperature. These were validated experimentally. The work concluded that the size of the molten pool, temperature distribution within the molten pool, and the cooling rates largely depend on the laser power and velocity.

Wang et al. (2008b) used a 3-D finite element model with element birth and death technique to simulate the LENS deposition of an SS410 plate. They have reported the importance of maintaining a steady melt pool size for attaining a homogeneous microstructure and minimal part distortions. Steady melt pool size was obtained by controlling the laser power as predicted in the FE thermal model. Manvatkar et al. (2011) used the 3-D dimensional heat transfer analysis (FEM based) to calculate the layerwise variation in the thermal cycle and melt pool configuration. The LENS process was used to deposit the austenite stainless steel and the predicted the layerwise molten pool dimensions showed good agreement with the experimental results. Sammons et al. (2013) studied the effect of increase in part height on melt pool. They also reported higher thermal gradients with increase in layers. Amine et al. (2014) used a commercial finite element software ABAQUS to develop the 3-D transient thermomechanical models to understand the temperature and thermal stress distribution in a multilayer part built using the laser deposition technique. A K-type thermocouple in situ was utilized to measure the temperature in each layer, and the experimentally measured temperatures were compared with the numerical model.

Soleymani (2015) developed an FE thermal model for the deposition of a nickel-based superalloy on a steel base plate for the estimation of melt pool size. The results of the estimated melt pool dimensions showed good agreement with the experimental ones. Yan et al. (2016) carried out a 3-D transient thermal analysis of the laser metal deposition of Ti48Al2Cr2Nb alloy for the estimation of temperature and cooling rates. They incorporated the element activation and deactivation technique and a laser heat source as Gaussian distribution equation in the thermal model. The developed FE thermal model helped in predicting cooling rates and thereby produced crack-free parts. Mukherjee et al. (2017b) predicted temperature cycles using 3-D transient thermal and fluid flow analysis. They reported that the estimation of the temperature cycles during deposition helps in controlling residual stress development.

Kamara et al. (2011) carried out a thermomechanical analysis to find the residual stress build-up in laser deposited samples. They claimed that with increasing the number of layers, stress built up in the growth direction of the component. Zhao et al. (2011) investigated thermal stress evolution and residual stress distribution in a multilayer

weld-based rapid prototyping. They reported that the direction of the deposition affected residual stress. Mohammadhosseini et al. (2012) used thermomechanical modeling to understand the build-up of residual stress during the electron beam melting process. They built components of Ti-6Al-4V and reported that if the temperature was in a steady state, then the residual stresses were lower than the yield stress.

Sheng et al. (2007) carried out a three-dimensional transient thermomechanical analysis of the LMD process during the deposition of Ni60A using ANSYS software. The melt pool temperature and stresses were predicted. It was reported that the predicted melt pool temperature showed good agreement with the experimentally (CCD colorimeter) measured temperature. Missouri (2012) carried out thermomechanical modeling using a commercial finite element package ABAQUS. The author reported that stress and strain were induced in the deposited components due to large thermal gradients. Wang et al. (2008a) studied the effect of process parameters such as laser power and scan speed on the residual stress build-up in LENS deposited samples. They measured the residual stresses using the neutron diffraction method. They also carried out a thermomechanical finite element analysis of thin-wall geometries to predict residual stresses and reported good agreement between the FEM results and the neutron diffraction results of the residual stresses. Liu et al. (2013) carried out thermomechanical analysis using ABAQUS and evaluated residual stress and distortion. They used the laser displacement sensor to measure the deflection of the substrate caused by thermal stresses. The results were in good agreement between the modeling predictions of the deformations and the experimental measurements. Denlinger et al. (2014) studied the distortion of large parts (additive manufactured) using a thermo-elasto-plastic analysis. They used the hybrid activation and reactivation strategy. They then deposited large samples using the EBM technique and measured residual stresses. The experimental measurements and the predicted distortions showed good agreement. Ina et al. (2015) built Ti6Al4V alloy samples using the SLM machine. The X-ray diffraction technique was used to measure the residual stress of the samples. It was reported that the residual stress was higher in the scanning direction and lower in the build direction. Each layer experienced a different level of stress due to the nature of the thermal gradients. Parry et al. (2016) carried out a coupled thermal and structural

analysis to understand the effect of scanning paths on stress fields. They found no significant variation on the magnitude of stresses between unidirectional and parallel scanning. However, the distribution of stresses did vary due to the temperature variation with respective scanning plans.

Zyl et al. (2016) deposited Ti6Al4V samples using the DMLS technique and measured the residual stress of the samples using XRD technique. They have found that biaxial tensile stress with major components of stress being in the laser beam guiding direction. Wang et al. (2017) used the neutron diffraction and thermomechanical model to calculate the residual stresses in directed energy deposited IN 625 alloy. The temperature-dependent IN 625 material properties were used in the simulation of the thermomechanical analysis. It was found that the estimated stresses were following the measured residual stresses. Kemerling et al. (2018) investigated the residual stresses development in the Direct Metal Laser Sintering (DMLS) fabrication of the SS304L material using the neutron diffraction and numerical approaches. Process variables such as scan strategy and preheating were used for alleviating the residual stresses. It was reported that tensile stresses were found along the transverse, longitudinal direction, while compressive stresses were dominant along the build direction. The predicted and experimentally measured residual stresses showed comparable agreements. Ahmad et al. (2018) used computation modeling of wire-feed additive manufacturing of Ti alloy to predict residual stress and to compare with experimentally measured residual stress values. They have observed high tensile stresses at the interface and compressive stresses in the deposits. They also showed satisfactory confirming of computational results with experimentally measured stresses. Paul et al. (2014) used thermomechanical finite element models to predict deformation in parts manufactured by AM. They reported that part orientation, slice thickness, scanning speed, and material properties affect thermal deformation.

Zekovic et al. (2005) established a three-dimensional transient thermal-mechanical model. The numerical model incorporated necessary boundary conditions for the estimation of temperature histories for the residual stress and distortion modeling of H13 tool steel material. Temperature dependent thermo-mechanical properties of the H13 tool steel with isotropic hardening were used in the simulation. They reported that

maximum tensile stress was present in the interface of the wall. The developed models helped to identify the location of the stress concentration in the wall. However, the interface of the wall exceeded the yield strength of the material and hence, delamination occurred. Luo et al. (2018) developed a coupled transient thermomechanical FE model to understand the selective laser melting deposition of SnTe thermoelectric material. The moving laser beam assumed as a Gaussian heat source model used the parallel scanning path for SnTe single layer deposition. The governing equations of the thermomechanical model were presented. Higher thermal stresses concentrated in the middle of the first track and reduced in the subsequent tracks. The residual stresses increased with laser power and decreased with the scanning speed. The simulated thermomechanical FE model results were in accordance with the experimental results. Foroozmehr et al. (2010) developed a three-dimensional thermochemical finite element model to study the effect of laser path planning on temperature and residual stresses developed during LMD. It was concluded that the short-bead pattern was minimum and the spiral-in pattern had maximum residual stress in the deposited material. This was due to fact that the short-bead pattern had less temperature variation compared to spiral-in pattern. Pratt et al. (2008) investigated the residual stress development in the LENS deposited AISI 410 stainless steel samples, both numerically and experimentally. They deposited samples at different powers, scan speeds, and at different powder feed rates. They reported that the laser velocity did not contribute significantly to residual stress, while the laser power had a strong influence on the development of residual stress. Rangaswamy et al. (2005) reported the measurement of residual stresses in laser-deposited rectangular and square samples. They measured residual stresses using neutron diffraction and contour method. They reported tensile residual stresses at the edges and compressive residual stresses in the centre of the samples. According to the authors, thermal stresses generated during the process were the likely reason for the development of residual stresses in the components. Moat et al. (2007a) built Waspaloy samples using laser deposition technique and measured residual stresses using neutron diffraction. They reported uniaxial tensile stresses at the top surface and compressive stresses close to the substrate. Moat et al. (2010b) used laser deposition technique to fabricate bulky 3-D geometries. They measured residual stresses in these components using neutron diffraction and contour methods. The effect of thermal gradients on

24

residual stress was relatively lower in bulky 3-D geometries when compared with thin-wall specimens. Levkulich et al. (2019) built Ti6Al4V alloy samples using the powder bed fusion process under various process parameters and measured the residual stresses using X-ray diffraction, contour, and hole drilling methods. They revealed that the process parameters significantly influence the development of residual stresses in the deposits. Further, on the top surface of the deposit, residual stresses had decreased with increasing power, reducing scan speed, and build length of the samples. Moreover, all the three measurement techniques showed the same trend.

2.3.1 Summary of literature review on thermomechanical modeling and measurement of residual stresses in LMD parts

Right from the initial development of the laser-based material deposition processes, analytical and numerical modeling techniques have been used by several researchers to measure melt pool dimensions, temperature distribution, cooling rates, and thermal gradients. The predictions of temperature distribution and melt pool dimensions were validated experimentally by using various thermal imaging techniques. Several researchers have used thermomechanical finite element models to understand the development of residual stresses and to predict their state and magnitude in laser and electron beam fabricated components. Further, residual stresses have also been measured using X-ray diffraction, hole drilling method, contour method, and neutron diffraction techniques. A number of researchers have reported good agreement between modeling and experimentally measured residual stresses. From the reviewed literature, it can be concluded that no work has been reported on either numerical modeling or experimental measurement of residual stresses in laser metal deposition of γ-TiAl alloys.

2.4 Motivation

Titanium aluminide alloy (Ti-48Al-2Cr-2Nb) is an intermetallic alloy. Traditionally, many aerospace components are made of nickel-based superalloys, which approximately have twice the density of γ-TiAl alloys. γ-TiAl alloys have attractive mechanical properties such as high corrosion and oxidation resistance, high service temperature. Therefore, γ-TiAl is a strong candidate to replace Ni-based superalloys in

aerospace applications. However, γ-TiAl alloys are conventionally processed using casting and powder metallurgy techniques. The drawbacks of these techniques include long processing time and costly secondary operations to obtain desired properties. Therefore, there is a need to identify new processing techniques to fabricate γ-TiAl components. In recent years, additive manufacturing techniques have shown promise towards fabricating controlled microstructure and thereby, desired properties are possible with AM techniques.

Computational modeling has become a valuable tool to understand thermal behaviour during the deposition of various materials using a laser and electron beam. Numerical modeling is a valuable tool to predict residual stresses in laser metal deposited components. From the literature review, it has been identified that there are no studies on thermal modeling and the experimental measurement of residual stresses in laser deposited γ-TiAl alloys. Therefore, the focus of the present thesis is to understand thermal behaviour during the laser deposition of γ-TiAl alloys using thermomechanical models to predict residual stresses and to validate these predictions with experimental measurements. The idea is to provide process parameters for fabricating crack free components made of γ-TiAl alloys using the laser metal deposition technique.

2.5 Research objectives

1. To determine the laser absorption coefficient (α_A) of the γ-TiAl alloy by numerical and experimental analysis of the laser surface melting process;

2. To use transient thermomechanical finite element analysis to investigate the effect of the laser process parameters (laser power and scan speed) on the magnitude and distribution of the residual stresses developed during laser surface melting;

3. To simulate the deposition of thin-wall geometries (single row and multiple layers) using the element birth and death technique, and to understand the influence of the deposition process parameters (laser power, scan speed, and substrate pre-heat temperature) on melt pool dimensions, cooling rates, and thermal gradients, and the magnitude and distribution of the residual stresses in the laser-deposited γ-TiAl thin-wall geometries;

4. To simulate the deposition of plate geometries (multiple rows and multiple layers) using the element birth and death technique, and to understand the influence of the deposition process parameters (laser power, scan speed, and raster pattern) on the melt pool dimensions, cooling rates, and thermal gradients, and the magnitude and distribution of the residual stresses in the laser-deposited γ-TiAl plate geometries;

5. To measure the residual stresses in laser-deposited γ-TiAl thin-wall samples and to compare the measured values with that predicted by the thermomechanical finite element models, so as to, validate the finite element model; and

6. To characterize the range of microstructures in the laser-deposited γ-TiAl thin-wall samples.

CHAPTER 3

3   NUMERICAL MODELING METHODOLOGY

This chapter presents the numerical modeling procedures used for simulating the deposition of γ-TiAl thin-wall and plate geometries using Laser Metal Deposition. One of the important parameters needed for carrying out the numerical modeling of the LMD process is the laser absorption coefficient (α_A). In the present thesis, the laser absorption coefficient (α_A) was evaluated by numerical and experimental analysis of the laser surface melting of γ-TiAl alloys. The numerical modeling procedures used for the laser surface melting study are also described in this chapter.

3.1   Flow chart of thermo-mechanical analysis

Figure 3.1 illustrates the overall flow diagram of the sequentially coupled transient thermomechanical analysis. Firstly, the transient thermal analysis was carried out to predict temperature distribution. For this analysis, the necessary material properties, initial conditions, and boundary conditions were applied. The nodal temperatures field obtained by solving each load step, was applied as a function of time. Next, the mechanical analysis was carried out by importing computed temperature distribution and mechanical properties. Finally, the results were extracted from both thermal and mechanical analyses such as temperature field, melt pool, and residual stresses.
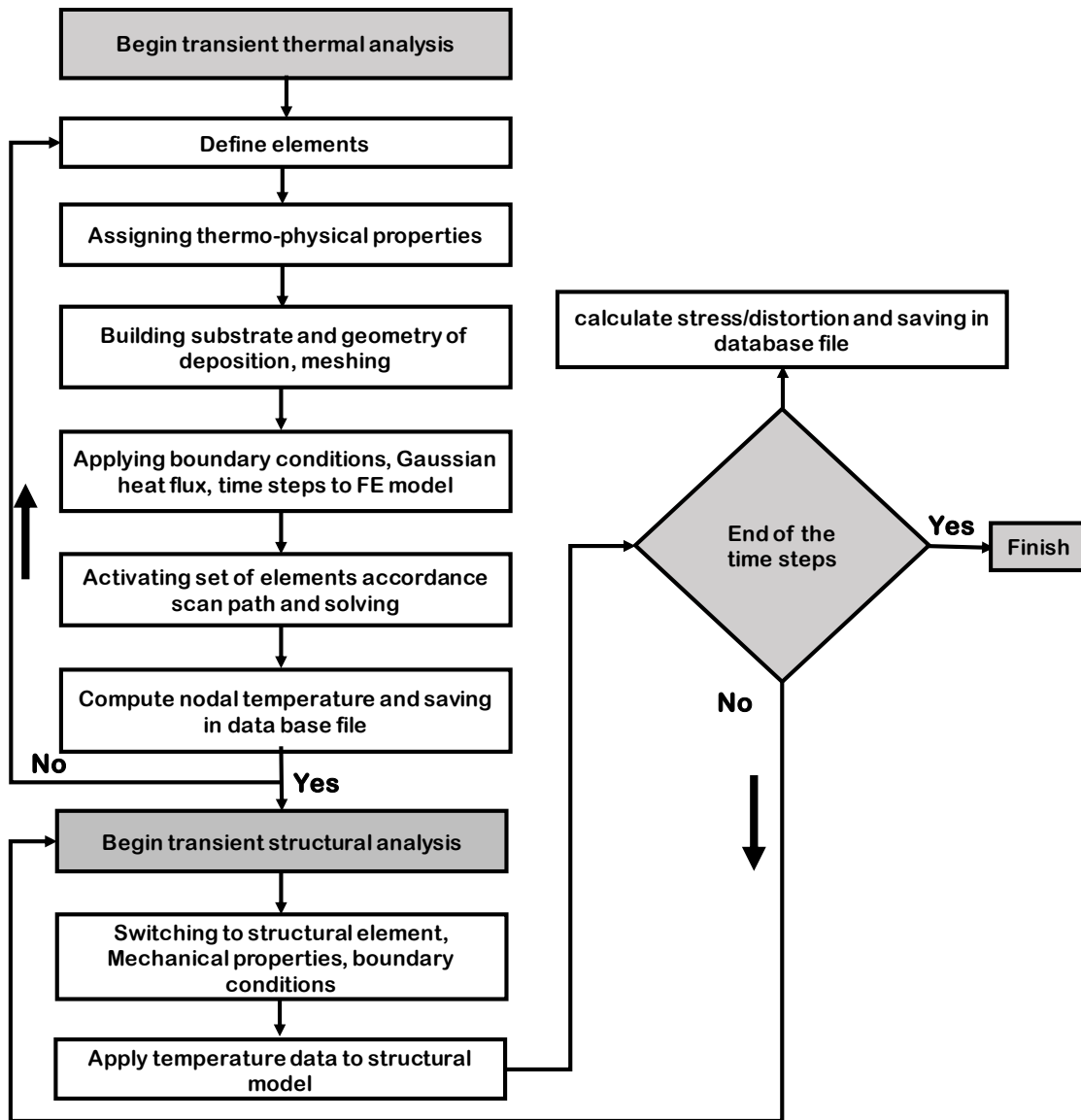
Figure 3.1 Illustrates the overall flow diagram of the sequentially coupled

transient thermo-mechanical analysis

3.2   Geometries considered

The thin-wall and plate geometries considered in this work are shown in Figure 3.2 (a) and (b). The dimensions of the thin-wall considered are length = 15 mm, width = 0.5 mm, and height = 2.5 mm. The thin-wall is considered to be deposited on a substrate whose dimensions are length = 30 mm, width = 10 mm, and height = 2 mm. The dimensions of the plate geometry are length = 20 mm, width = 3 mm, and height = 0.5 mm. Analogues to thin-walls, the plate was considered to be deposited on a substrate

whose dimensions are length = 30 mm, width = 30 mm, and height = 5 mm. When the thin-wall or plate is deposited on the underlying substrate, they bond with the substrate. This physical phenomenon was captured in the models by defining a bonded contact between the deposit and the substrate.
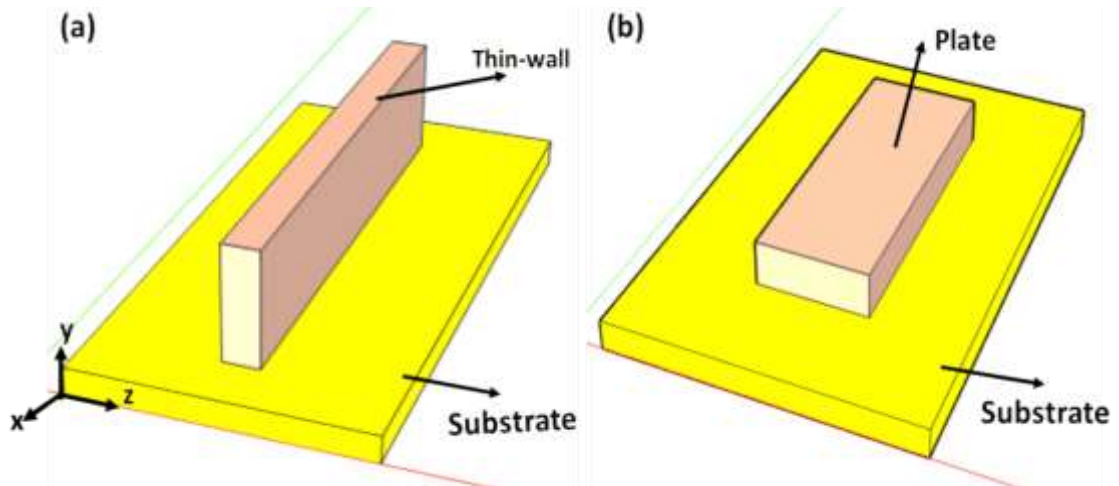
Figure 3.2 Geometries considered in this work (a) Thin-wall and (b) Plate geometries

3.3 Element type
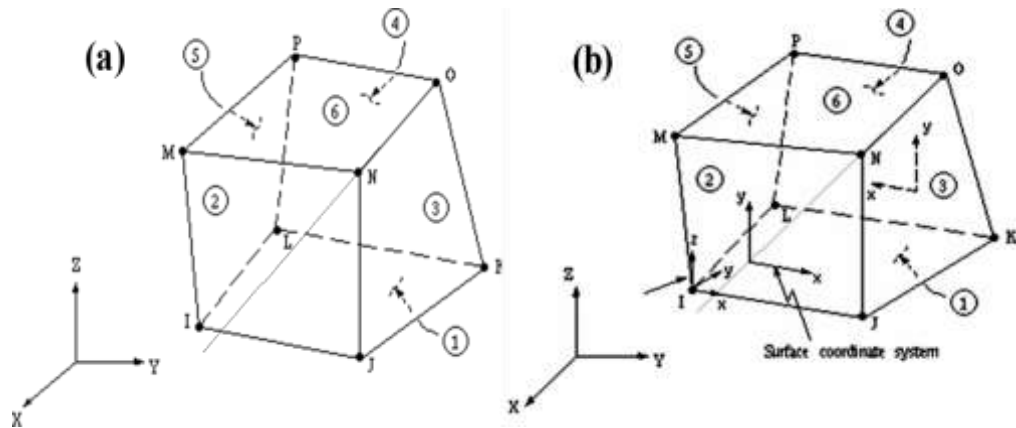
Figure 3.3 Element type used in simulations (a) SOLID 70 element for transient thermal analysis (ANSYS 2017a), and (b) SOLID185 element for transient structural analysis (ANSYS 2017b)

In the LMD process, the main mode of heat transfer is conduction when compared with convection and radiation (Vasinonta et al. (2001)). So, convection and radiation were neglected in the transient thermal analysis. SOLID 70 element (Figure 3.3 (a)) was used

31

in the simulation to capture the thermal behaviour. The SOLID 70 element has eight nodes with a single degree of freedom at each node (ANSYS 2017a). This element possesses three-dimensional thermal conduction capability and can be used in steady-state or transient analysis. The mechanical analysis was carried out by switching the element type to SOLID 185 (Figure 3.3 (b)). This element has 8 nodes with three degrees of freedom at each node, namely, translations in x, y, and z directions (ANSYS 2017b). The element is capable of receiving temperature distribution from the transient thermal analysis. The addition of material in the LMD is accounted by using the element birth and death technique. Both the elements, namely, SOLID 70 and SOLID 185 can be used with the EBD technique.

3.4 Assumptions

The following assumptions were made to simplify the numerical modeling:

- Convection and radiation heat transfer were neglected as conduction was the predominant mode of heat transfer in the LMD;
- The Marangoni effect in the melt pool was neglected;
- Forced convection caused by the purged argon gas was not considered;
- Evaporation in the melt pool was not considered; and
- The reference temperature for strain calculation is the initial temperature.

3.5 Laser surface melting
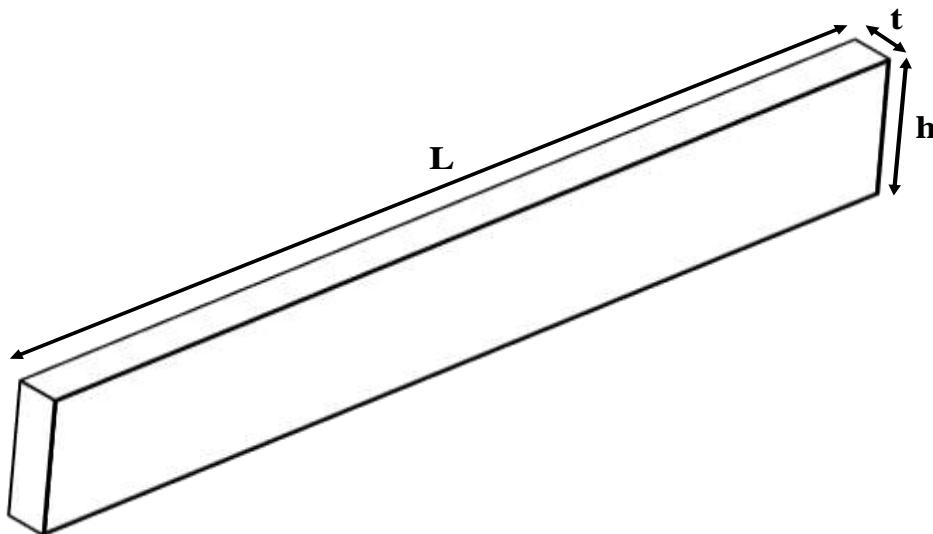
Figure 3.4 Thin-wall geometry considered for the LSM simulation

In the present thesis, the main focus of the laser surface melting (LSM) was to determine the laser absorption coefficient (α_A) of the γ-TiAl alloy. To this end, a numerical modeling and experimental analysis of the laser surface melting process was carried out. In the LSM simulations, there was no powder addition and hence, the EBD technique was not considered. The LSM process was simulated as a single laser pass (from left to right) on the substrate. The dimension of the substrate (Figure 3.4.) used for LSM analysis included length (L) = 50 mm, height (h) = 8.6 mm, and thickness (t) = 2 mm.

3.6   Material properties of γ-TiAl alloy

Thermo-physical properties density (ρ), specific heat (C_p), and thermal conductivity (k) used as functions of temperature in the transient thermal simulations are presented in Table 3.1. The latent heat of fusion during melting was taken into consideration by modifying the specific heat at the melting temperature using the following equation (Fallah et al. 2011):

$$C_P^* = C_P + \frac{L}{T_m - T_0} \qquad\qquad 3.1$$

Where, C_P^* is the modified specific heat at melting temperature, C_p is the actual specific heat at melting temperature, L_f is the latent heat of fusion, T_m is the liquidus temperature of the γ-TiAl alloy, and T_0 is the initial temperature of the substrate, which is 25°C.

Table 3.1 Thermo-physical properties of γ-TiAl alloy (Sung et al. 2006)

Temperature (^{o}C)	Density (Kg/m^3)	Specific heat (J/kg K)	Thermal conductivity (W/m K)
25	3900	610	10
126	3893	635	15
326	3879	670	18
526	3866	695	21
726	3853	725	24
926	3840	770	26
1460	-	1060*	-
1533	3800	780	28

* Modified specific heat at the melting temperature to include effect of latent heat

The properties required for structural simulations included Young's modulus (E), Poisson's ratio (µ), coefficient of thermal expansion (α), and yield strength (σs). These properties as a function of temperature are documented in Table 3.2**.** Further, to capture the plasticity behaviour of the material, the bilinear isotropic hardening (BISO) model was used.

Table 3.2 Mechanical properties of γ-TiAl alloy (Zhang et al. 2009; Yan et al. 2016)

Temperature ^{o}C	25	150	300	450	600	900
Young's modulus E/GPa	172	166	162	157	153	144
Yield strength σ_{ys}/N/m^2	360×10^6	374×10^6	359×10^6	337×10^6	330×10^6	259×10^6
Thermal expansion α/10^{-6}K^{-1}	11	11.7	12	13	14	15
Poisson's ratio µ	0.22	0.22	0.22	0.22	0.22	0.22
Tangent modulus/MPa	377×10^6	392×10^6	376×10^6	353×10^6	345×10^6	271×10^6

3.7 Scanning patterns considered

As observed in Figure 3.5. Here, the laser beam traverses from the left side to the right side of the thin-wall. After the deposition of one layer, a dwell time of 2s is considered. After which, the travel of the laser beam is again from the left to the right side with an increment in layer thickness of 0.25 mm. For the plate geometry simulations, both the unidirectional and bidirectional (Figure 3.6) scan strategies were considered. The main difference between the simulations of thin-wall and plate geometries are in the number of tracks in each layer. In the case of thin-wall geometry, there is only one track in each layer. However, for plate geometry, there are six tracks in each layer. The computational models used in this work consider only the most commonly used scanning strategies (unidirectional and bidirectional) for deposition of thin-wall and plate geometries. Other scan strategies such as zig-zag, spiral inwards, spiral outwards, YY pattern, etc. are generally used during fabrication of complex geometries (Ghosh and Choi 2007; Ren et al. 2019) and hence were not considered in this research.

Unidirectional scan pattern for thin-wall deposition
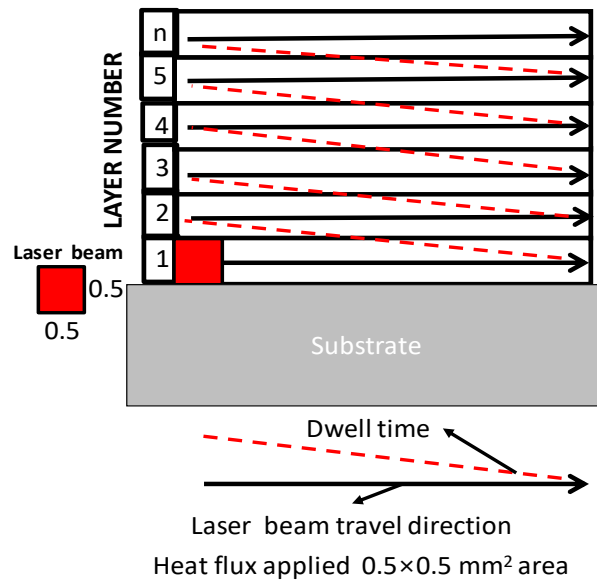
Figure 3.5 Schematic of unidirectional scanning strategy
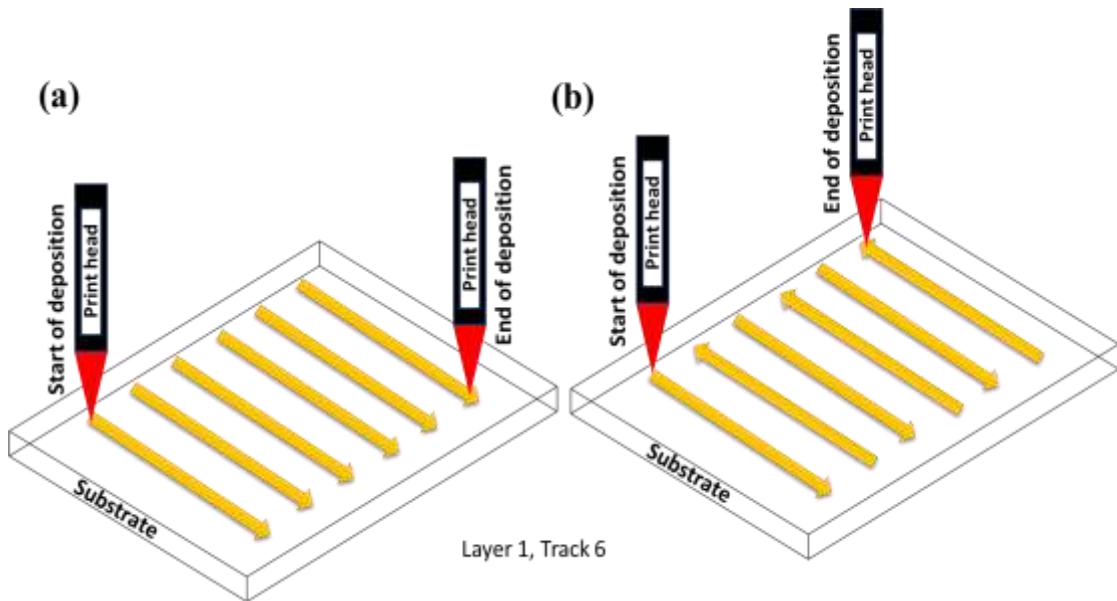
Figure 3.6 Schematic of scanning strategy (a) Unidirectional and (b) Bidirectional

3.8 Laser heat source model

The laser was modelled as a heat source with Gaussian distribution, as shown in Equation 3.2 (Fu et al. 2014). A 2-D Gaussian equation represents the heat flux applied on the surface of the elements.

$$F = \frac{2\alpha P}{\pi r^2}\, e^{\left(-2\frac{x^2+y^2}{r^2}\right)} \qquad\qquad 3.2$$

Where F is the heat flux in J/mm^2, α is the laser absorption coefficient, P is the laser power in watts, r is the radius of the laser beam in mm, and x and y are the variables which specify the distance from the centre of the laser beam. Laser processing conditions were used in this equation to simulate each condition. The movement of the laser beam was taken into account by using a moving coordinate system. Further, the laser spot overlap was not considered in the simulation studies of both thin-wall and plate geometries.
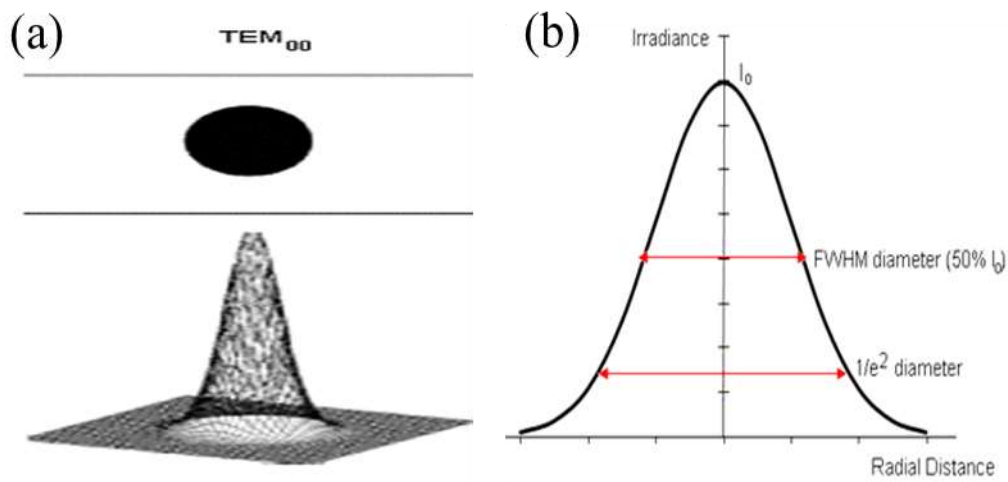
Figure 3.7 (a, b) Gaussian distribution for TEM$_{00}$ mode (Roberts et al. 2009)

3.9   Governing equations

Thermal analysis

A three-dimensional transient heat transfer analysis of the layer-by-layer deposition in the LMD process was carried out in the current work. The transient heat conduction equation in the three-dimensional Cartesian coordinate system can be written as (Fallah et al. 2011):

$$\frac{\partial}{\partial x}(k\frac{\partial T}{\partial x}) + \frac{\partial}{\partial y}(k\frac{\partial T}{\partial y})+\frac{\partial}{\partial z}(k\frac{\partial T}{\partial z})+ \dot{q} = \rho C_p \frac{\partial T}{\partial t} \qquad\qquad 3.3$$

Where k is the thermal conductivity, T is the temperature of the part, $\dot{q}$ *is* rate at which the heat is supplied to the system, ρ is the density of the material, and C_p is the specific heat (Fallah et al. 2011).

36

The initial condition specifies the substrate to be at room temperature,

$$T(x, y, z, 0) = 25\ ^oC \qquad\qquad 3.4$$

For newly added material, the boundary condition is specified as follows:

$$T(x, y, z, t_{activation}) = 25\ ^oC \qquad\qquad 3.5$$

Mechanical Analysis

The body temperatures from the transient thermal analysis were imported using the LDREAD command into the mechanical analysis. Therefore, the temperatures obtained from the thermal analysis were used as loads in the mechanical analysis. Also, the temperature-dependent mechanical properties are important in the development of thermal stresses.

The total strain ε is represented as:

$$\varepsilon = \varepsilon^{el} + \varepsilon^{p} + \varepsilon^{th} \qquad\qquad 3.6$$

Where $\varepsilon^{el}, \varepsilon^{p}, and\ \varepsilon^{th}$ are the elastic strains, plastic strains, and thermal strains, respectively. The stress components were computed from the elastic strains as follows (Roberts 2012):

The elastic component can be written as follows:

$$\varepsilon^{el} = \varepsilon - \varepsilon^{p} - \varepsilon^{th} \qquad\qquad 3.7$$

Therefore stress field is computed as follows (Roberts 2012):

$$\{\sigma\} = [D]\ \{\varepsilon - \varepsilon^{p} - \varepsilon^{th}\} \qquad\qquad 3.8$$

Where, $[D]$ is the stress-strain matrix.

3.10 Numerical simulation

The simulation of the developed thermo-mechanical models was carried out using the commercially available ANSYS (APDL-Advanced Parametric Design Language) software. The thermal analysis was solved using the Newton-Rapson solver with a full transient method. The mechanical analysis was solved using a Pre-Conditioned Conjugate Gradient (PCG) solver. PCG is better for large displacement and non-linear problems compared with the SPARSE and FRONTAL solvers. The accuracy of the temperature and stress field also depends on the number of finite elements and sub-

steps used in the thermomechanical analysis. Hence, suitable elements and sub-steps were used in thermomechanical model.

The parametric analysis of the thermo-mechanical models (thin-wall, plate and LSM geometries) was carried out in 32 cores workstation. Upon completion of the simulations, melt pool dimensions, temperature cycles, magnitude, and distribution of the residual stresses were extracted from the thermo-mechanical models.

3.11 Element birth and death (EBD) technique

The addition of material during the LMD process was captured in the simulations using the element birth and death technique. Here, initially the finite element model included both the substrate and the deposit. At the start of the simulation, all the elements of the deposit (either thin-wall or plate geometry) were killed (temporarily deactivated) by multiplying their thermo-physical properties by a severe reduction factor of about 10^{-6}, such that these elements did not contribute to the finite element equations or the conductance matrix. Then to mimic the deposition process, the elements were activated (thermo-physical properties restored to their original values) based on the location of the laser as shown in Figure 3.8. As the laser moved to the next location, the next set of elements were activated. This process was continued until the entire geometry was deposited.
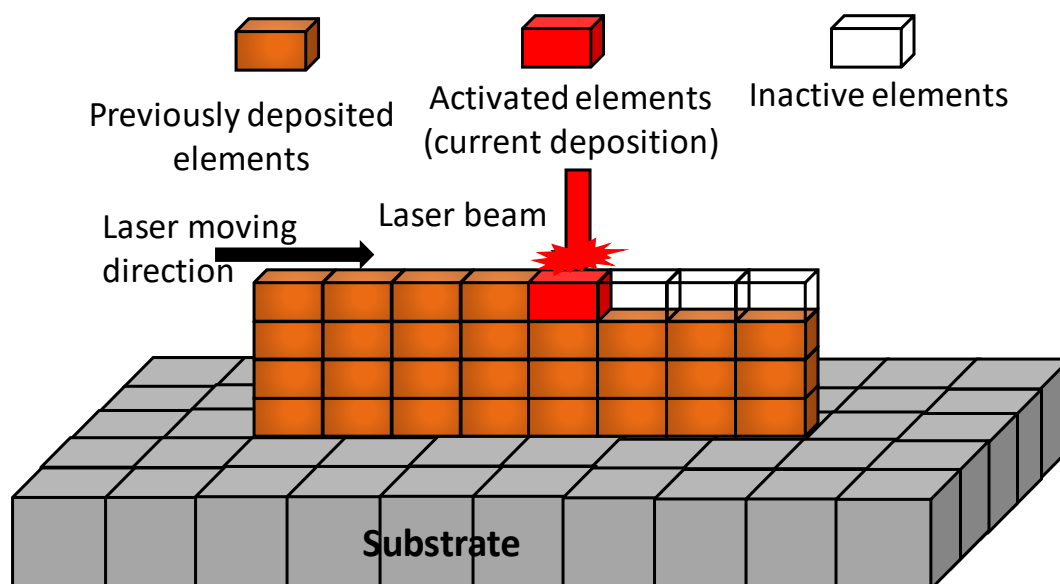
Figure 3.8 Illustration of the element birth and death technique

38

CHAPTER 4

4   EXPERIMENTAL METHODOLOGY

This chapter describes the experimental methodology used for the deposition of the samples, measurement of residual stresses, microstructural analysis, and hardness measurement in the deposited samples. Also, the experimental work carried out as part of the laser surface melting study to determine α_A is also presented herein.

4.1   Materials

The material used in the present research is γ-TiAl alloy. Pre-alloyed γ-TiAl powder was procured from Arcam, Sweden. The alloy consists of 48 at. % Al, 2 at. % Cr, 2 at. % Nb, and the rest is Ti. The size of the γ-TiAl powder particles varies between 45-150 µm and is mostly spherical in shape.

4.2   Laser metal deposition of γ-TiAl alloy

Thin-walls were fabricated using one of the laser metal deposition techniques called the Laser Engineered Net Shaping (LENS) MR7 (Optomec, Albuquerque, NM, USA) has a continuous wave ytterbium-doped fibre laser. The process starts when a high-intensity laser beam targets a tiny spot on a metal substrate, producing a molten pool. From either side of the laser nozzle, a precise amount of metal powder is blown into the melt pool to increase the size of the material. The laser beam builds the part layer-by-layer to the CAD geometry as the system moves the substrate under the beam in the XY plane and nozzle head moves up one-layer thickness in the Z direction. This lasing and powder deposition process continues until the entire part is completed. The action takes place in a sealed chamber, where the restricted environment variables can be tightly controlled. The oxygen level is controlled below 10 ppm in an argon atmosphere. The experimental set-up of the LENS equipment is shown in Figure 4.1 and the schematic of the LENS deposition of thin-wall is illustrated in Figure 4.2.
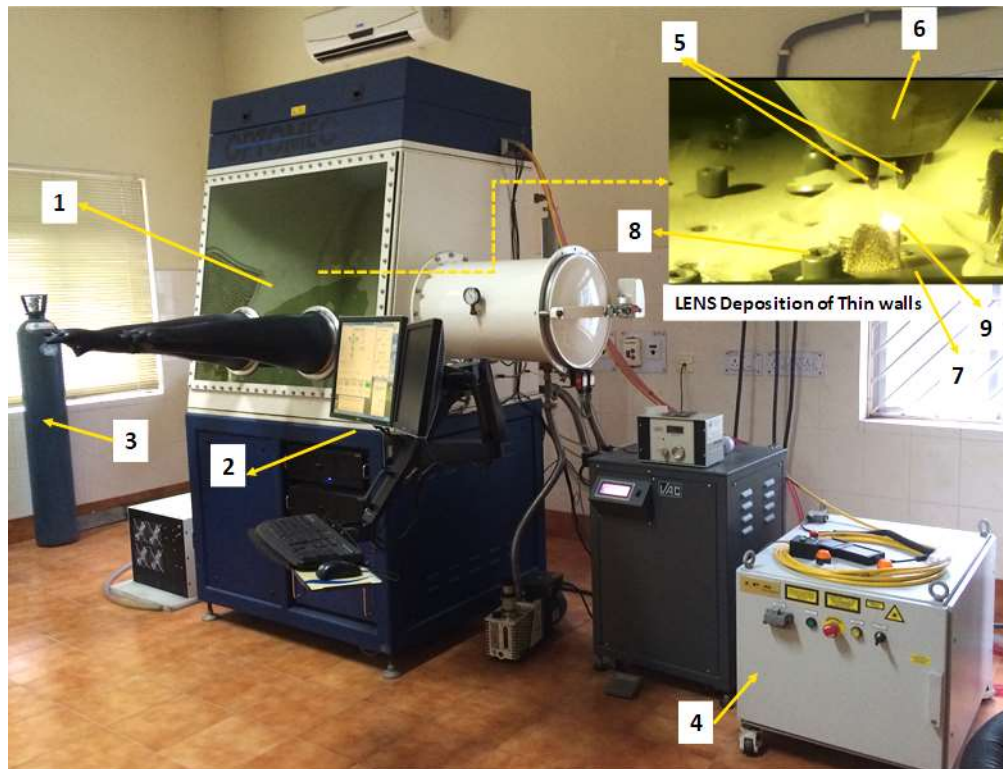
Figure 4.1 Experimental set up of LENS equipment (Curtsey: CSIR-CGCRI, Kolkata)

The primary parts of the LENS equipment are shown in Figure 4.1 and are presented below:

1. Glovebox,
2. Computer controller unit,
3. Gas cylinder,
4. Laser supply unit,
5. Powder feed nozzles,
6. Deposition head,
7. Substrate,
8. Clamping, and
9. Laser beam.
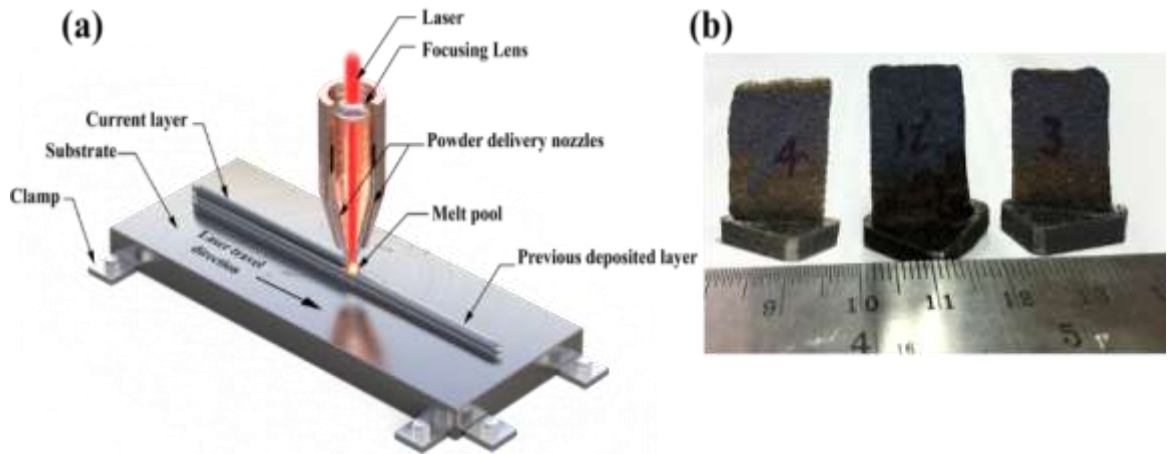
Figure 4.2 LMD process (a) Schematic representation and (b) As-deposited thin-wall structures

Table 4.1 Process conditions used for depositing thin-wall samples

Power (W)	Travel speed (mm/s)	Energy density (J/mm^2)	Abbreviation	Layer height (mm)	Powder feed rate (g/min)
200	8	50.0	200-8		2.9-3.3
200	10	40.0	200-10	0.25	3.3-3.66
200	12	33.3	200-12		4.0-4.4
250	8	62.5	250-8		2.9-3.3
250	10	50.0	250-10	0.25	3.3-3.66
250	12	41.6	250-12		4.0-4.40
300	8	75.0	300-8		2.9-3.3
300	10	60.0	300-10	0.25	3.3-3.66
300	12	50.0	300-12		4.0-4.4

Thin-wall samples of dimensions $15 \times 20 \times 2$ mm^3 (Figure 4.2 (b)) were fabricated at different laser powers, travel speeds, and powder flow rates as documented in Table 4.1. A layer thickness of 0.25 mm was used for all the samples deposited in this work. The spot size of the laser beam was 0.5 mm. The laser energy density was calculated as (Balla et al. 2016):

$$E = \frac{P}{Vd} \qquad\qquad 4.1$$

Where E is the laser energy density in J/mm^2, P is the laser power in Watts, V is the travel speed in mm/s and d is the laser spot diameter in mm.

An important point to note here is that the LSM study was carried out using the same LENS MR-7 system without the addition of powder material (i.e., powder hoppers were not used for the LSM study). Different processing conditions were used for remelting the samples and are presented in Table 4.2. Microstructural, phase analysis, and hardness study were carried out on the deposited as well as LSM samples.

Table 4.2 Laser process conditions used in the remelting study

Laser power (W)	Travel speed (mm/s)	Abbreviation	Energy density (J/mm^2)
200	10	200-10	40
300	10	300-10	60
400	10	400-10	80

4.3   Measurement of residual stress

The X-Ray diffraction technique was used to carry out the residual stress measurements of the deposited samples. A PROTO iXRD equipped with Cu-K$_\alpha$ radiation and λ = 1.5418 A^o was used for residual stress measurements. The optimum measurement conditions included a 3 mm collimator (Aperture), a 25 kV voltage with a target current of 4 mA, exposure time (at each point) of 14 min, and an angle of $2\theta = 142^o$. The strain and stress were calculated using the linear elasticity theory (Fitzpatrick et al. 2006) and the slope of the 2θ vs. $\sin^2 \psi$ plot. The PROTO iXRD equipment and its parts are shown in Figure 4.3.

1. Goniometer
2. Detectors
3. X-ray beam status
4. X-ray radiation
5. Laptop with XRD win 2.0 software
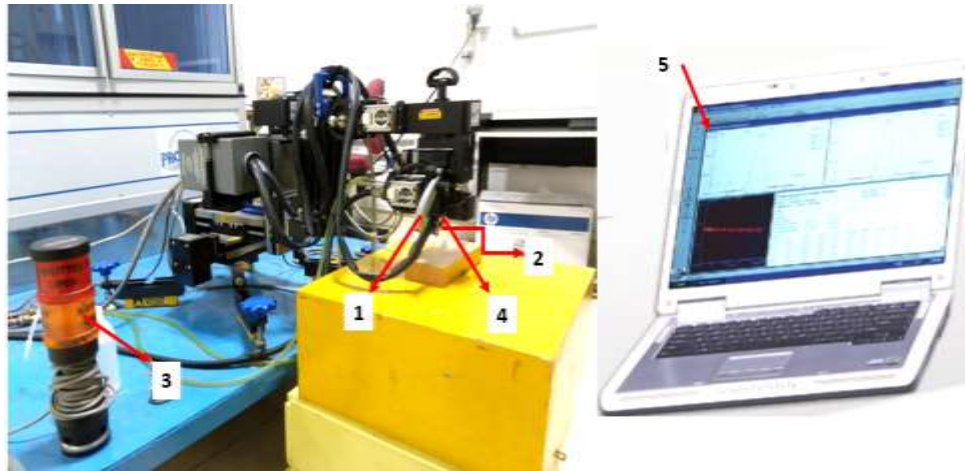
Figure 4.3 Portable XRD based residual stress measurements (Courtesy: MCD division DRDL Hyderabad)
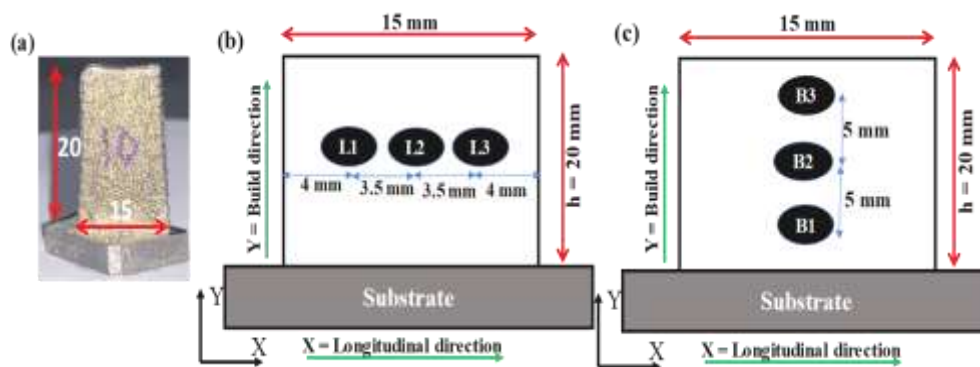
Figure 4.4 (a) Typical γ-TiAl thin-wall deposited on a substrate (b) Location of residual stress measurements along longitudinal and (c) Build directions.

Figure 4.4 shows the Residual stress measurement locations. A total of six points were considered along the longitudinal and build directions. The locations of the points along the longitudinal direction were as follows: point L1 is 4 mm away from the left edge, point L2 is at the centre of the sample, and point L3 is 3.5 mm away from the centre point L2. The distances of the points along the build direction are as follows: the centre point B2 is at the mid-point of the sample in the vertical direction, and the points B1 and B3 are 5 mm above and below from the centre point B2. The residual stresses were measured five times at each point, and the average of the five readings is reported. The residual stress measurements carried on all deposited samples are presented in the results section.

43

4.4 Measurement of surface roughness

The roughness of the deposited thin-walls was measured using a non-contact type Confocal Microscope, OLS4000 (Japan) equipped with class 2 laser and wavelength of 412 nm. Five measurements were taken along the build direction. The arithmetic mean height (S_a) with standard deviation was reported.

4.5 Microstructural analysis

The as-built thin-wall samples were separated from the substrate using Wire Electric Discharge Machining (EDM). The required size of the sample was cut for microstructure observation using the Metallurgical saw MS-10, Ducom (India), both along the build and transverse directions. The samples were mirror-polished using metallurgical standards, followed by etching of the samples using Kroll's (50 ml HF, 50 ml HNO_3 60% concentration, and 150 ml H_2O) reagent. The microstructural analysis was carried out using both optical (EVO MA18 with Oxford EDS, Germany) and scanning electron (EVO MA18 with Oxford EDS, Germany) microscopes at different regions of the samples.

4.6 Phase analysis

The formation of different phases of the as-deposited sample was identified by X-Ray diffractometry (Rigaku smart lab, Japan) operating at a 40 kV voltage and a current of 30 mA. The data was collected using monochromatic CuK_α radiation ($\lambda = 0.154$ nm) with a scan speed of 2° per minute over a range of 20° to 90°.

4.7 Mechanical properties

Vickers microhardness test was carried out using HMV-G 20ST (Shimadzu, Japan). The microhardness tests were carried out at a load of 200 g with a dwell time of 15 sec. The hardness measurements were carried out along both the longitudinal and build directions.

5 LASER SURFACE MELTING: RESULTS AND DISCUSSION

This chapter presents and discusses the results of the laser surface melting study. Both the modeling and experimental results will be discussed in the subsequent sub-sections. As discussed earlier, the primary goal of the LSM study is to determine the laser absorption coefficient (α_A). However, after surface melting, cracks were noticed in the remelted region and hence, a thorough study of the thermal behaviour as well as evolution of the residual stresses were also carried out.

5.1 Thermomechanical analysis of LSM process

5.1.1 Geometry and mesh attributes of LSM

The commercially available Finite Element Analysis (FEA) package ANSYS was used to simulate the LSM process. In the FE model, Figure 5.1 (a), the dimensions of the plate considered were 50 mm length $\times$ 8.6 mm width $\times$ 2 mm thickness. In the meshed model, solid 70 and solid 185 elements were used for thermal and mechanical analysis, respectively. The model consisted of 56,000 elements and 64,119 nodes. Highly refined mesh with an element size of 250 µm length $\times$ 50 µm width $\times$ 83 µm thickness ((enlarged view of Figure 3.3 (a)) was used along the laser travel direction (i.e., along with the x-axis). The temperature of the bottom surface of the substrate was fixed at 25 °C, while all other faces were insulated (q=0).
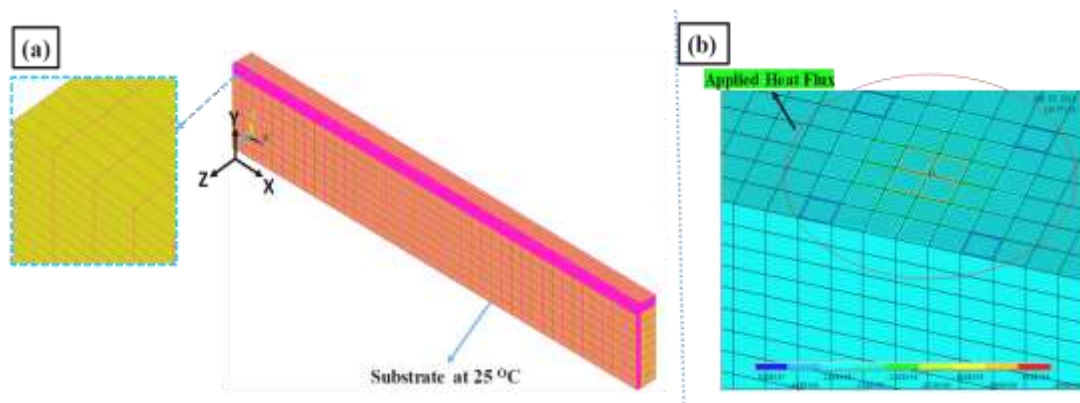
Figure 5.1 Finite element model (a) Shows meshed model along with boundary condition (b) Applied heat flux on the surface of elements

5.1.2 Melt pool dimensions

Figure 5.2 presents the temperature contours in the melted region. The red-coloured region in these contours indicates the melt pool region, i.e., the region where the temperature is greater than the liquidus temperature of the γ-TiAl alloy. The melt pool depth and length were measured from these contours and compared with the experimentally determined dimensions.
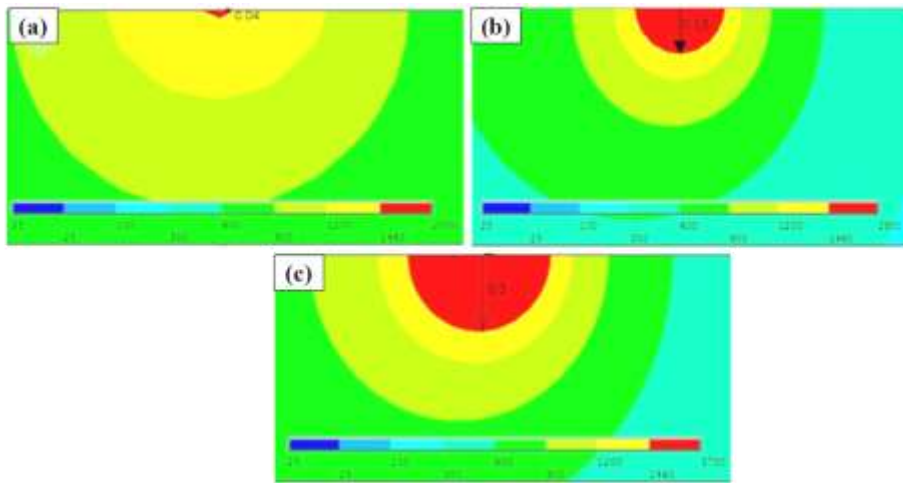
Figure 5.2 Estimated melt pool contours during LSM at (a) 200 W (b) 300 W (c) 400 W

5.1.3 Temperature fields

The temperature distribution in the melt pool along the width direction is presented in Figure 5.3 (a). These temperatures were extracted from the centre of the melt pool. For all the laser powers, it could be observed that the temperature decreased with the increase in the width. The occurrence of maximum temperature at the location of maximum applied heat flux is in accordance with the heat source model represented by Equation (3.2). The applied heat flux on the surface of the solid sample is shown in Figure 5.1 (b). As the laser power was increased from 200 to 400 W, the peak intensity of heat flux was found to increase from 89061 W/m^2 to 180272 W/m^2. Similarly, high values of heat flux (in computational models of LAM processes) were reported in literature by several other researchers (Al-Sayed Ali et al. 2019; Marshall et al. 2016). It was observed that as the laser power increased, the heat flux increased in the centre of the laser beam. This heat flux diminishes by 1/e^2 as it radially moves outward from

46

the centre of the laser beam. Therefore, the peak temperature and its profile changes in accordance with the irradiance intensity on the surface of the solid samples along with width and longitudinal directions.
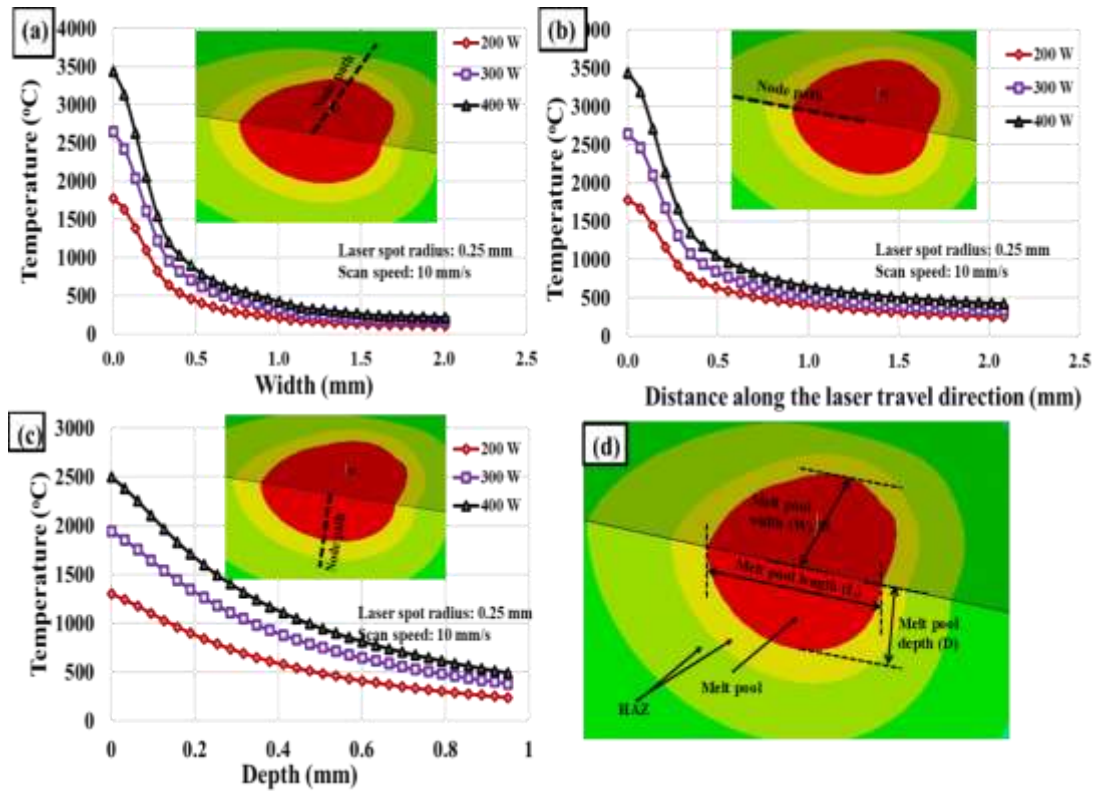
Figure 5.3 Temperature in melt pool along (a) Width direction (b) Distance along laser travel direction (c) Depth direction and (d) Melt pool configuration

The distribution of temperature along the longitudinal direction is shown in Figure 5.3 (b). A steep temperature change is noticed in this direction compared with the other two directions. The temperature becomes steeper as the laser power is increased from 200 W to 400 W at the surface. This gradient in temperature distribution is mainly the higher energy density found on the surface rather than the subsurface. The temperature distributions along the depth direction are presented in Figure 5.3 (c). The temperatures were extracted at the centre of the melt pool starting from the surface through a depth of 1000 µm. This depth of 1000 µm encompasses the molten pool as well as the HAZ. It is clearly evident from these plots that for all the laser powers, temperatures decrease rapidly from the melt pool surface to the substrate. Further, the increasing laser power at constant velocity results in higher temperature gradients. It is evident from Figure

5.3 (c) that maximum temperature at the melt pool surface along the depth direction is 1464 ºC, 2000 ºC, and 2500 ºC for 200 W, 300 W, and 400 W, respectively.

5.1.4 Cooling rates

The cooling rates experienced by the material during LSM were extracted from the transient thermal analysis on the melt pool surface. The liquidus and solidus temperatures of the TiAl alloy are 1460 ºC and 1440 ºC, respectively. In this narrow temperature range, the variation of temperature with time is assumed to be linear. The cooling rate at the onset of solidification is given by Equation (5.1) (Bontha et al. 2006).

$$\frac{\partial T}{\partial t} = \left| \frac{T_s - T_l}{t_s - t_l} \right| \qquad\qquad 5.1$$

Where, T_l and T_s are the liquidus and solidus temperatures attained at times t_l and t_s, respectively. To extract the cooling rates, time versus temperature data was used on the surface of the melt pool. The maximum cooling rate was observed at the surface and the minimum at the bottom of the melt pool. The cooling rates estimated for the three powers are presented in Table 5.1.

Table 5.1 Cooling rates, temperature, and thermal gradients at melt pool surface

Velocity 10 mm/s	Cooling rates ºC/s	Temperature (ºC)		Thermal gradients (ºC/m)	
Power (W)	(Melt pool surface)	Middle (Region B)	Right end (Region C)	Middle (Region B)	Right end (Region C)
200	6.0×10^5	1774	1993	2.60×10^6	2.67×10^6
300	3.12×10^5	2645	3061	3.82×10^6	4.08×10^6
400	1.25×10^5	3436	3999	5.09×10^6	5.45×10^6

The cooling rates decreased from 6.0×10^5 ºC/s to 1.25×10^5 ºC/s with the increase in power from 200 W to 400 W. This shows that the laser power of 400 W increases the thermal energy in the irradiated region. This results in large thermal gradients and low cooling rates in the irradiated region, which is processed at 400 W. These high cooling rates are found to have a direct influence on the microstructures, hardness, and cracks observed in the samples. For example, high cooling rates result in refined

microstructures leading to an increase in hardness. At the same time, rapid cooling rates can generate excessive residual stresses (Carcel et al. 2014) and develop cracks in the solidified region of the melt pool. Therefore, the prediction of cooling rates during melting enables better control of the microstructures and cracking propensity.

5.1.5 Von Mises stresses

The rapid cooling rates can generate large amounts of stresses during solidification, which can lead to cracking. The schematic representation of the regions and the stress extraction path is shown in Figure 5.4 (a). The Von Mises stress contour for 200 W is shown in Figure 5.4 (b). The maximum stress was found in the mid-top surface of the substrate and minimum stress was found at either end of the substrate. The stress distribution at room temperature along the x-axis is shown in Figure 5.4 (c). The stress plot is divided into three regions, i.e., Region A is the left end of the substrate; Region B is the middle or core of the substrate, and Region C is the right end of the substrate. It can be seen that the stress gradually reduces in regions A and C, while uniform stress distribution is exhibited in region B due to the anisotropic thermal gradients in these regions. Similar stress distribution has been reported (Yilbas et al. 2011) in laser surface melted alumina. Thermal gradients at the surface of the melt pool in the three regions are summarized in Table 5.1, which shows that thermal stress is relieved in regions A and C, due to large thermal gradients. The highest Von Mises stresses at region B is due to steep thermal gradients along the x-axis at the surface vicinity. It is understandable that the developed residual stress should not exceed the yield strength of the material to prevent cracking. However, maximum stress in the melted region was found to be 596 MPa (for 200 W), exceeding the yield strength of the material (400 MPa), and therefore, resulted in cracking. Further, similar stress behaviour was observed in the samples processed at 300 W and 400 W power. However, with increasing laser power from 200 W to 400 W, the magnitude of the stress also increased from 596 MPa to 835 MPa. Since the induced stresses exceeded the yield strength, all the samples showed microcracks, as shown in Figure 5.5.

The Von Mises stress for 200 W at room temperature along the transverse direction is shown in Figure 5.4 (d). The stress decreased while moving away from the laser irradiation spot, as from Figure 5.3 (a). The stress variation followed the Gaussian heat

flux distribution, i.e., bell shape at the laser irradiation region, while a constant value of stress was observed in the rest of the region. Also, the magnitude of the stress developed in the transverse direction exceeded the yield strength of the γ-TiAl alloys. Hence, microcracks were also found along the transverse direction (Balichakra et al. 2019a).
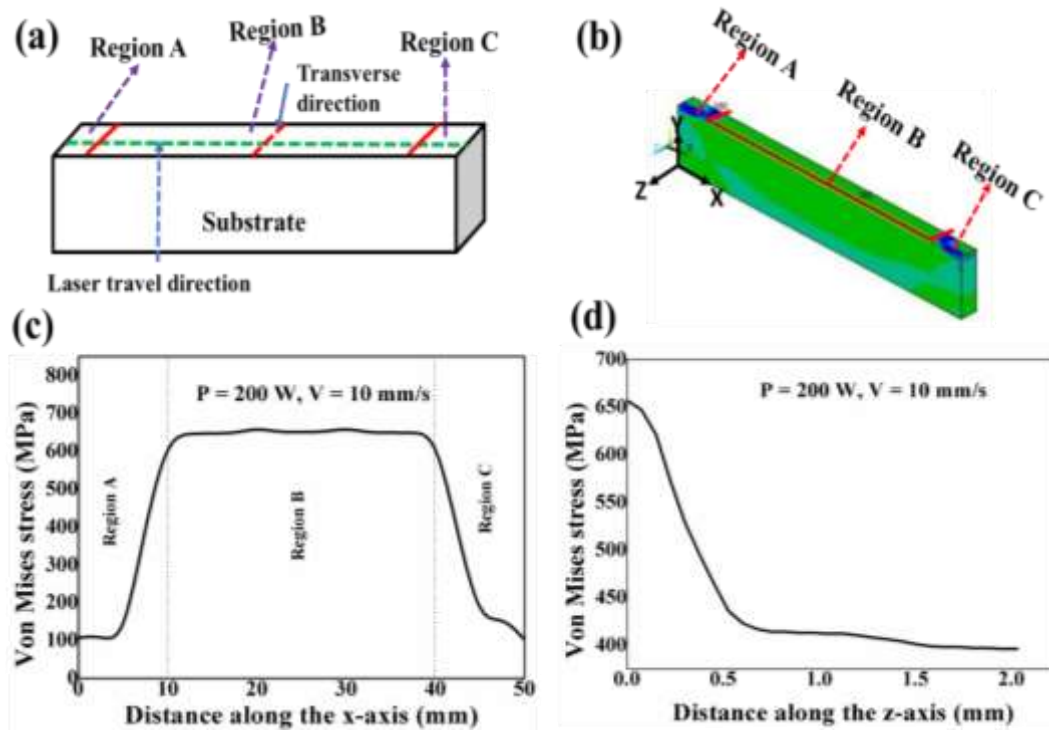
Figure 5.4 Von Mises stress (a) Schematic representation of regions and paths (b) Stress contour for 200 W (c) Stress along the longitudinal direction (d) Stress along the transverse direction

5.1.6 Experimental results

5.1.7 Microstructural and melt pool analysis of LSM samples

Figure 5.5 shows the microstructures of the substrate and melted region of the γ-TiAl alloy samples processed at different laser powers. The substrate exhibited a fully lamellar microstructure consisting of alternating γ-TiAl and α_2-Ti$_3$Al plates stacking up into the lamellas. It was observed that this kind of similar lamellar structure was found to be more ductile than the equiaxed microstructure. The microstructure of the melted region showed a single-phase and appeared to be a massive γ phase. The formation of

a single phase in this region was attributed to the rapid cooling rates experienced by the material during LSM. The LSM regions of the sample also showed cracks under all processing conditions.
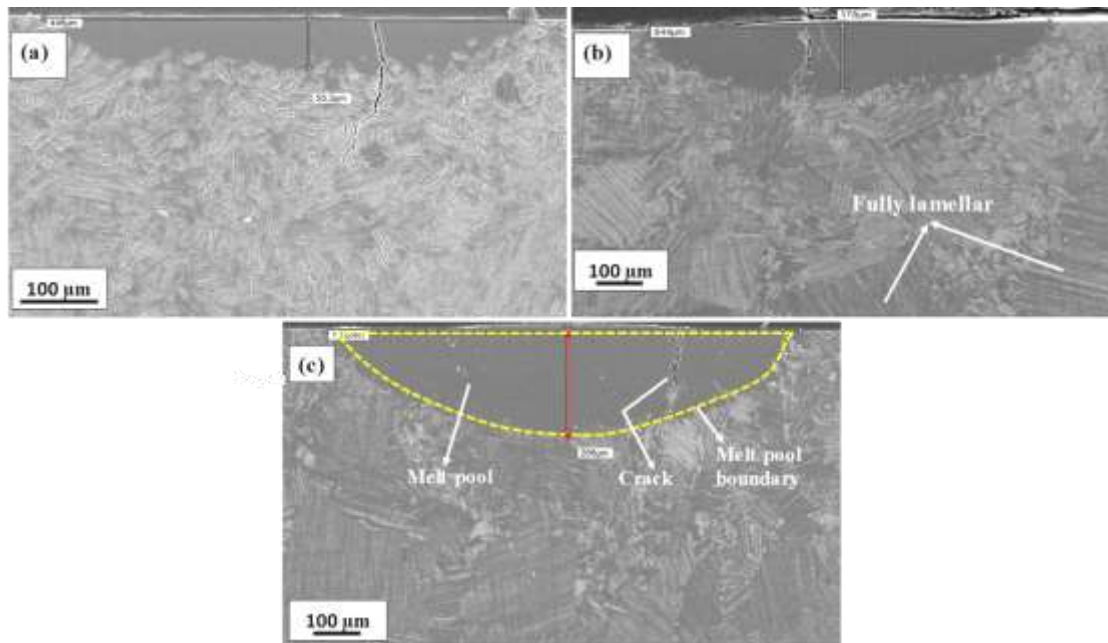
Figure 5.5 SEM images showing microstructures of the substrate and melted regions of γ-TiAl alloy (a) 200 W (b) 300 W (c) 400 W

Further, the cracks appeared to have propagated from the surface of the melt pool into the substrate. The maximum crack length along the melt pool cross-section was measured to be 600 µm in the samples processed with 400 W and 10 mm/s. The results indicated that the crack depth increases with increasing power at a constant velocity. This is attributed to the deeper melt pools and stress fields present in the melted regions formed during LSM at high laser power. Further, the cracking indicates that the developed residual stresses are tensile in nature and exceed the yield strength of the material. The melt pool dimensions such as depth and length increased as the laser power was increased from 200 W to 400 W.

The variation in the hardness of the melted regions is presented in Table 5.2. The hardness of the substrate was measured to be 300 ± 15 HV. However, the hardness increased significantly after LSM. The hardness of LSM region ranged from 493 to 515 HV, and the laser power was found to have little influence. This improvement of

hardness can be attributed to microstructural changes such as phase transformations and refined microstructural features as a result of rapid cooling rates. The microstructure changes from lamellar (substrate) to massive γ-formation in the melt pool during LSM. However, the processing conditions which were used for the LSM samples have no significant effect on the hardness, primarily due to similar microstructural features exhibited in the melt pool of the samples processed at different laser processing parameters.

Table 5.2 Process conditions, melt pool dimensions, and microhardness values of the melted region

Power (W)	Velocity (mm/s)	Laser energy density (J/mm^2)	Melt pool length (µm)	Melt pool depth (µm)	Hardness (HV)
200	10	40	476 ± 42	65 ± 14	515 ± 9
300	10	60	850 ± 8	175 ± 4	508 ± 15
400	10	80	1120 ± 11	259 ± 7	493 ± 11

5.1.8   Influence of laser power on melt pool dimensions
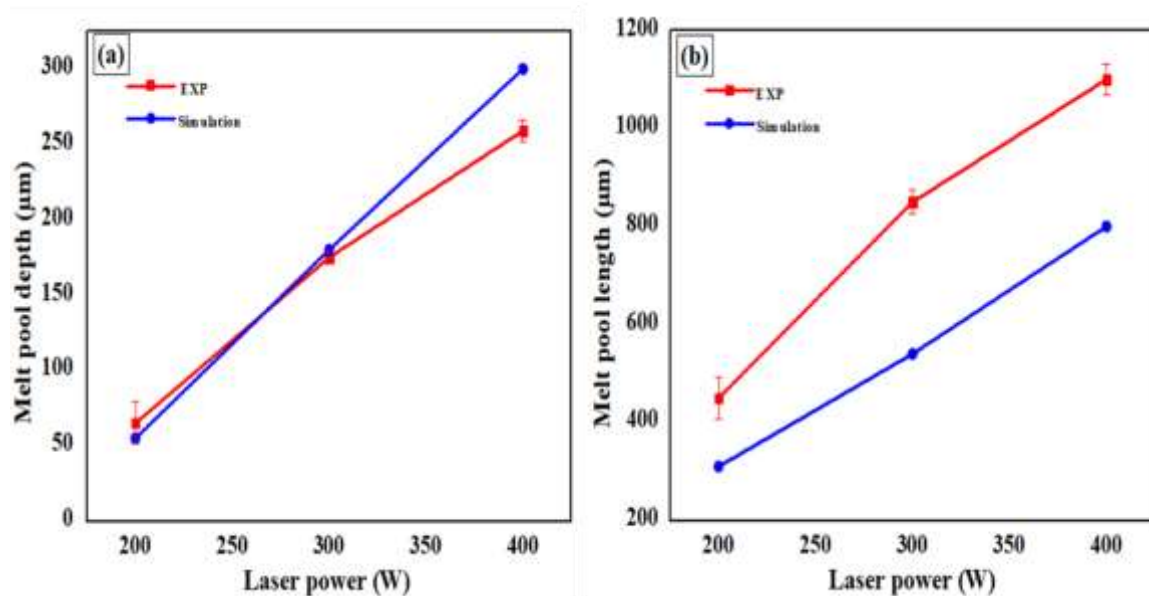
Figure 5.6 Influence of laser power on (a) Melt pool depth and (b) Melt pool length

Figure 5.2 presents the temperature contours in the melted region. The red coloured region in these contours indicates the melt pool region, i.e., the region where the temperature is greater than the liquidus temperature of the γ-TiAl alloy. The melt pool depth and length were measured from these contours and compared with the experimentally determined dimensions. From Figure 5.6 (a), it is evident that the measured and predicted values of the melt pool depth are in good agreement with maximum error of 13.6% at P = 400 W and V = 10 mm/s. Further, it can be seen that as the laser power increases from 200 to 400 W, the melt pool depth increases from 65 to 259 µm.

Figure 5.6 (b) presents the experimental and numerical predictions of the melt pool length as a function of laser power. From the plot, it is evident that the modeling results agree with the trend of the experimental data. However, the measured melt pool lengths were higher than the predicted values. The reasons for this discrepancy can be attributed to the assumptions made in the thermal analysis (Balichakra et al. 2016).

5.1.9 Determination of laser absorption coefficient (α_A) of γ-TiAl alloy

As discussed earlier, the focus of the present work is to determine the laser absorption coefficient of the γ-TiAl alloy. The laser absorption coefficient is determined by comparing the measured (SEM) and the simulated melt pool depths. This procedure is analogous to the one used by Chad Brown in his work to determine the laser absorption coefficient of Titanium alloy Ti-6Al-4V. In the current work, finite element simulations were run for different values of α_A, starting with $\alpha_A = 0.35$, which is the laser absorption coefficient of Ti-6Al-4V. The value of α_A is successively decreased and the corresponding melt pool depths are compared with the measured ones. This process is repeated until the FEM predictions of the melt pool depths are close to the measured values. An α_A value of 0.13 gave the best agreement between the FEM predictions and the measured values of the melt pool depth for the different processing conditions considered in the present study. The measured melt pool depths and the FEM results for $\alpha_A = 0.13$ are reported in Figure 5.6 (a) (Balichakra et al. (2019a)).

5.2 Summary of the chapter

The current work focuses on numerical modeling and experimental study of the laser surface melting of the γ-TiAl alloy mainly to determine the absorption coefficient and to understand the cracks in the samples. The following conclusions were drawn from this chapter:

- As the laser power increased from 200 to 400 W, the melt pool dimensions also increased;
- Maximum Von Mises stress was predicted along the laser travel direction due to high thermal gradients;
- The predicted Von Mises stress of 596 MPa exceeded the yield strength (400 MPa) of the γ-TiAl alloys;
- The microstructure of the substrate was fully lamellar and transformed to predominantly γ-TiAl with little traces of α_2-Ti$_3$Al phases after LSM;
- The hardness improved in the melted region from 300 ± 15 HV to 515 ± 9 HV due to phase transformation and higher cooling rates;
- Microcracks were observed in all the melted regions due to high tensile stress in these regions, which exceeded the yield strength (400 MPa) of the material;
- The laser absorption of the γ-TiAl alloys was determined using a combination of simulation and experimental approaches and was found to be $\alpha_A = 0.13$; and
- The measured and predicted values of the melt pool depth are in good agreement with a maximum error of 13.6%.

CHAPTER 6

6   LASER METAL DEPOSITION OF γ-TiAl THIN-WALL STRUCTURES

This chapter presents the results of the numerical modeling and experimental study of laser metal deposited γ-TiAl alloy thin-wall structures. The thin-wall structures considered in this thesis are assumed to be fabricated with deposition of a single track in each layer (i.e., single track, multi-layer deposition). The same assumption (single track in each layer) was used during the simulation of thin-wall structures. The results from both the numerical modeling and the experimental work are discussed in detail herein.

6.1   3-D transient thermomechanical analysis of thin-wall structures

Table 6.1 Details of thin-wall dimensions, finite element model, and simulation

Parameter	Details
Dimensions: Substrate, thin-wall	L30×W10×H2 mm³, L15×W0.5×H2.5 mm³
Element size of the layer (L), substrate (S)	0.125 mm (L), 0.125 and 1.66 mm (S)
Type of element	Thermal SOLID70, Structural SOLID185
No. of nodes, elements	23635, 19,440
No. of layers, layer height, length	10, 0.25 mm, 15 mm
Laser beam diameter	0.5 mm
Scanning patterns	Unidirectional

6.1.1   Description of FE model

A meshed model is shown in Figure 6.1, and represents the γ-TiAl alloy specimen built using the APDL pre-processor. The SOLID70 element is used to mesh a thin-wall geometry. The model consists of 10 layers representing the total build height of 2.5 mm with each layer of thickness 0.25 mm. Each layer was subdivided into group size of 0.5 mm x 0.5 mm x 0.25 mm consisting of 32 elements, including two rows along the height. The element groups were activated based on the time interval and movement of

the laser heat source. The substrate was modelled with coarse mesh with four layers of elements. The entire FE model consisted of 19,440 elements and 23,635 nodes.

No. of Nodes	23,635
No. of Elements	19,440
Thermal Element	SOLID70
Structural Element	SOLID185
No. of Layers	10
Layer Height (mm)	0.25
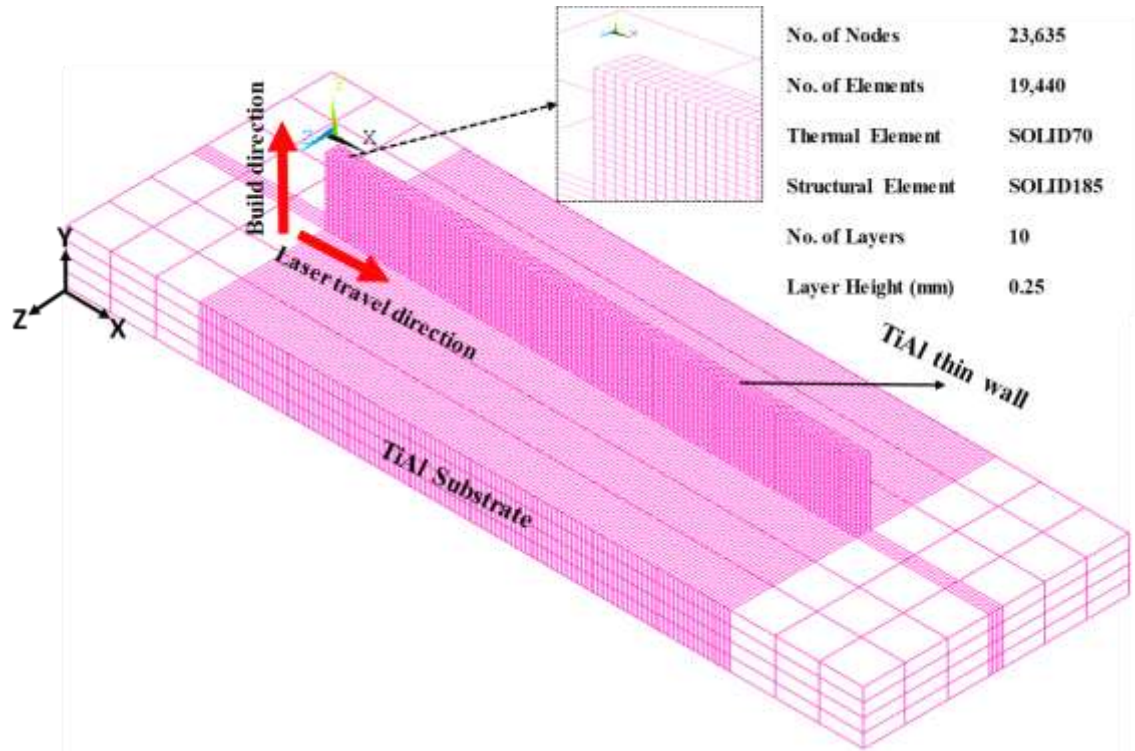
Figure 6.1 Finite element model of thin-wall structure built on a substrate

6.1.2 Gaussian distribution of heat flux
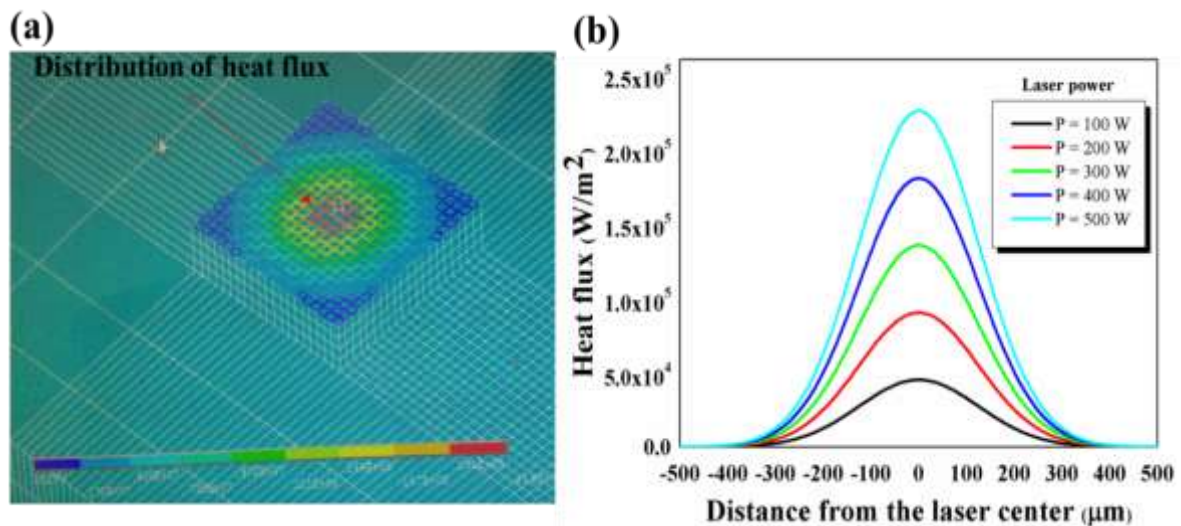
Figure 6.2 (a) Heat flux applied on a small region on the surface of the thin-wall

(b) Heat flux magnitude and distribution for various laser powers

56

The laser beam traverses from the left to the right end (unidirectional scan) of the FE model with velocity V. The movement of the laser beam was taken into account using a moving coordinate system. The heat flux was applied using Equation (4.1) over a 0.5 × 0.5 mm² surface area of the elements, as shown in Figure 6.2 (a). The distribution of the heat flux at different laser powers is shown Figure 6.2 (b). As the laser power increased from 100 to 500 W, the peak intensity of heat flux was found to increase from 45104 W/m² to 225340 W/m². It was observed that as the laser power increased, the heat flux increased at the centre of the laser beam. This heat flux diminished by $1/e^2$ as it radially moved outward from the centre of the laser beam.

6.1.3   Melt pool dimensions
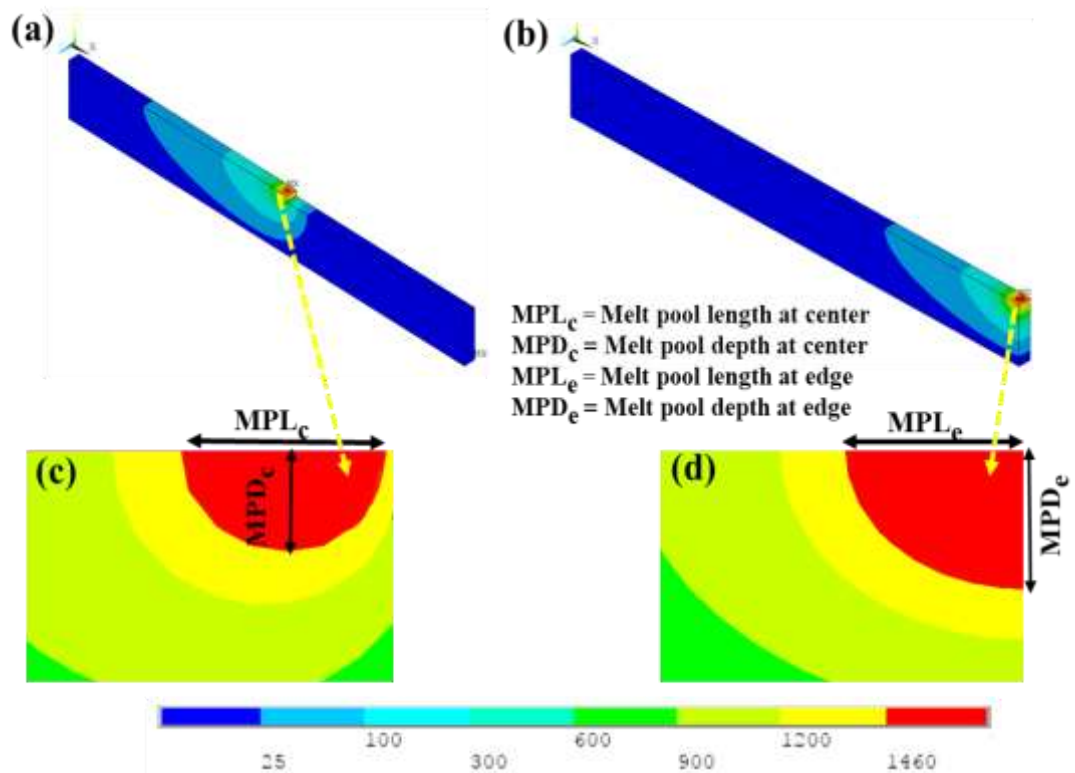
Figure 6.3 Temperature contours (a, b) and melt pool size (c, d) as a function of laser beam location on the thin-wall during deposition of the last layer with P = 200 W, V = 8 mm/s

The temperatures and melt pool dimensions were extracted from finite element models during the deposition of the last layer, both at the centre and also at the free edge of the wall. The temperatures and melt pool contours predicted for P = 200 W and V = 8 mm/s

are shown in Figure 6.3. As illustrated in Figure 6.1, for a single layer, the scan path of the laser beam starts at the left edge and ends at the right free edge of the wall. An increase in both melt pool dimensions and temperatures are observed as the laser beam approaches the free edges of the wall due to the decreased area available for the conduction of heat. An observation of Figure 6.3 (a) and (b) reveals that the maximum temperature at the free edge temperature (3104 °C) is higher compared with that at the centre of the wall (2643 °C). The melt pool depth at the centre (MPD$_c$) is 0.3125 mm (Figure (c)), whereas it is 0.7625 mm at the free edge (MPD$_e$) (Figure 6.3 (d)). The thermal gradients at the free edge are higher in magnitude compared with that at the centre of the wall. This is due to the higher temperatures at the free edge. Further, the temperatures within the melt pool increase as the laser power increases (Balichakra et al. 2019b).

6.1.4 Temperature cycling
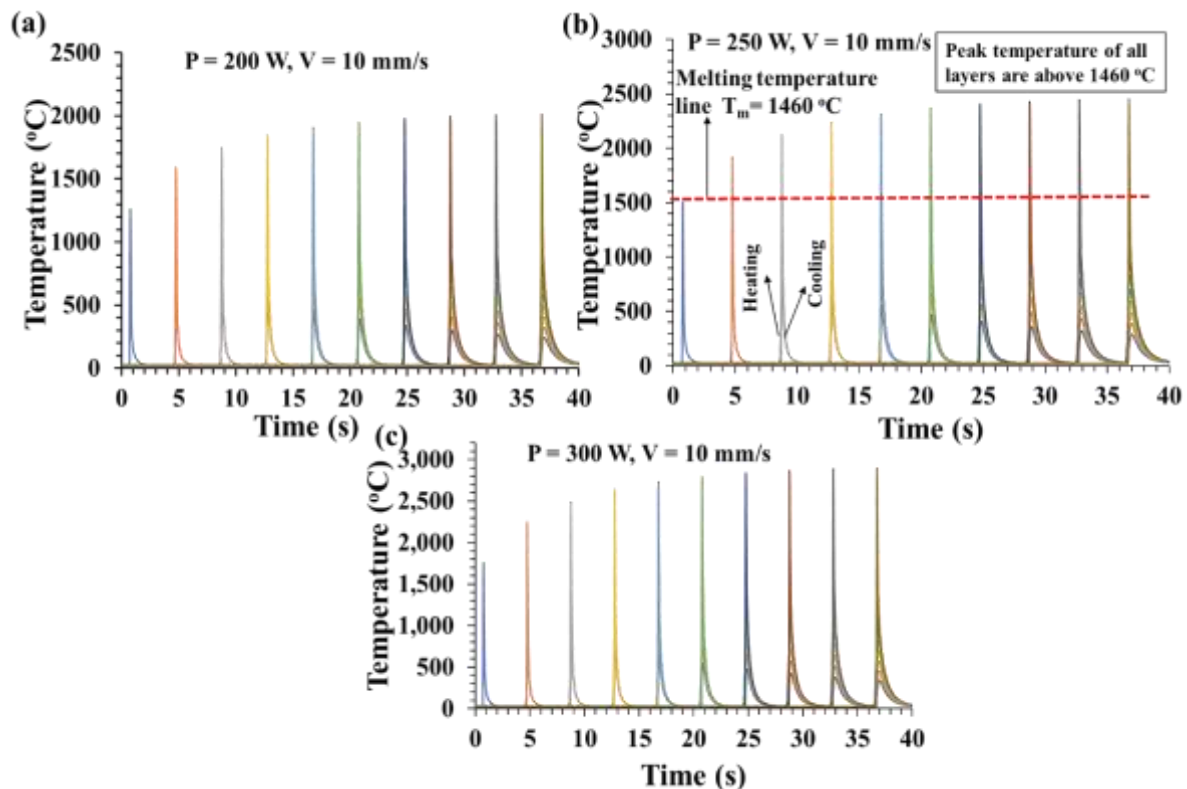
Figure 6.4 Variation of temperature with time at the centre of each layer for various laser powers (a) 200 W (b) 250 W, and (c) 300 W

The variation of temperature with time at the center of each layer is shown in Figure 6.4 (a), (b), and (c) corresponding to the 200-10, 250-10, and 300-10 conditions. The laser beam moves over a predefined location. The temperature at that location reaches the maximum value, i.e., above the melting temperature. After the laser beam passes by, the temperature quickly reduces due to solidification. It is seen that the temperature at the upper layers is significantly higher than that of the lower layers. This is because the substrate acts as a heat sink and conducts the heat away from the layers. Therefore, the first layer has the lowest temperature. The temperature gradually increases in the subsequent layers. As the number of layers increase, the temperature of the consecutive layers remains almost the same, as the effect of the substrate becomes negligible.

Also, the temperature at different layers exhibits quite a similar thermal profile, indicating that each layer undergoes similar thermal cycling. The trend of the estimated temperature cycles follows those reported in the existing literature (Wang et al. 2007; Ge et al. 2018). It was observed that three process conditions follow the same trend. Temperature magnitude was increased as the laser power increased from 200 W to 300 W at a constant travel speed of 10 mm/s.

6.1.5 Thermal gradients

The influence of laser power and travel speed on thermal gradients is shown in Figure 6.5 (a) and (b). Here, the gradients were extracted along the build direction at the centre of each layer of the thin-wall. Figure 6.5 (a) shows the gradients at different laser powers at constant travel speed (V = 10 mm/s). The magnitude of the thermal gradient increases from the first layer to the last layer. Lower thermal gradients in the bottom layers can be attributed to the rapid heat extraction by the substrate, which acts as a heat sink and conducts the heat away from the melt pool. However, as the number of layers increase, the effect of the substrate diminishes and therefore, the thermal gradients increase. Sammons et al. (2013) reported a similar trend of thermal gradients along the build direction. Table 6.2 presents the thermal gradients in the first and last layer of the deposition for all the simulated cases.

Further, the thermal gradients were found to increase as the laser power increases from 200 W to 300 W (refer section 6.1.2). Thermal gradients are the lowest for 200-10 and the highest for the 300-10 conditions. Figure 6.5 (b) depicts the gradients for various

travel speeds at constant power (P = 200 W). The trends in variation of the thermal gradients with travel speed are analogous to that reported for variation in laser power. The thermal gradients reported in Table 6.2 are in agreement with thermal gradient values reported for LAM processes in the literature (Xia et al. 2016; Zhang et al. 2015).

Table 6.2 Thermal gradients in the first and last layer of deposition

Laser power-travel speed (W-mm/s)	Thermal gradient (°C/mm) in 1st layer (near to substrate)	Thermal gradient (°C/mm) in 10th layer (topmost layer)
200-8	6,614	11,284
200-10	6,484	10,878
200-12	6,360	10,284
200-10	6,484	10,878
250-10	7,767	13,425
300-10	9,109	15,714
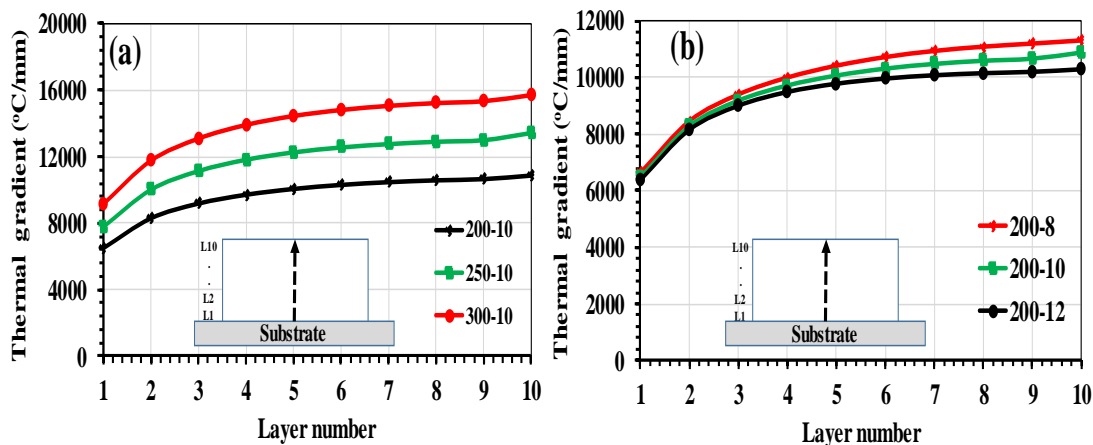
Figure 6.5 Variation of thermal gradients in different layers during thin-wall deposition (a) Influence of laser power, and (b) Influence of travel speed

6.1.6 Cooling rates

The cooling rates for various laser powers and travel speeds are shown in Figure 6.6 (a) and (b). Here, the cooling rates were extracted along the build direction at the centre of each layer of the thin-wall. The trend of the cooling rates is opposite to the thermal gradients. Figure 6.6 (a) shows the cooling rates at different laser powers (200, 250, and 300 W) at constant travel speed (V = 10 mm/s). The magnitude of the cooling rate decreases from the first layer to the last layer. Higher cooling rates in the vicinity of the

bottom layers can be attributed to the substrate effect. However, as the number of layers increases the effect of the substrate reduces and therefore, the cooling rates decrease. The trends are in agreement with those reported in the existing literature that cooling rates decrease with increasing laser power (Liu et al. 2018; Manvatkar et al. 2011).

Further, the cooling rates were found to decrease as the laser power increased from 200 to 300 W at constant travel speed 10 mm/s. The cooling rates were highest for 200-10 and lowest for the 300-10 process conditions. The predicted cooling rates are in agreement with those reported in the literature (Balla et al. 2016; Roberts 2012a; Yin et al. 2008; Liu et al. 2018).
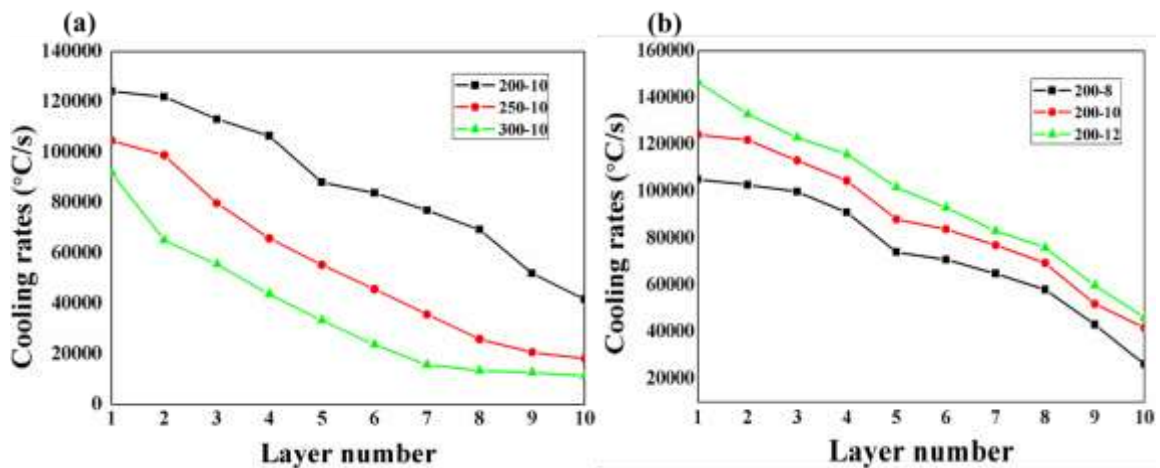
Figure 6.6 Variation of cooling rates in different layers during thin-wall deposition (a) Influence of laser power, and (b) Influence of travel speed

Table 6.3 Cooling rates in mid-length of the first and last layer

Power-Travel speed (W-mm/s)	Cooling rates ($^{\circ}$C/s) in 1st layer	Cooling rates ($^{\circ}$C/s) in 5th layer
200-10	124270	41768
250-10	104611	18245
300-10	91702	11475
200-8	105154	26284
200-10	124270	41768
200-12	146683	46224

Figure 6.6 (b) presents the cooling rates for various travel speeds (8, 10, and 12 mm/s) at constant power (200 W). The trends in variation of the cooling rates are analogous

61

to that reported for variation of laser power. It was observed that travel speeds were showed greatest influence on developing higher cooling rates. Hence, the prediction of the cooling rates during LMD enables better control of the microstructures and mechanical properties (Balla et al. 2016; Srivastava et al. 1999; Tlotleng 2018).

6.1.7   Mechanical analysis of the thin-wall

The LMD of the materials involves several reheating and cooling cycles during the layer-by-layer deposition. This results in rapid cooling rates and high-temperature gradients, which often causes significant thermal stresses leading to warpage. Further, under some conditions, the parts can develop cracks during or immediately after deposition (Balla et al. 2016). Therefore, understanding the effect of the process parameters on the magnitude and distribution of the residual stresses is critical both for manufacturing defect-free parts as well as to minimize stress-induced warpage. This understanding is even more important for an intermetallic such as γ-TiAl, which is the material under consideration in the present study. In the present work, a mechanical analysis was carried out using thermal histories obtained from the transient thermal analysis to estimate the residual stress and distortion during the deposition of thin-walls under different process conditions.

6.1.8   Influence of laser power and travel speed on magnitude and distribution of residual stresses

Figure 6.7 (a), (b), (c), (d), (e), and (f) shows the stress distribution contours in the thin-wall after cooling to room temperature. Figure 6.7 (a), (b), and (c) were plotted for different laser powers (P= 200, 250, and 300 Watts) at constant travel speed V = 10 mm/s. In all cases, tensile stresses were present both at the edges as well as at the top surface of the wall. This is due to expansion and contraction. On the other hand, compressive stresses were present in the inner regions of the thin-wall. Further, the magnitude of the residual stress increased marginally with the increase in the laser power from 200 to 300 W at constant travel speed. This is due to the increase in thermal gradients with the increased in power (refer Figure 6.5 (a) and section 6.1.2). Although stress distribution may appear symmetric in the contour plots, a close observation shows peak tensile stresses at the right edge of the wall. This can be attributed to the scanning

path where the laser traverses from the left to the right edge. If the magnitude of tensile stress in the thin-wall exceeds the yield strength of the γ-TiAl, it may lead to cracking or delamination.
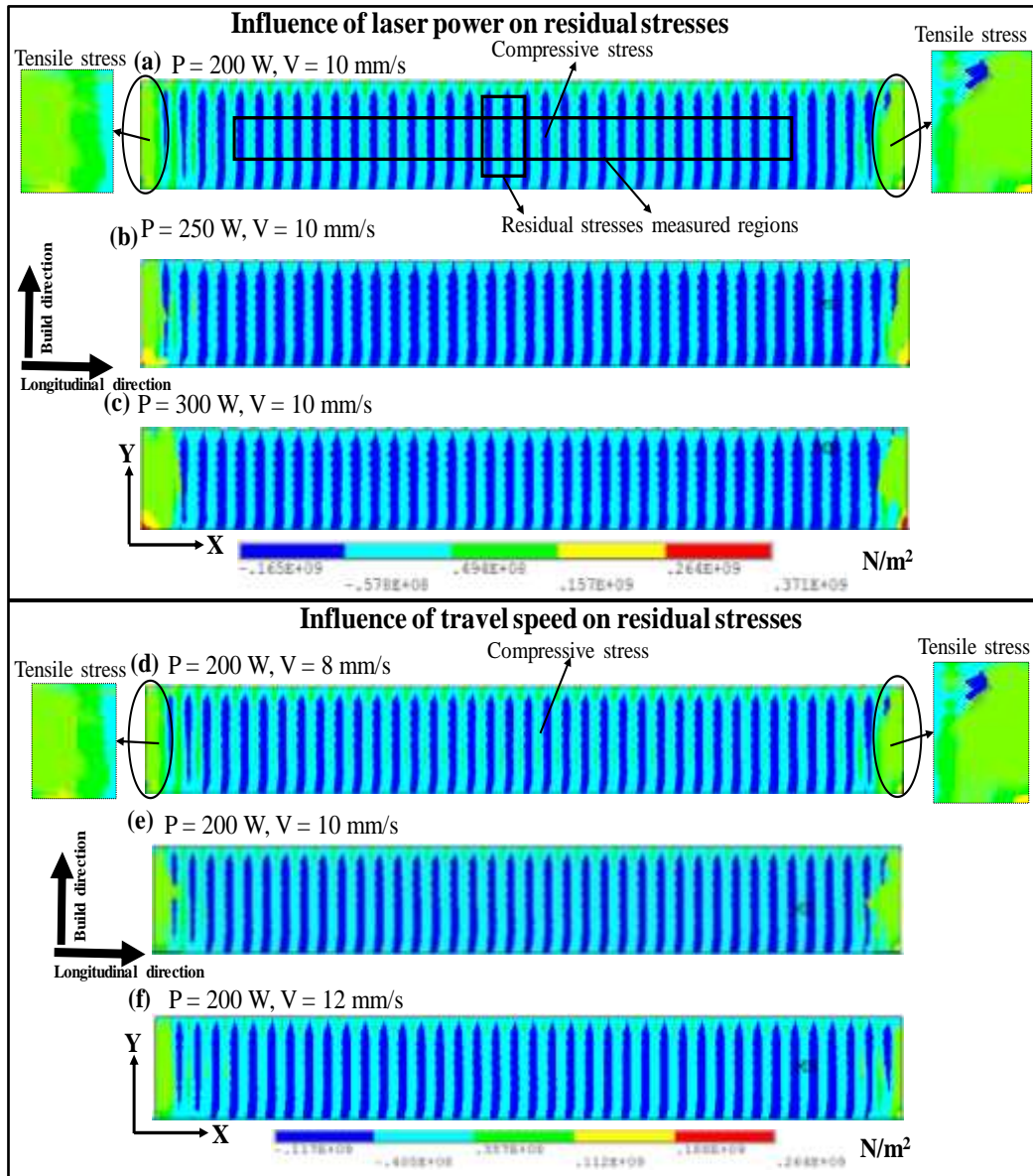
Figure 6.7 Contour plots showing the influence of laser power (a, b, c) and travel speed (d, e, f) on the distribution of residual stresses in γ-TiAl thin-wall structures

The contours shown in Figure 6.7 (d) (e), and, (f) were plotted for different travel speeds (V = 8 mm/s, 10 mm/s, and 12 mm/s) at constant power of 200 W. It can be seen that the trends of stress distribution are analogous to that observed for variation of power at constant travel speed. However, the stress contours for varying travel speed did not

show any substantial difference in magnitude. This can be attributed to the fact that the difference in travel speeds considered in the present study is only 2 mm/s (Balichakra et al. 2019b).

During cooling, thermal contraction takes place at the edges as they are free to contract, which is not the case with the material at the centre of the wall. As discussed earlier, the material at the free-edges of the thin-wall is at higher temperatures compared with the material at the centre of the wall. As a result, the hotter free edges start shrinking owing to the reduction in temperature leading to strain mismatch between the edges and the centre of the thin-wall. Plastic deformation occurs at the free edges as the developed thermal stress exceeds the yield strength of the material. This plastic deformation results in relieving the initially induced compressive stresses at the edges. After completion of cooling, the shrinkage at the edges is higher due to solidification and plastic deformation. Thus, tensile stresses are generated at the edges, while compressive stresses are generated at the centre region of the thin-wall. These results are in agreement with those reported in literature by Rangaswamy et al. [8] and Wang et al. [14].

6.1.9 Preheating effect
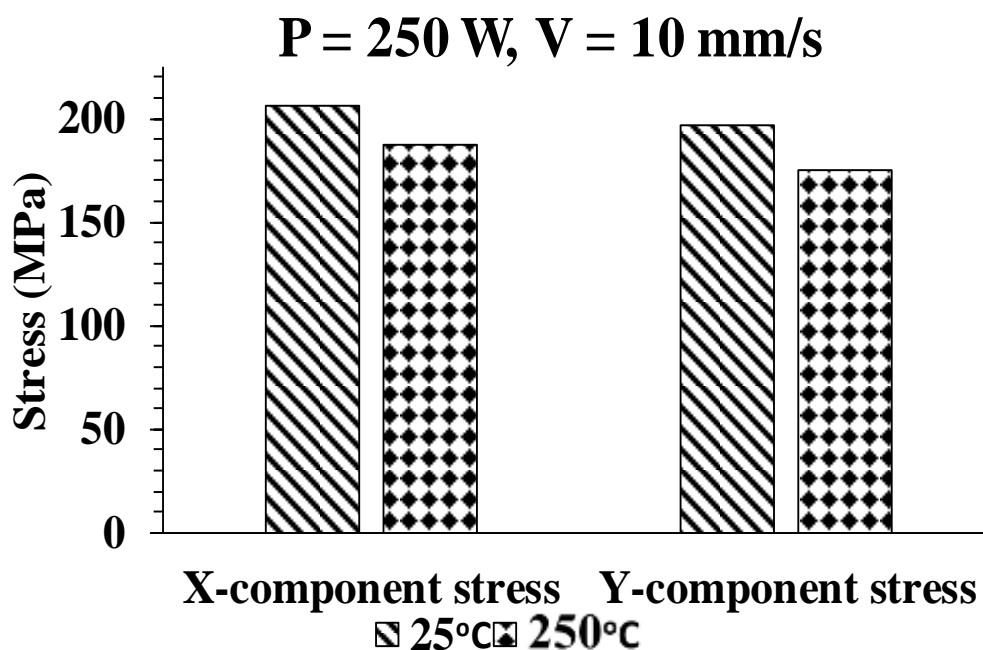
Figure 6.8 Influence of substrate preheating on residual stress

64

In the LMD process, residual stresses are generated due to thermal gradients. The generated residual stresses affect the part performance, cracking, and premature failure. Hence, the reduction of residual stress in a component is essential. These residual stress magnitudes can be reduced by preheating the substrate (Kai Zhang et al. 2014 and Vasinonta et al. 2000). To see the effect of preheating on residual stress development in the LMD of the γ-TiAl thin-walls. A thermomechanical FE model of thin-wall with substrate preheating was performed. The substrate was preheated from room temperature 25 ºC to 200 ºC. The reduction of stresses was observed in the preheated substrate, as shown in Figure 6.8. The x and y-component stresses were found to be 187 and 175 MPa, which were lower than those of the non-preheated substrate of 206 and 197 MPa, respectively, (250 W, 10 mm/s). The preheating study demonstrates reducing stress levels in the LMD of the γ-TiAl components.

6.2   Experimental results

The following subsections present the results for experimental measurement of residual stress, powder morphology, microstructural analysis, phase analysis, and hardness values of the deposited thin-wall specimens.

6.2.1   Experimentally measured residual stresses

The stress distribution measured along the longitudinal and build directions of the different samples are shown in Figure 6.9-Figure 6.11. The stresses were measured along the longitudinal direction at height h = 10 mm and at the centre of the sample along the build direction. In all the nine thin-wall samples deposited, a total of six prespecified data points were considered with three points along the horizontal direction and three points along the vertical direction (Figure 4.4 b & c).

Figure 6.9-Figure 6.11 (a), (c), and (e) show that in the longitudinal direction (x-axis), the stresses are compressive. It is clear that maximum compressive stress develops in the centre of the sample, and as the distance increases from the centre, a small reduction in the compressive stress level is noticed near either edge of the samples. A similar trend is observed in the thin-wall samples 1-6 and sample 9. In general, the tensile residual stresses are present at either edge and the compressive stresses direct in the core portion of the thin-wall samples (Pratt et al. 2008; Rangaswamy et al. 2005). In

the present work, the stresses were measured at points 4 mm away from both the edges. These results highlight the variations in the stresses generated within the thin-wall samples. Meanwhile, a reverse trend is observed in the samples 7 and 8 (Figure 6.11 a, c), where maximum compressive stresses are observed at either edge with a decrease in compressive stresses at the centre of the sample. These variations may be attributed to material irregularities such as pores/inclusions in the sample.
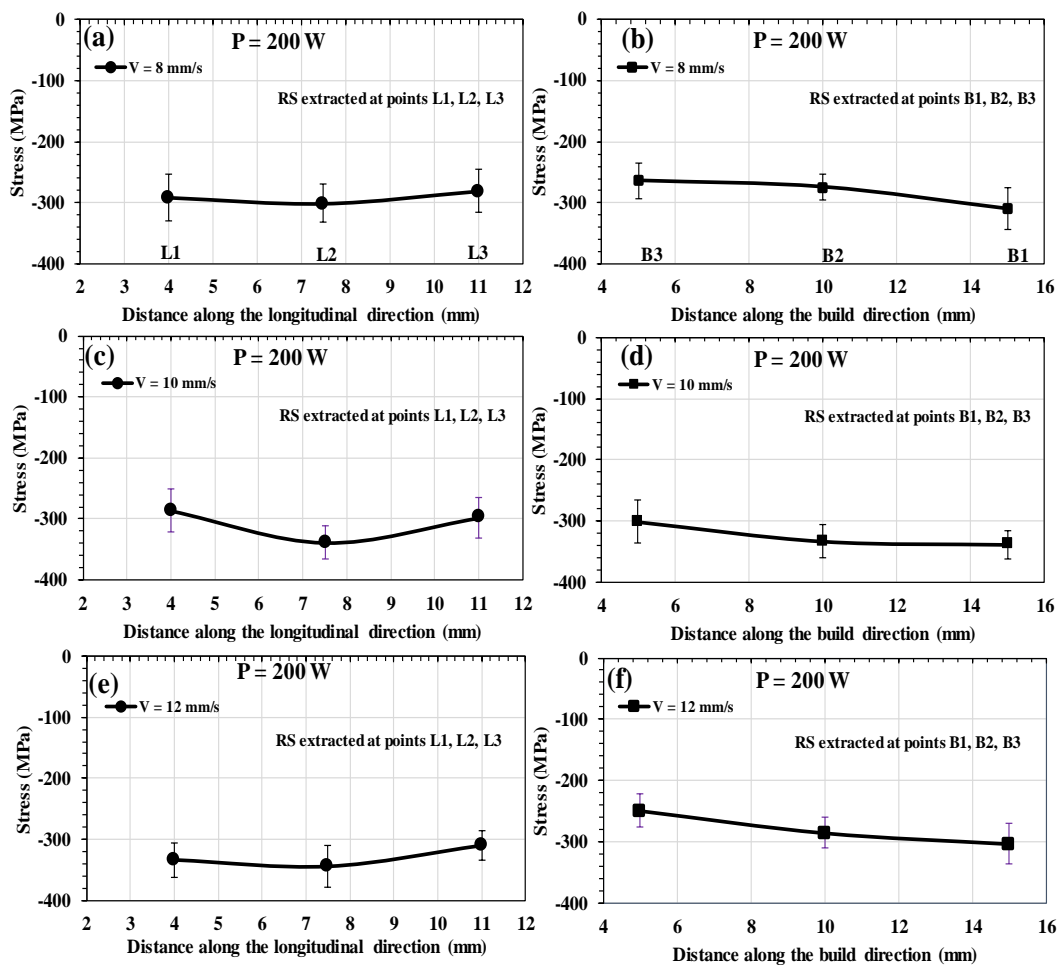
Figure 6.9 Stress as a function of location along the longitudinal and build directions (a) (b) Sample 1, (c) (d) Sample 2, (e) (f) Sample 3

Figure 6.9-Figure 6.11 (b), (d), (f) show the magnitude of the stresses developed along the build direction. All the samples exhibited compressive stresses in the build direction. The compressive stresses within the thin-wall structures increased towards the substrate from the topmost layers. However, with the increase in the number of layers being deposited, the build-up of residual stresses varied with higher compressive

stress in the layers very close to the substrate. The magnitude of these compressive stresses decreased with the increase in distance from the substrate (Rangaswamy et al. 2005; Sammons et al. 2013). However, samples 7 and 8 exhibited an opposite trend to that shown by samples 1-6 and 9 along the build direction as shown in Figure 6.11 (b) and (d). That is to say that the magnitude of the compressive stresses was higher at the edges compared with the centre of the wall. This is possibly due to the high surface roughness and irregularities present at the respective locations where the deviation in trend was observed in the samples. Similar reasoning has been provided in the literature for explaining the deviation in trends of stress results (Pratt et al. (2008).
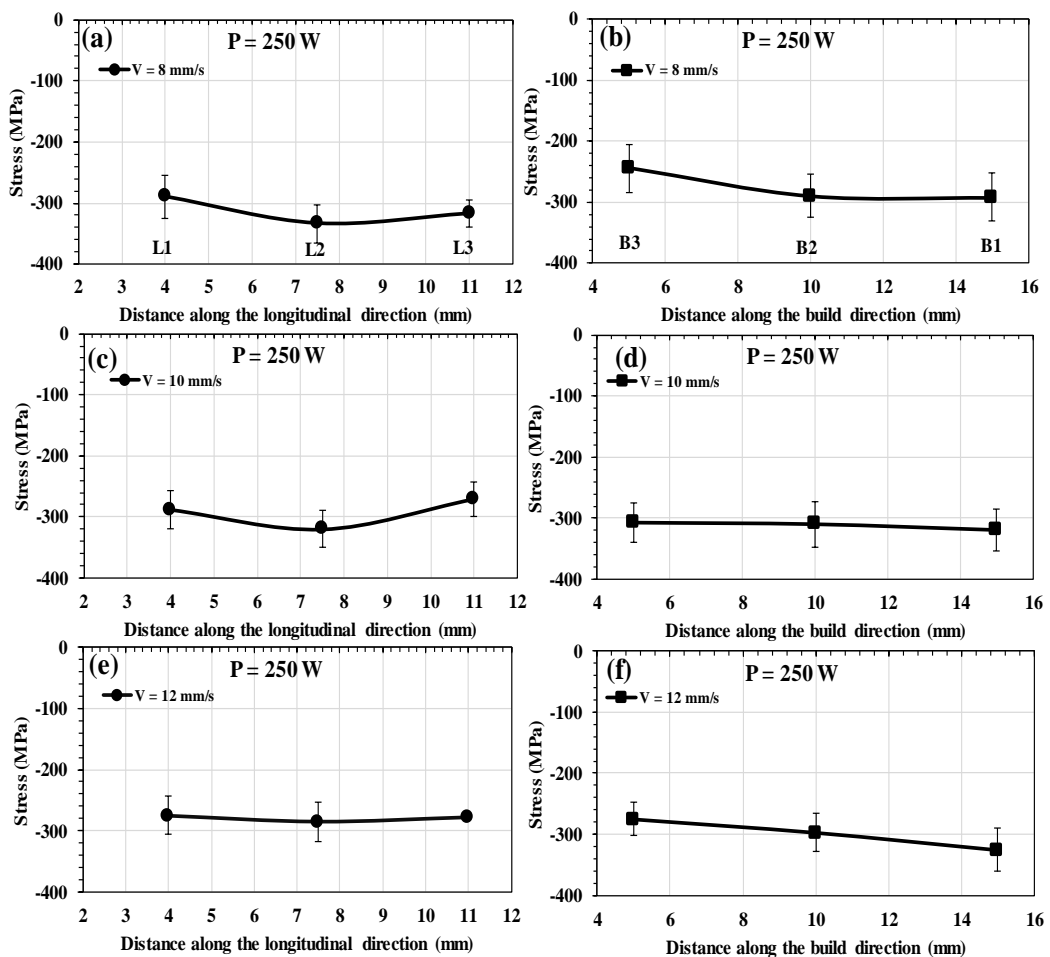
Figure 6.10 Stress as a function of location along the longitudinal and build directions (a) (b) Sample 4, (c) (d) Sample 5, (e) (f) Sample 6

Therefore, to understand material irregularities, a sample was cold mounted and polished according to metallurgical standards. The optical microscope images of an

unetched sample revealed defects such as pores/inclusions, as shown in Figure 6.13 (a) and (b). The pores observed in the optical micrographs were different in size and shape. The presence of defects in the deposited samples could be responsible for the measurement errors and deviations in the plotted trends of the stresses.
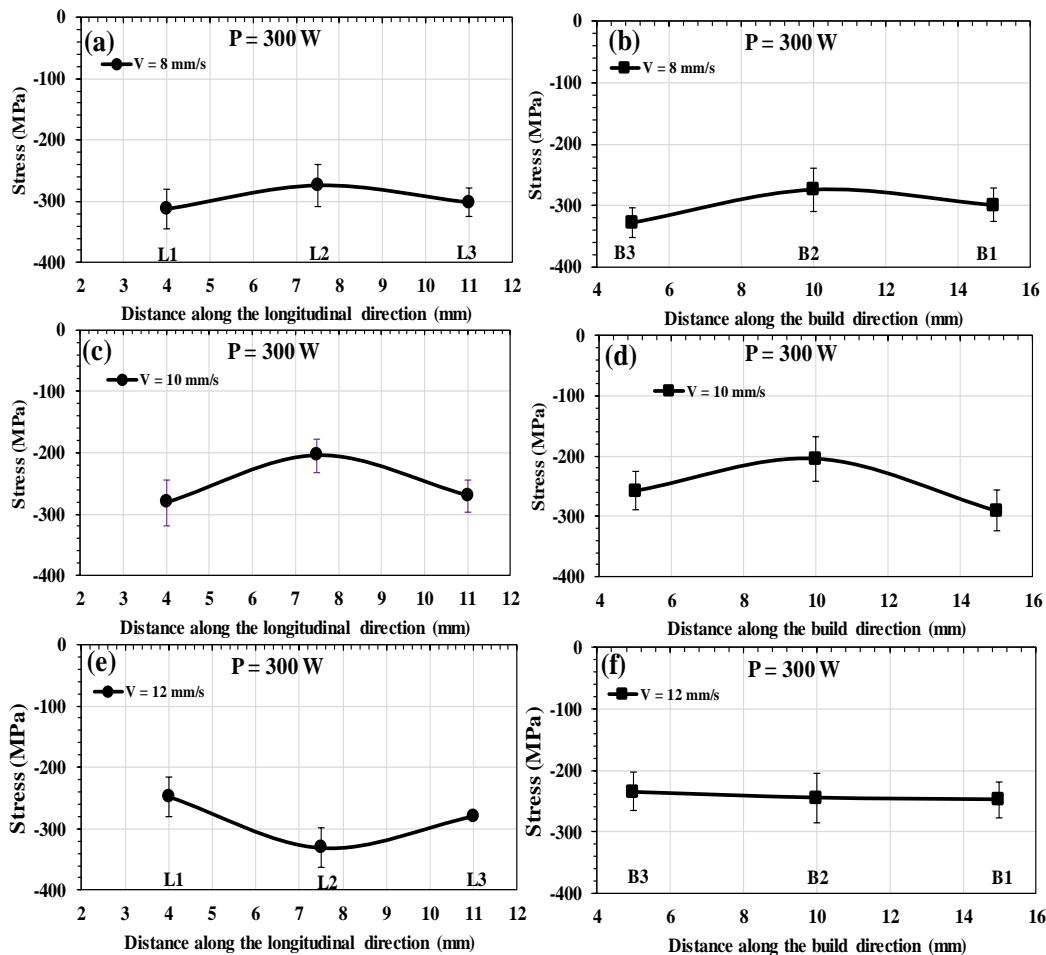
Figure 6.11 Stress as a function of location along the longitudinal and build directions (a) (b) Sample 7, (c) (d) Sample 8, (e) (f) Sample 9

Figure 6.12 shows the effect of laser power and travel speed on residual stresses. The results of Figure 6.12 (a) and (b) reveal that as the laser power increases from 200 to 300 W, the magnitude of the compressive stresses decreases. The results of Figure 6.12 (c) show that compressive stresses increase as the travel speed increases from 8 to 12 mm/s. The measured residual stresses in both the directions for the samples were 1-9, as presented in Table 6.4. It can be seen from Table 6.4 that the maximum compressive stresses in the samples were about 49%-79% of the yield strength of the γ-TiAl alloy.

68

However, the trends in the experimentally measured stresses reported in the present work in both the longitudinal and build directions showed good agreement with the existing literature (Pratt et al. 2008; Rangaswamy et al. 2005). Further, the reliability obtained during the residual stress measurements in the range of ± 40 MPa considered acceptable with respect to the attained stress measurements.
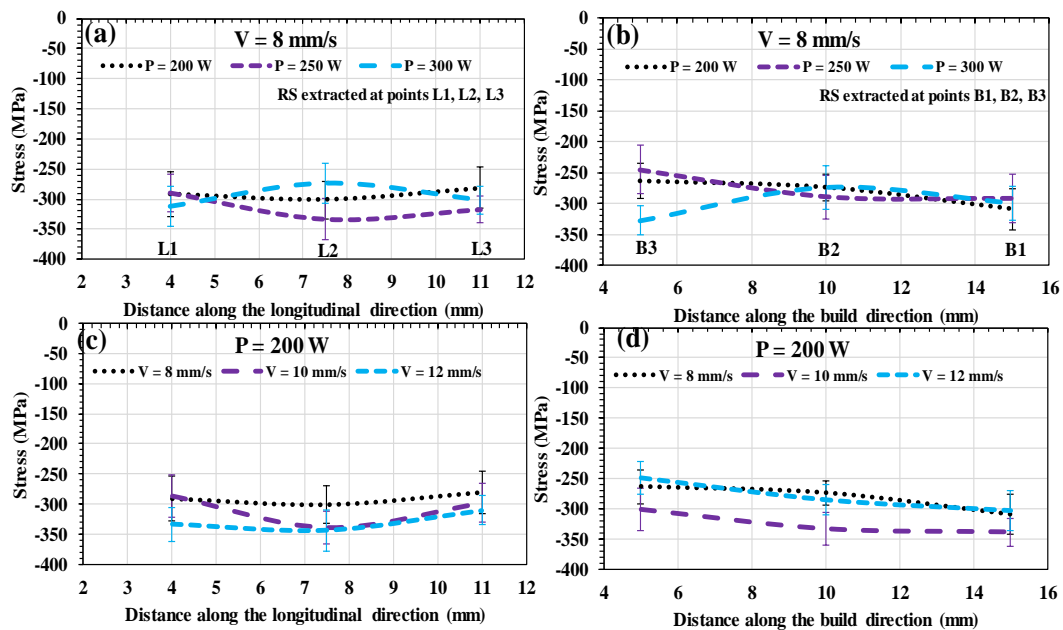
Figure 6.12 (a), (b), (c), (d) Stress as a function of location along the longitudinal and build directions demonstrate the effect of laser power and travel speeds
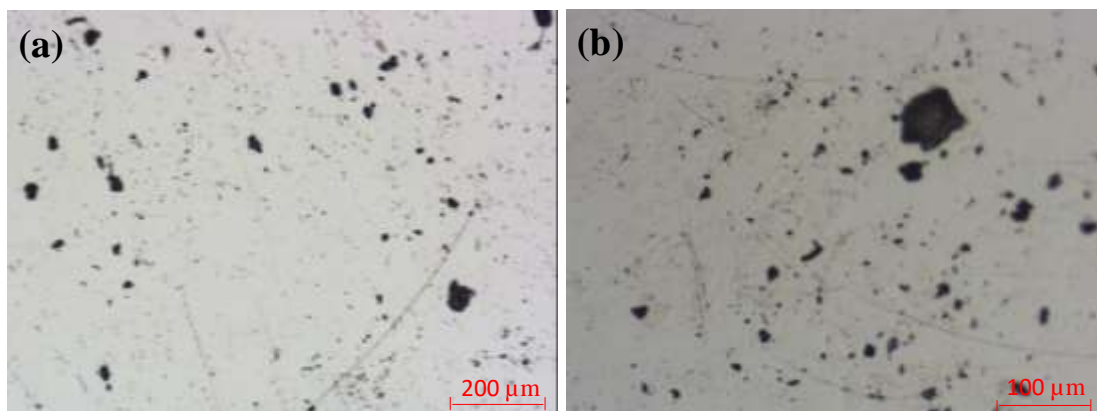
Figure 6.13 Optical micrographs showing porosity in the γ-TiAl thin-wall sample at different magnifications (a) 50 x and (b) 100 x

Table 6.4 Measured residual stresses in all thin-wall samples along longitudinal and build directions

Measured Points	L1	L2	L3	B1	B2	B3
Velocity (mm/s)	V = 8	V = 10	V = 12	V = 8	V = 10	V = 12
200 W	-291.4 ± 37.5	-286.1 ± 35.3	-333.7 ± 28.2	-263.9 ± 28.6	-301.2 ± 35.3	-249.5 ± 27.5
	-301.2 ± 31.3	-338.9 ± 27.5	-344.3 ± 33.8	-274.1 ± 20.7	-333.5 ± 27.5	-285.6 ± 24.6
	-281 ± 35.1	-298.1 ± 32.3	-310 ± 24.6	-309 ± 33.8	-338.9 ± 22.8	-303.4 ± 33.5
250 W	-289.5 ± 34.7	-288.1 ± 31.8	-274.8 ± 31.7	-244.9 ± 39	-307.2 ± 27.2	-274.7 ± 28.1
	-333.3 ± 31.2	-319.7 ± 30.7	-285.1 ± 31.9	-289.5 ± 34.7	-309.9 ± 30.7	-296.9 ± 31.7
	-317.3 ± 22.6	-271.1 ± 27.6	-277.5 ± 28.7	-292.2 ± 39.4	-319.7 ± 37.7	-325.6 ± 35.6
300 W	-312.3 ± 32.8	-281.4 ± 37	-248 ± 40	-327.6 ± 23.6	-257.2 ± 31.4	-234.1 ± 31.4
	-273.9 ± 34	-204.7 ± 27	-331 ± 38	-273.9 ± 35.1	-204.7 ± 37.3	-244.7 ± 40
	-301.6 ± 23.6	-270.1 ± 26.4	-279.7 ± 36.7	-299 ± 27.3	-290.4 ± 34	-248 ± 29.5

6.2.2 Comparison of modeling and experimentally measured residual stresses

Figure 6.14 (a) and (b) presents the qualitative comparison between the predicted and the experimentally measured stresses. The plots show stress distribution in samples 2, 5, and 8 along the longitudinal and build directions. The stress values were extracted from the simulated finite element models represented using data points, which were then curve-fitted using a polynomial function and are denoted by continuous lines. From Figure 6.14 (a) and (b), it can be seen that the predicted residual stress distribution follows a similar trend as the experimentally measured ones. Figure 6.14 (a) shows the stress distribution along the longitudinal direction of the thin-wall. Here, the numerical modeling results are plotted along the length of the sample. The results show tensile stresses at the edges and compressive stresses in the core. The compressive stresses in core of the wall are balanced by tensile stresses present at the edges of the thin-wall (Ma 2015). This is due to the imposed thermal gradients and plastic deformation. Further, a comparison of the trends in stresses obtained from the numerical models and the experimentally measured ones show a good agreement.

Figure 6.14 (b) shows the predicted and measured residual stresses along the build direction of the samples. The numerical modeling predictions of the stress distribution in the build direction reveal tensile stresses in the topmost layer of the wall, and compressive stresses in the rest of the thin-wall. It was found that there is good agreement between the predicted and the experimental results. The discrepancy

between the predicted and the measured stress results can be attributed to the assumptions (neglection of convection, radiation and Marangoni effect, etc.) made in the numerical models. Further, the predicted stress distribution trends are in good agreement with those reported in literature (Pratt et al. 2008; Wang et al. 2008a).
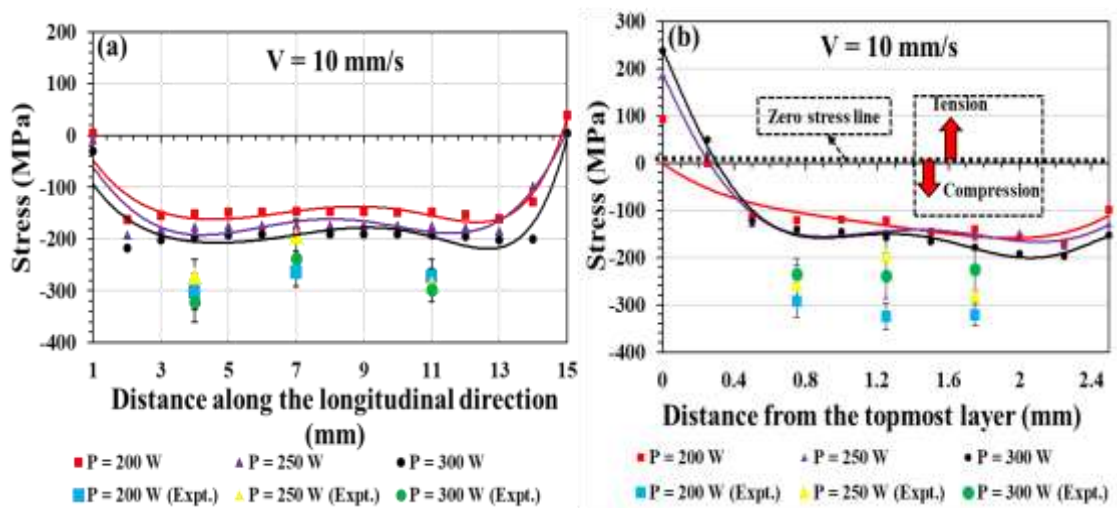
Figure 6.14 Comparison of stress results obtained from numerical modeling and experimental measurements (a) Along longitudinal direction and (b) Along build direction for different laser powers

6.2.3 Delamination of thin-wall from the substrate
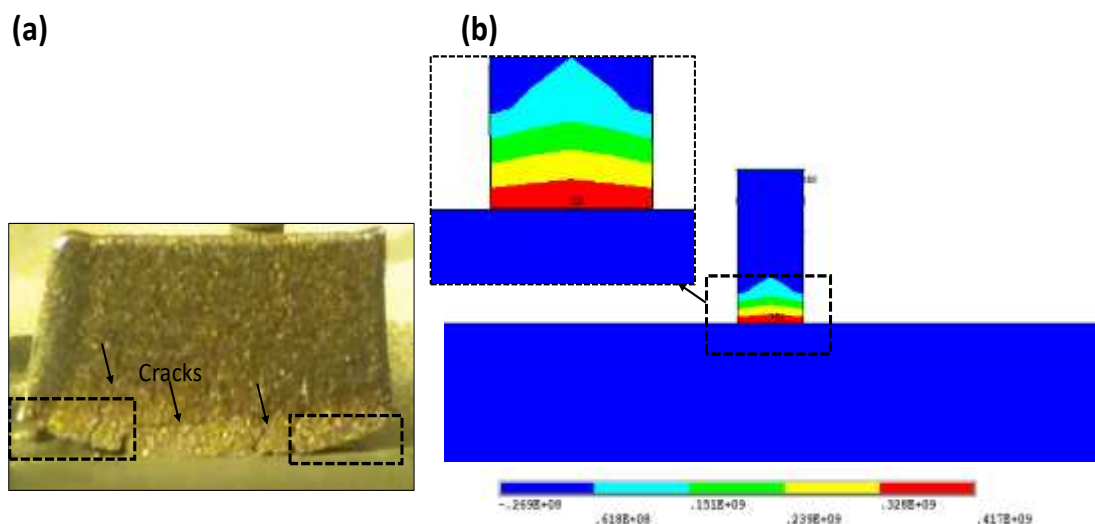
Figure 6.15 (a) LMD deposited γ-TiAl thin-wall with delaminated edges from the substrate and (b) Build direction stress contour

71

The deposited thin-walls delaminated from the substrate at certain processing conditions (P = 350 W, V = 10 mm/s). This delamination of the wall is shown in Figure 6.15 (a). For this processing condition, the thermomechanical finite element models (Figure 6.15 (b)) predicted a maximum tensile stress of 417 MPa at the interface between the substrate and the wall. This maximum value of stress (417 MPa) is higher than the yield strength (400 MPa) of the material resulting in delamination at either edge of the thin-wall. This illustrates the utility of the computational modeling results to understand the delamination in the deposited samples.

6.2.4 Powder morphology and composition
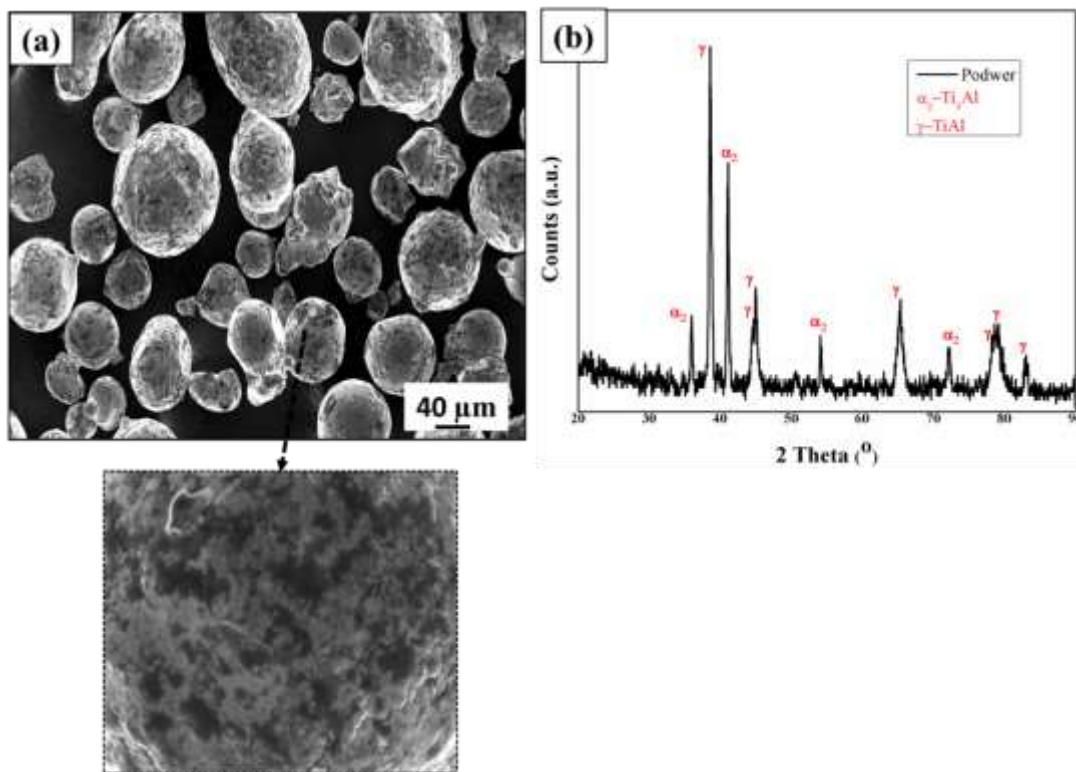
Figure 6.16 (a) SEM image and (b) XRD spectra of γ-TiAl powder

The morphology of powder particles was studied using both SEM (equipped with EDS) and XRD, and the results are shown in Figure 6.16. The secondary electron images show nearly spherical powder particles (Figure 6.16 (a)). The composition analysis of both the powder particles as well as that of the as-deposited samples is reported in Table 6.5. From the table, it can be seen that there is no significant difference in the elemental composition between the precursor powder and the deposited material. However, a

maximum loss of approximately 4% of Al was found in the deposited samples. This loss of Al content helps in the formation of a fully lamellar microstructure (Thomas et al. 2017). The XRD analysis of the powder particles showed two phases: γ-TiAl and α_2-Ti_3Al (Figure 6.16 (b)).

Table 6.5 Chemical composition of powder and as-deposited sample

Element (at%)	Al	Cr	Nb	Ti
Powder	47.20±1.01	2.11±0.85	2.10±1.02	48.59±0.45
200-10	46.23±0.35	2.53±0.22	2.72±0.11	48.53±1.22
250-10	45.17±1.1	1.32±0.85	3.10±1.34	50.41±1.33
300-10	45.53±0.43	1.49±0.75	3.93±0.1	49.15±0.63

6.2.5 Surface roughness
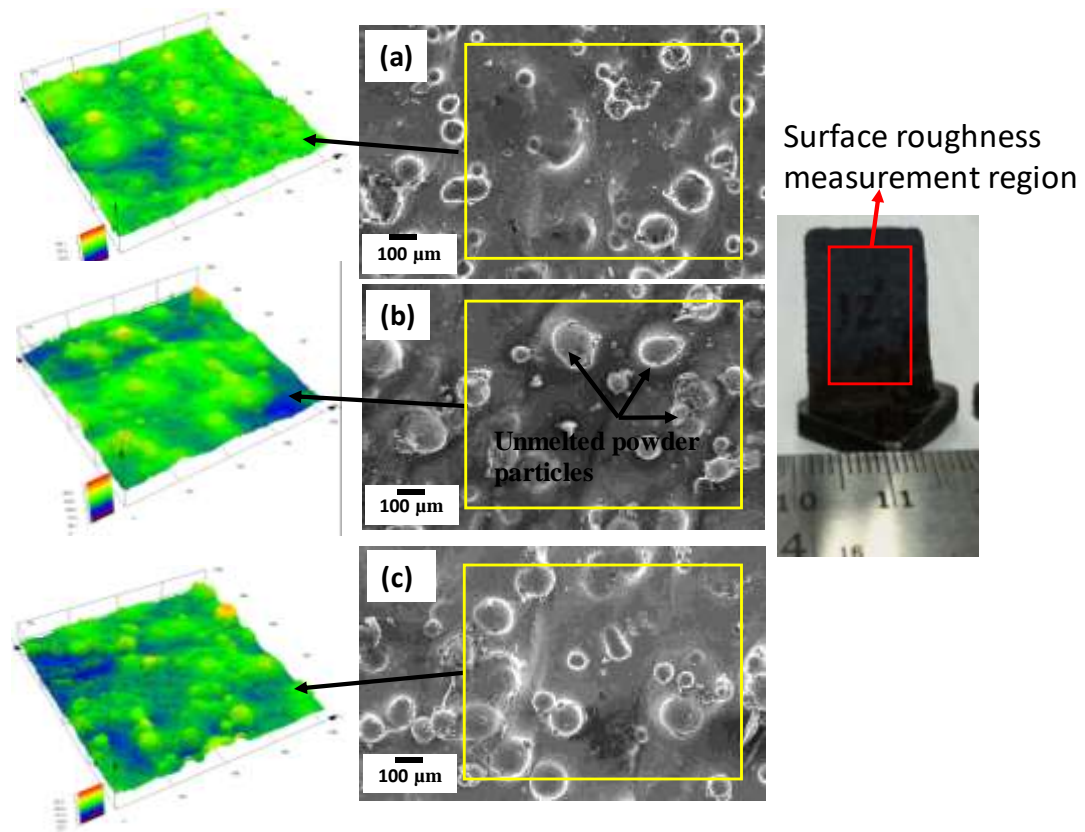
Figure 6.17 3D profiles and SEM images of samples for (a) 200-8 (b) 200-10 and (c) 200-12

73

The roughness of deposited thin-walls were measured using a LEXT 3D laser microscope, OLS4000, Japan and confirmed with SEM analysis. The SEM images with a 3D surface profile of thin-walls are shown in Figure 6.17. From Figure 6.17, it is evident that all thin-wall surfaces contain unmelted powder particles, which contributed to increase in surface roughness. Surface area roughness parameter (Sa) varied between 24.98 ± 1.07 µm to 27.98 ± 2.32 µm with increase in travel speed (8-12 mm/s) at constant power (200 W). The roughness decreased from 25.05 ± 1.92 to 23.72 ± 1.58, as the laser power increased from 200-300 W at a constant travel speed 10 mm/s. The increase in travel speed resulted in an increase in surface roughness. This can be attributed to a decrease in energy density available to melt the powder, resulting in partial melting. Further, the roughness value decreased with increase in laser power, which is due to the higher energy density available to melt the powder.

6.2.6 Microporosity
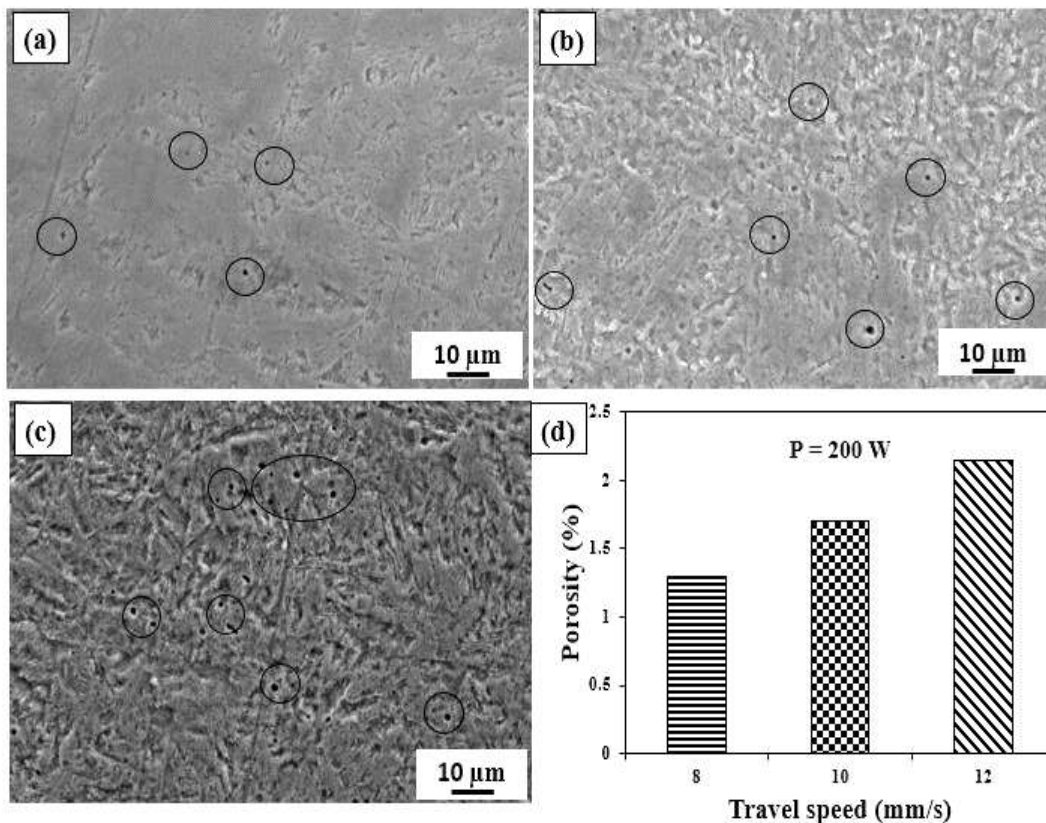
Figure 6.18 SEM images of pores at high magnification for (a) 8 mm/s (b) 10 mm/s (c) 12 mm/s and (d) Effect of travel speeds on pore size

74

Figure 6.18 (a), (b), and (c) illustrate the effect of travel speed at constant power on microporosity in LMD deposited samples. The porosity in the samples was measured using image analysis. It was found that a small percentage of porosity (in the range of 1.3 to 2.1%) was present in the deposited samples. As the travel speed increased from 8 to 12 mm/s, the porosity percentage in the samples increased, which can be attributed to the lower energy density available to the melt the powder (Wang et al. 2008b). Furthermore, gas entrapment in the powder during deposition generated porosity in the samples (Biamino et al. 2011; Tlotleng 2018). It was also observed that the porosity decreased with the increase in power due to the higher energy density available to the melt powder particles.

6.2.7 Microstructure
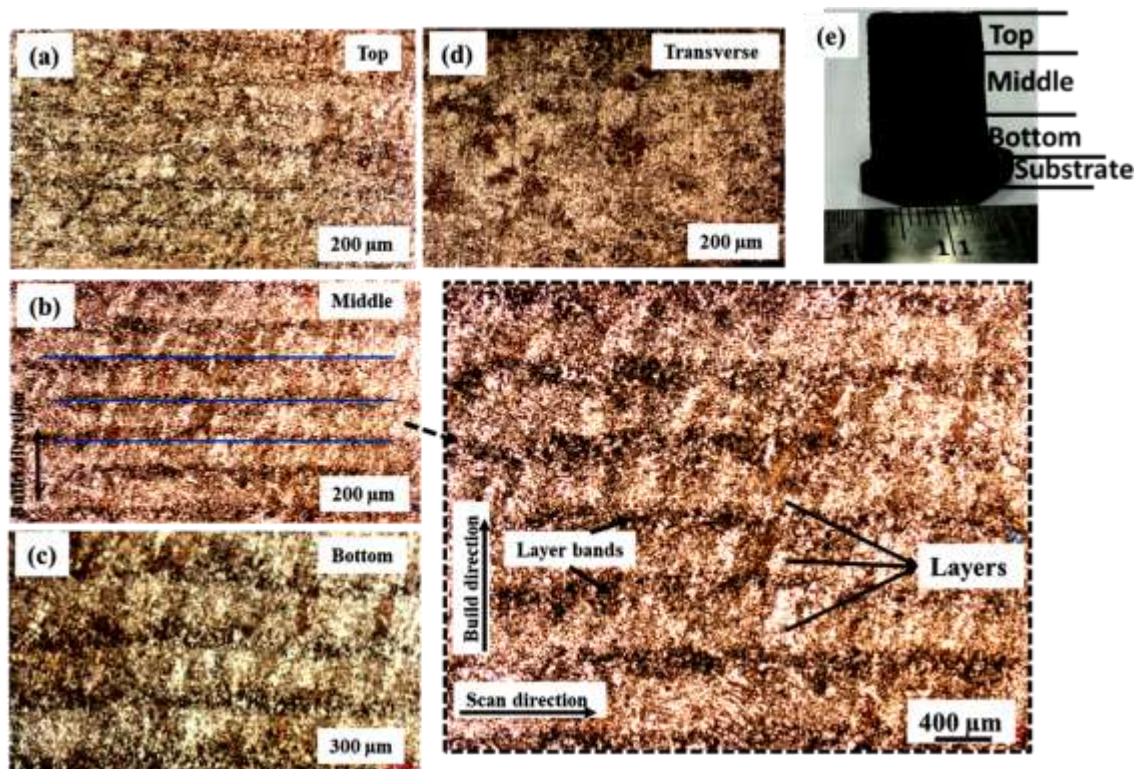
Figure 6.19 Optical microscope images of different regions of the γ-TiAl sample
(a) Top (b) Middle (c) Bottom (d) Transverse and (e) Thin-wall

Figure 6.19 presents the optical micrographs of an as-deposited γ-TiAl alloy at 200-10 process condition. All the micrographs presented here show a dendritic fine grain structure with a relatively non-homogeneous microstructure. In all the micrographs of

Figure 6.19, the regions of light contrast are the $\alpha_2+\gamma$ phase, which has a lamellar structure and the regions of dark contrast is the γ-TiAl phase. This kind of morphology is in agreement with that reported in the existing literature (Srivastava et al. 1999; Zhang et al. 2001). The lamellar grains are oriented in the build direction. This orientation can be attributed to the unidirectional flow of heat that occurs during the deposition of successive layers in the LMD process. Figure 6.19 (a) shows the microstructure in the top region of the deposited thin-wall. This micrograph shows a refined structure that can be attributed to the reheating of the previously deposited layers and the conduction of excess thermal energy to the substrate (Tlotleng 2018). Figure 6.19 (b) and (c) show the microstructure at the middle and bottom regions of the deposited thin-wall. These micrographs also display a fine structure with epitaxial growth of grains along the build direction. The transverse section morphology is shown in Figure 6.19 (d). In the transverse direction, the structure also displays same phases ($\alpha_2+\gamma$ and γ-TiAl). This microstructure changes in the thin-wall regions can be attributed to the high cooling rates and in situ cyclic heat treatment of the layers (Tlotleng 2018; Yang et al. 2016).

Figure 6.20 BSE images showing microstructure of LMD deposited γ-TiAl alloy thin-walls for (a) 200-8, (b) 200-10, and (c) 200-12

The microstructure of the middle surface of the as-deposited sample for different process conditions are reported in Figure 6.20. The BSE (Back Scattered Electrons) images reveal massive γ and $\alpha_2 + \gamma$ phases in all the samples. The $\alpha_2 + \gamma$ phase has Al content between ~36-51 (at%.) and the phase is formed as a result of cooling from α phase ($\alpha \rightarrow \alpha+\gamma \rightarrow \alpha_2 +\gamma$). The α_2 phase has low ductility but exhibits good high-temperature strength. But α_2 phase has a high absorption rate of oxygen and hydrogen, leading to embrittlement at high working temperatures (Bird et al. 2004; Ma et al. 2015; Sarkar et al. 2009). The γ-TiAl phase has Al composition between ~46-65 (at. %). The γ phase has a face-centered tetragonal $L1_0$ structure and the c/a ratio for the stoichiometric composition is around 1.02 (Ma 2015). Since lattice parameters a and c show a linear dependence on Al %, the distortion of tetragonality increases with increase in Al composition. The γ phase maintains long-range ordering up to its melting point (1460 °C). An important property of γ phase is its excellent oxidation resistance. Also, it has a low hydrogen absorption rate, unlike the α_2 phase (Ma 2015). However, it exhibits no ductility at room temperature; thereby processing it is challenging. The two-phase titanium aluminide exists with a γ and α_2 phases having Al between 37-49 (at%.). Hence percentage of Al is more prominent in deciding mechanical properties for structural applications.

It can be seen from Figure 6.20, that fine lamellar and massive γ-TiAl grains are distributed on the surface of the samples. Irregular shaped γ laths were found to precipitate at the grain boundaries (Ma et al. 2015). Whereas fully lamellar with different colony sizes consisting of γ and α_2 phases were observed (Figure 6.20). A fine lamellar structure is formed as a result of higher cooling rates (Franzen 2010). Balla et al. (2016) reported similar microstructures during LMD of γ-TiAl alloys.

In conventional techniques, a fully lamellar microstructure with coarse grain size is obtained (Kothari et al. 2012). The LMD process produces lamellar structure with a smaller grain size (Balla et al. 2016). It was found that the size of the lamellar grains was between 12-60 µm, which resulted in improved ductility (Wang et al. 2002). Figure 6.21 (a), (b), and (c) shows the SEM images of the middle surface of the as-deposited sample for different process conditions. These micrographs also confirm the presence of lamellar and massive γ phases. As can be seen from SEM images of Figure 6.21 and

77

Figure 6.22, the microstructure of the samples processed at different conditions show identical phases.

Furthermore, microstructural refinement is noticed as the laser power decreases from 300 to 200 W at a constant travel speed of 10 mm/s (Figure 6.22). This can be attributed to higher cooling rates with a decrease in laser power (Balla et al. 2016; Zhang et al. 2001).

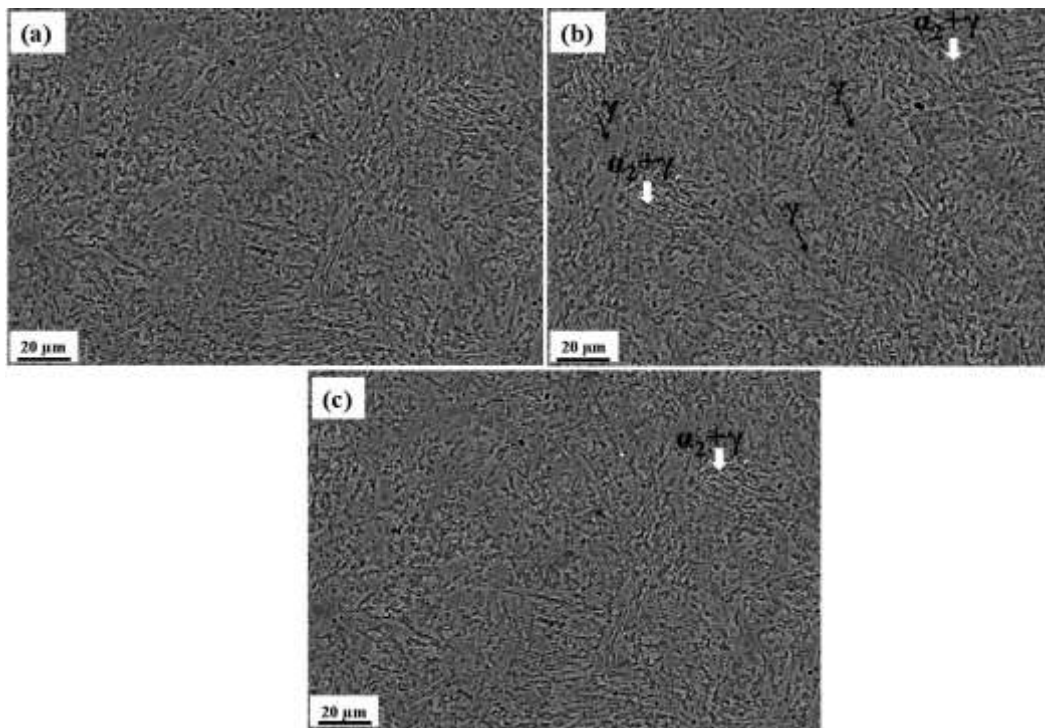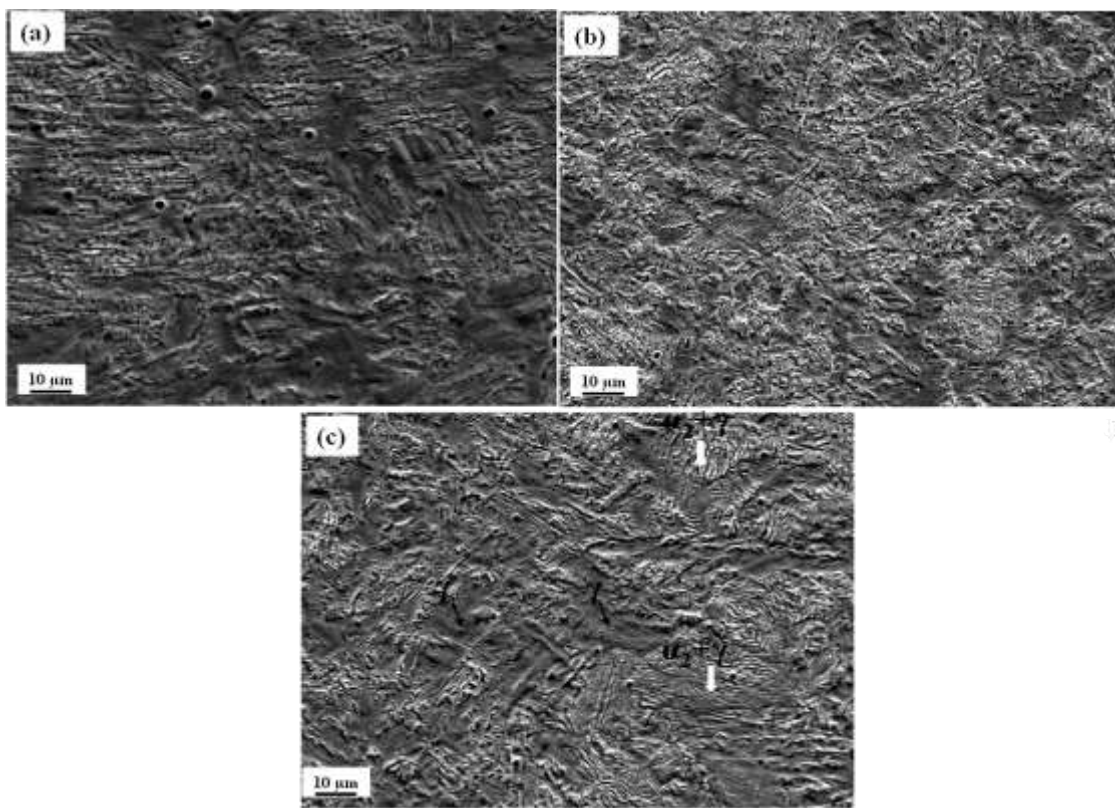Figure 6.21 SEM images showing microstructure of LMD deposited γ-TiAl alloy thin-walls for (a) 200-8, (b) 200-10, and (c) 200-12
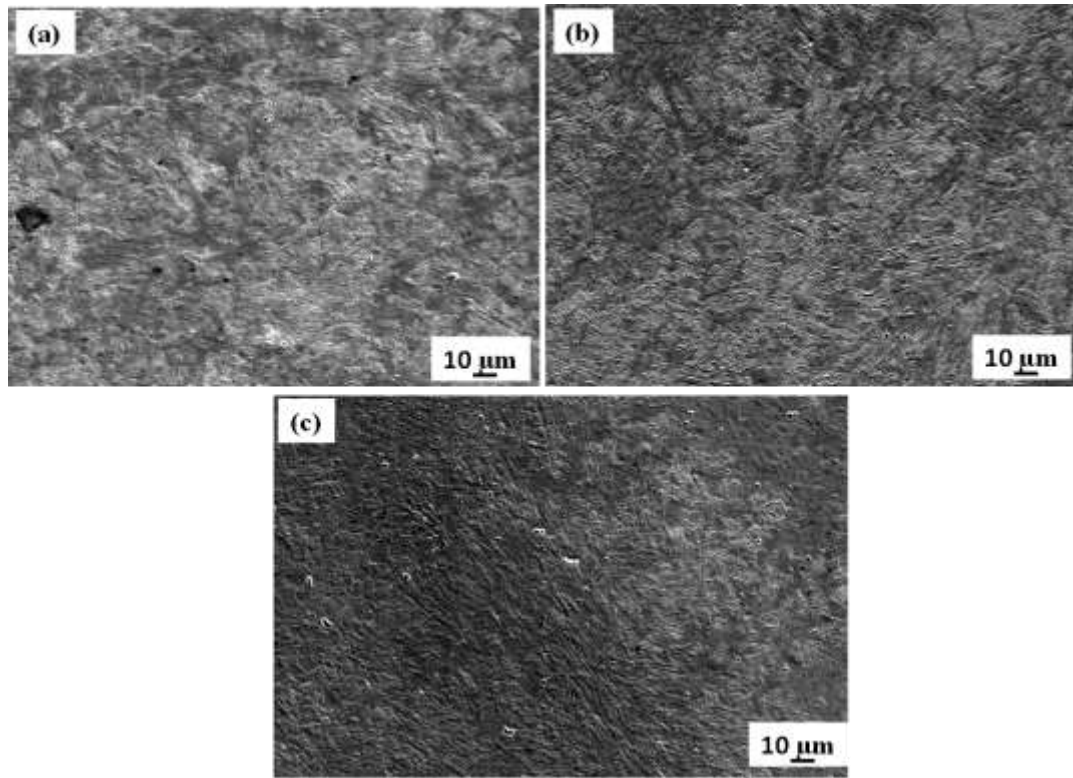
Figure 6.22 SEM images showing microstructure of LMD deposited γ-TiAl alloy thin-walls for (a) 300-10, (b) 250-10, and (c) 200-10

6.2.8   Phase analysis

The phase constituents of the solid samples were determined using XRD and are presented in Figure 6.23. The solid samples primarily consist of γ-TiAl and a small amount of α_2-Ti_3Al phase. In Figure 6.23, it can be observed that there is no difference in XRD peaks between solid samples deposited at different laser power and travel speed. The as-received powder showed a relatively high amount of α_2-Ti_3Al (refer to Figure 6.16 d). The fraction of α_2-Ti_3Al was found to decrease in the solid samples, which could be attributed to the microstructural transformation that occurred in the solid samples (Mohammad et al. 2017). Further, the XRD results of the thin-walls also confirm the existence of a two-phase microstructure. These two phases, namely, α_2-Ti_3Al and γ-TiAl, were present at all processing conditions. The Ti_3Al phase was formed as a result of the solid-state phase transformation and high cooling rates (Balla et al. 2016). The volume fraction of the phases is influenced by the cooling rates and thermal cycles developed during deposition (Ma et al. 2014).
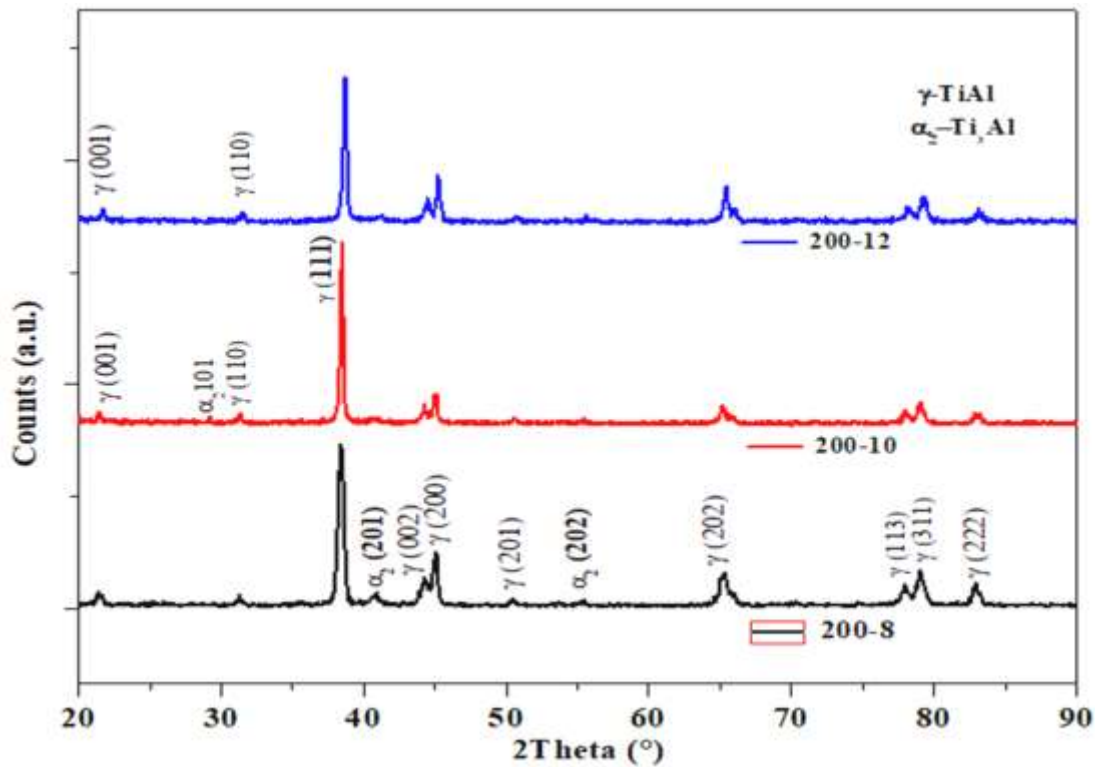
Figure 6.23 XRD diffraction spectra for LMD built thin-wall structures for various process conditions

6.2.9 Microhardness

Vickers microhardness is plotted along both the longitudinal, and build directions of the as-deposited samples and the results are shown in Figure 6.24. In Figure 6.24 (a), the hardness is plotted as a function of distance (from the left to the right edge) along the longitudinal direction at constant power (200 W) for different travel speeds (8, 10, and 12 mm/s). It was observed that the hardness values ranged from 323-420 HV along the longitudinal direction. In the build direction, the hardness values are plotted as a function of distance (from the top surface of the thin-wall towards the substrate) at constant power (P = 200 W) for different travel speeds (8,10, and12 mm/s). It can be observed that the hardness values are in the range of 331-431 HV along the build direction. These results indicate that the hardness value in the deposited wall decreases with the increase in the number of layers, i.e., maximum hardness occurs in regions nearer to the substrate. This can be attributed to the higher cooling rates in the initial

layers (refer section 6.1.6) due to rapid heat extraction by the substrate and also due to the higher fraction of α_2 phase in the initial layers (Ma et al. 2014; Qu and Wang 2007; Zhang et al. 2001).

Further, the average hardness values for the various travel speeds are shown in Figure 6.24 (c). It was observed that the hardness value increased (5%) slightly with the increase in travel speed due to the increase in cooling rates (refer section 6.1.6). The average hardness values for the various laser powers are shown in Figure 6.24 (d). It was observed that the hardness values decreased (4%) slightly with the increase in laser power due to the decrease in cooling rates.
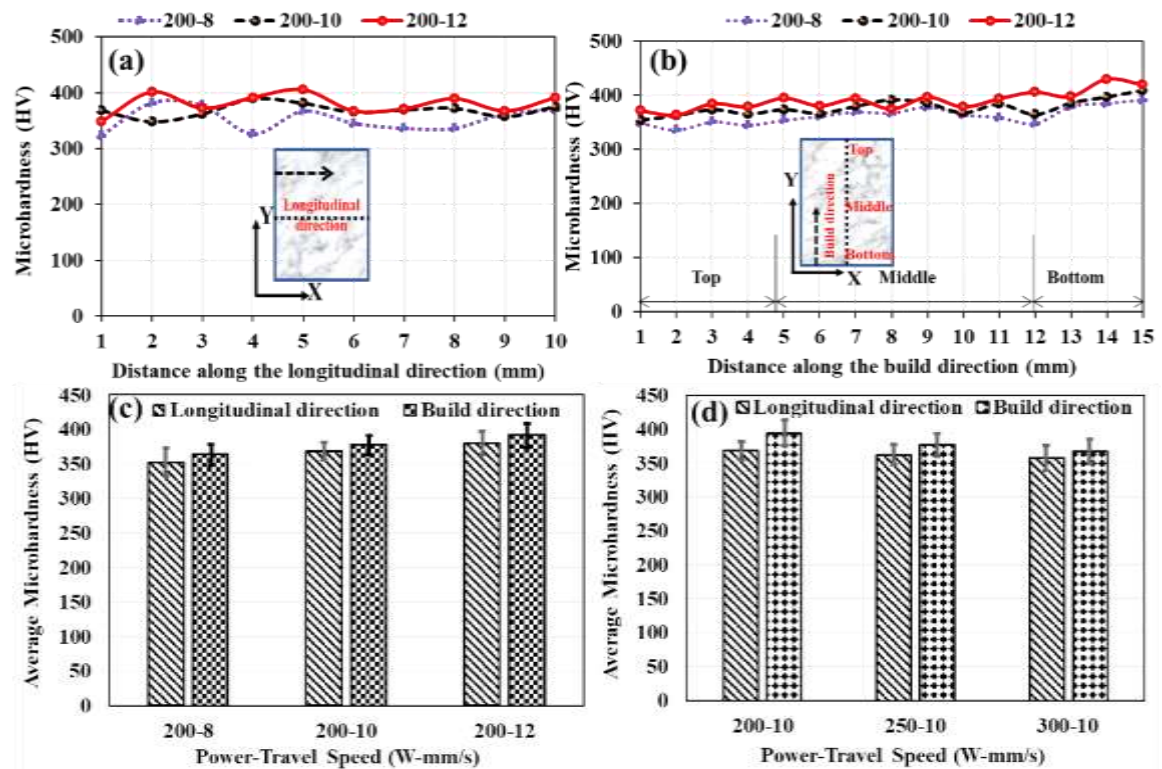
Figure 6.24 Microhardness of thin-walls along (a) Longitudinal (b) Build directions and (c), (d) Average microhardness

6.3 Summary of the chapter

This chapter presented the results of the numerical modeling and experimental study of laser metal deposited γ-TiAl alloy thin-wall structures. The following conclusions can be drawn from the chapter:

6.3.1 Numerical modeling results

- Thermal gradients increased with increase in the number of deposited layers, i.e., from the substrate to the last layer;

- Cooling rates decreased with increase in the number of deposited layers, i.e., from the substrate to the last layer;

- Along the build direction, tensile stresses were generated at the edges and compressive stresses were generated at the centre region of the thin-wall which increase with increase in distance from the substrate;

- Along the laser travel direction maximum compressive stresses were observed at the centre of the wall and these stresses decrease in magnitude with increase in distance from the centre;

- The state and magnitude of residual stress distribution in the thin-walls are attributed to the thermal gradients encountered during deposition.

6.3.2 Experimental results

- The trends of residual stress obtained from the numerical models were in decent agreement with experimental measurements;

- Microstructure of as-deposited samples showed fine lamellar structure comprising of γ and α_2 phases in agreement with published literature;

- The XRD study revealed the presence of the γ and α_2 phases found in the microstructural analysis; and

- The hardness values were found to decrease with the increase in wall height. Further, the hardness values increased marginally (5%) with the increase in travel speed.

CHAPTER 7

7   LASER METAL DEPOSITION OF γ-TiAl PLATE GEOMETRIES

In this chapter, the work was further extended to understand thermal behaviour and residual stresses during laser deposition of multitrack and multilayer structures (plate geometry). To this end, this chapter presents the results of the numerical modeling of laser metal deposited γ-TiAl plate geometries. At the time of reporting, there has been no work reported in literature on the evolution of residual stress during LMD of γ-TiAl plate geometries. This work is a first attempt in understanding the evolution of residual stress in γ-TiAl plate geometries using computational modeling.

7.1   Transient thermomechanical analysis of the plate

The thermomechanical analysis was carried out for the plate geometry. The details of the FE model of the plate geometry are presented in Table 7.1.

Table 7.1 Details of plate dimensions and finite element model

Parameter	Details
Dimensions: Substrate (S) and plate	L30×W30×H6 mm^3(S) L20×W3×H0.5 mm^3(P)
Element size of the layer (L), substrate (S)	0.125 mm (L), 0.125 and 1.66 mm (S)
Type of element	Thermal SOLID70, Structural SOLID185
No. of nodes, elements	48248, 38820
No. of layers, layer height, length	2, 0.25 mm, 20 mm
No. of tracks, Width of each track,	6, 0.5 mm
Laser beam diameter and overlap percentage	0.5 mm, 0%
Scanning patterns	Bidirectional, Unidirectional

7.1.1   Description of FE model

The dimensions of the plate geometry were length = 20 mm, width = 3 mm, and height = 0.5 mm. The plate was considered to be deposited on a substrate whose dimensions were length = 30 mm, width = 30 mm, and height = 5 mm. The FE model of the plate geometry is shown in Figure 7.1. The meshed FE model of the plate consisted of 48,248

nodes and 38,820 elements. During thermal analysis, fixed temperature (T = 25 °C) boundary condition was applied on the bottom face of the substrate. While in the structural analysis, all the degrees of freedom on the bottom face of the substrate were constrained to prevent the rigid body motion. Upon the completion of the simulations, melt pool dimensions, temperature cycles, magnitude, and distribution of residual stresses were extracted from the thermomechanical finite element models of the plate geometry.
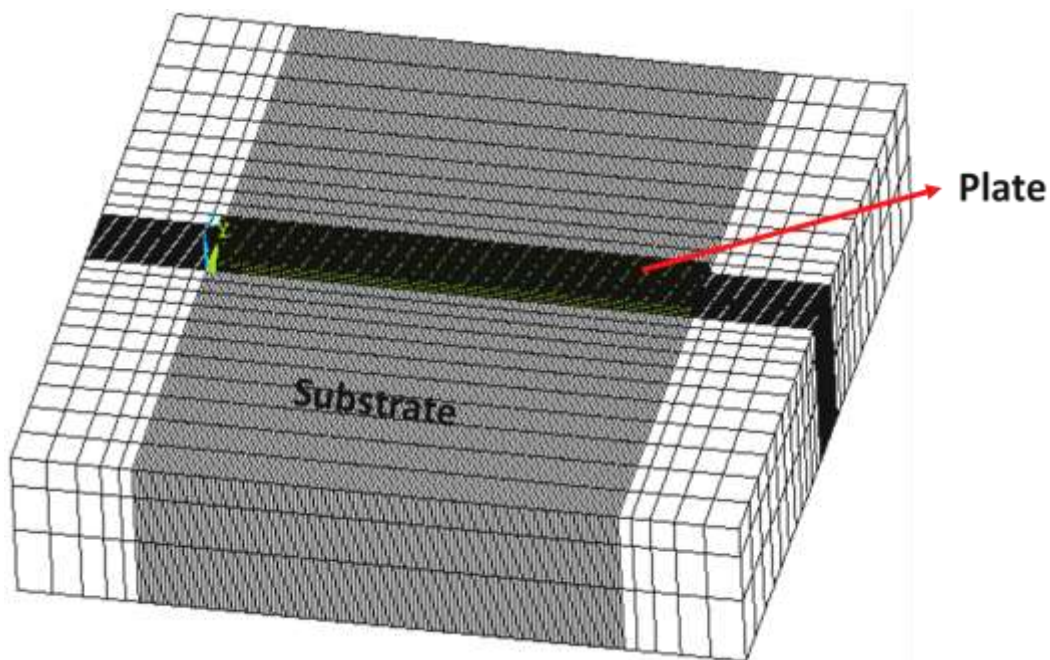
Figure 7.1 Isometric view of the finite element model of plate geometry built on a substrate

7.1.2 Melt pool dimensions

The melt pool contours were extracted from track 3 in layer 2 (i.e., the centre of the plate) are shown in Figure 7.2. The dimensions of the melt pool were extracted from these contours.
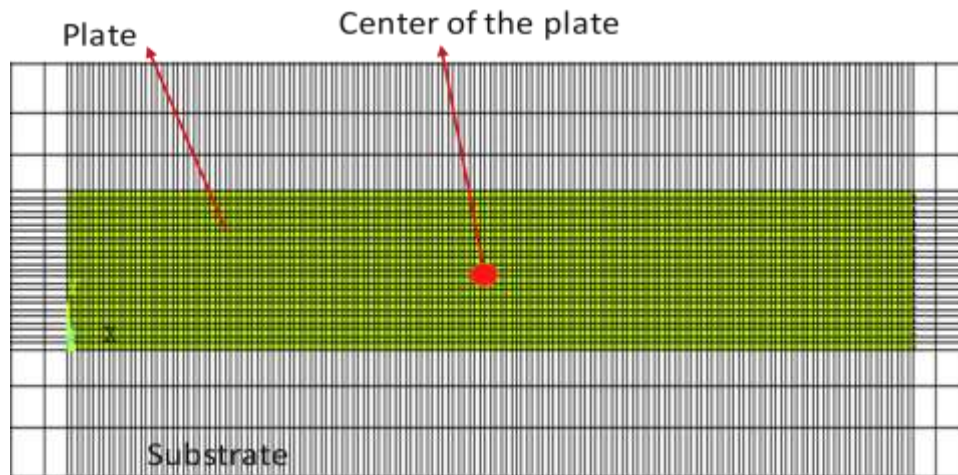
Figure 7.2 Illustration of the location from where melt pool dimensions were extracted

The contours of the melt pool (top and cross-sectional views) for varying laser power at constant travel speed are shown in Figure 7.3. In the contours, the red colour indicates the molten region where the temperatures were above the liquidus temperature (>1460 °C) of the material. The dimensions of the melt pool (length, width, and depth) for varying laser power at a constant travel speed of 15 mm/s are presented in Table 7.2. From this table, it can be observed that the melt pool dimensions (length, width, and depth) increased as the laser power was increase. The melt pool length increases from 0.425 mm to 0.55 mm, while depth increased from 0.1 to 0.29 mm and the width increased from 0.412 to 0.5 mm. This increase in melt pool dimensions with the increase in laser power can be attributed to the higher energy available at increasing powers to melt the powder.
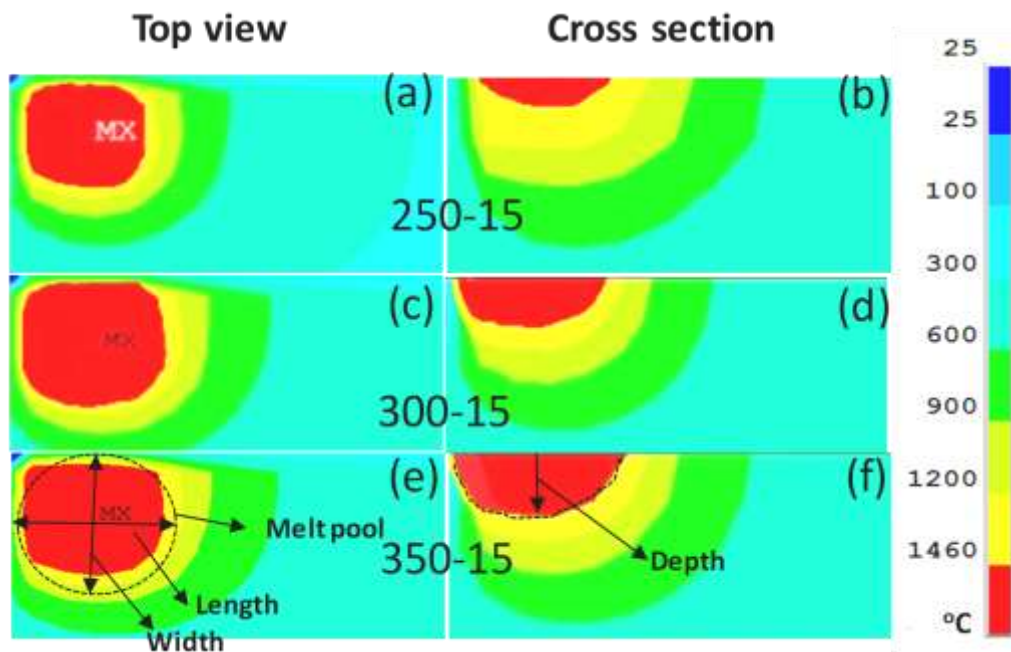
Figure 7.3 Top and cross-sectional view of the melt pool in track 3 and layer 2 at V = 15 mm/s and varying laser power a) and (b) 250 W; (c) and (d) 300 W; (d) and (e) 350 W
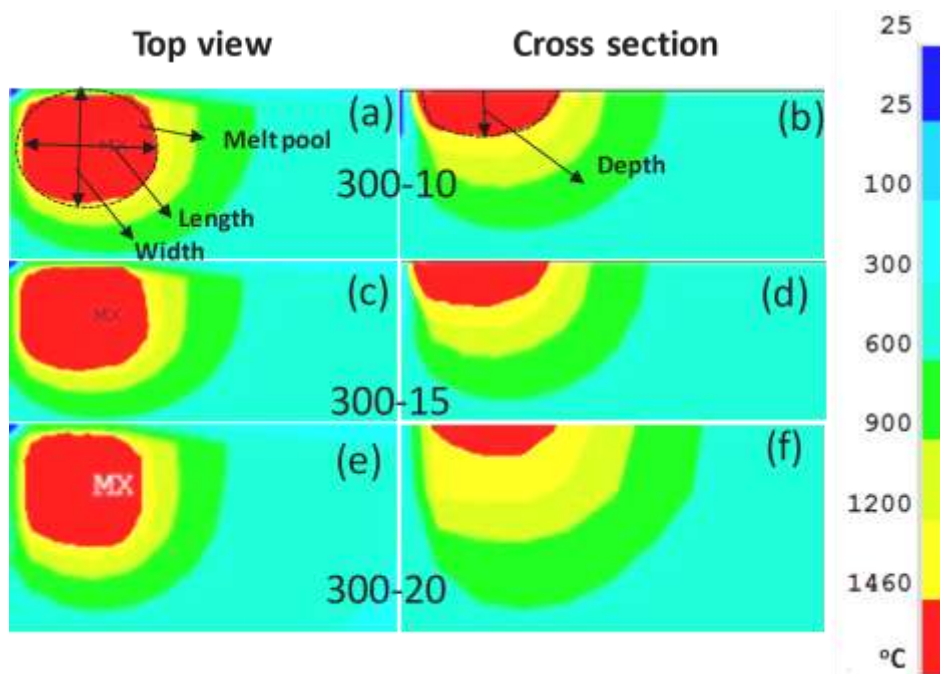
Figure 7.4 Top and cross-sectional view of the melt pool in track 3 and layer 2 at P = 300 W and varying travel speeds a) and (b) 10 mm/s; (c) and (d) 15 mm/s; (d) and (e) 20 mm/s

Table 7.2 Melt pool dimensions

Influence of laser power on melt pool dimensions (V = 15 mm/s)				
Laser power (W)	Energy density (J/mm^2)	Length (mm)	Width (mm)	Depth (mm)
250	33.33	0.425	0.4125	0.1
300	40.00	0.5	0.49	0.25
350	46.67	0.55	0.5	0.29
Influence of travel speed on melt pool dimensions (P = 300 W)				
Travel speed (mm/s)	Energy density (J/mm^2)	Length (mm)	Width (mm)	Depth (mm)
10	60	0.52	0.5125	0.3125
15	40	0.50	0.49	0.25
20	30	0.48	0.46	0.15

The contours of the melt pool (top and cross-sectional views) for varying travel speed at constant laser power are shown in Figure 7.4. The dimensions of the melt pool (length, width, and depth) for varying travel speed at constant laser power of 300 W are presented in Table 7.2.

From Table 7.2, it can be observed that the melt pool dimensions (length, width, and depth) decrease as the travel speed increase from 10 to 20 mm/s. The melt pool length decreased from 0.52 to 0.48 mm, while the width and depth decreased from 0.5125 to 0.46 mm and from 0.3125 to 0.15 mm respectively. This decrease in melt pool dimensions can be attributed to the decrease in energy density available to melt the powder with increasing travel speed. Further, it was observed that the top view (Figure 7.3 (a) (c) (e) and Figure 7.4 (a) (c) (e)) of melt pool contours resemble a cowboy hat pattern. This is due to the applied heat flux distribution, which follows the bell shape, i.e., TEM_{00} mode (Fu and Guo 2014; Luo and Zhao 2018).

7.1.3 Thermal cycling
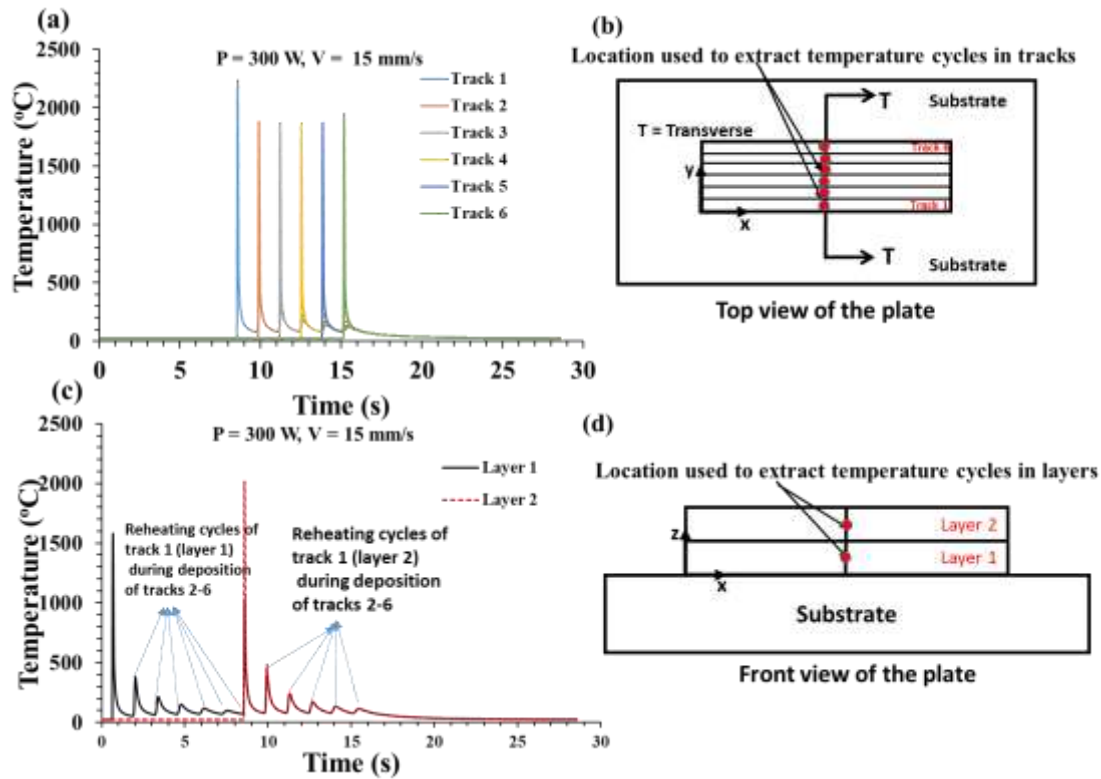
Figure 7.5 (a) and (b) Peak temperature cycling in tracks and locations used to extract temperatures of respective tracks, and (c) and (d) Peak temperature cycling in layers and locations used to extract temperatures of respective layers

The temperature profile of the six tracks as a function of time is plotted along the transverse direction (refer Figure 7.5 (a)) for bidirectional scanning. These temperatures were extracted at the centre of each track of the plate (x =10 mm and z = 0.5 mm) as shown in Figure 7.5 (b). From Figure 7.5 (a), it can be observed that the peak temperature in the plot is 2176 °C in track 1. The temperature then attains an uniform average temperature of 1826 °C in the middle tracks (2, 3, 4, and 5). However, in the last track (track 6), the temperature increases to 1899 °C. It can be seen that the edges experience a slightly higher temperature than the middle tracks and this may contribute to higher thermal gradients at the edges.

Table 7.3 Peak temperatures of layer 1, track 1 and layer 2, track 1 with reheating temperatures

Layer 1, Track 1						
Tracks	Track 1	Track 2	Track 3	Track 4	Track 5	Track 6
Temperature (°C)	1536	379	195	168	142	99
Layer 2, Track 1						
Temperature (°C)	1961	488	239	180	155	117

Figure 7.5 (c) shows the temperature profile in layers as a function of time for bidirectional scanning. The temperature profile was extracted (Figure 7.5 (d)) from the middle of each deposited layer. From Figure 7.5 (c), it can be observed that the peak temperature of track 1 is 1536 °C (layer 1), which is above the melting temperature of the material and hence, it is expected that the powder will melt during deposition. As the laser beam moves to the next location, track 1 starts to cool rapidly and reaches room temperature. However, due to the inherent nature of the LMD process, track 1 experiences a reheating cycle during the deposition of the neighbouring tracks (Table 7.3). It was found that the reheating temperature of track 1 was 379 °C, while track 2 is being deposited. Similarly, the temperature of track 1 keeps decreasing as the laser beam moves to deposit the subsequent tracks. The reheating temperature of track 1 was 195 °C, 168 °C, 142 °C, and 99 °C during the deposition of the successive tracks 3, 4, 5, and 6, respectively. Finally, track 1 attains room temperature after 28 secs after experiencing several reheating and cooling cycles. Similarly, layer 2 also undergoes similar heating and cooling cycles. It was noticed that there is a marginally higher temperature (Table 7.3) during the deposition of layer 2 due to decreased conduction of heat by the substrate. The successive building of layers reduces the heat sink effect of the substrate (Roberts et al. 2009).

7.1.4 Influence of laser power and travel speed on residual stress distribution in the plate

Table 7.4 presents the effect of laser power at constant travel speed on first Principal stress for bidirectional scan. The Principal stress increases from 196 to 237 MPa with

increase in laser power (250 to 350 W) at constant travel speed (15 mm/s). This is because the high laser power induces higher thermal gradients in the plate.

Similarly, the effect of travel speeds at constant laser power on first Principal stress for a bidirectional scan is shown in Table 7.5. The Principal stress slightly decreases from 239 to 215 MPa as the travel speed is increased from 10 to 20 mm/s at a constant laser power of 300 W. This is because the lower exposure time reduces the thermal gradients.

Table 7.4 Influence of laser power on first Principal stress

Influence of laser power (constant travel speed V = 15 mm/s)		
Laser power (W)	Energy density (J/mm^2)	Max. first Principal stress (MPa)
250	33.3	196
300	40	220
350	46.6	237

Table 7.5 Influence of travel speed on first Principal stress

Influence of travel speed (constant laser power P = 300 W)		
Travel speed (mm/s)	Energy density (J/mm^2)	Max. first Principal stress (MPa)
10	60	239
15	40	220
20	30	215

7.1.5 Comparison of laser scanning strategies

Residual stress distribution in build plate after cooling to room condition is discussed. Figure 7.6 (a) and (b) show first Principal stress contours for both unidirectional and bidirectional scans. The stress distribution is shown for laser power 300 W and travel speed 10 mm/s. Maximum Principal stress was found on the top surface and minimum stress was found at either edge of the plate.

Figure 7.6 (c) shows the numerical values of first Principal stress distribution along the laser travel direction. Magnitude of stress distribution for both scanning strategies is

almost the same. The maximum Principal stress was found in the core region of the plate with a magnitude of 136 MPa. This stress is lower than the yield strength of the material. The lowest Principal stress was near the edge of the plate. This decrease of residual stress at the edges can be attributed to the fact that edges are hotter than the interior (as observed in thermal simulation section 6.1.3), which causes strain mismatch between edge and core regions. Similar residual stress distribution has been reported in the literature (Moat et al. 2007; Rangaswamy et al. 2005).
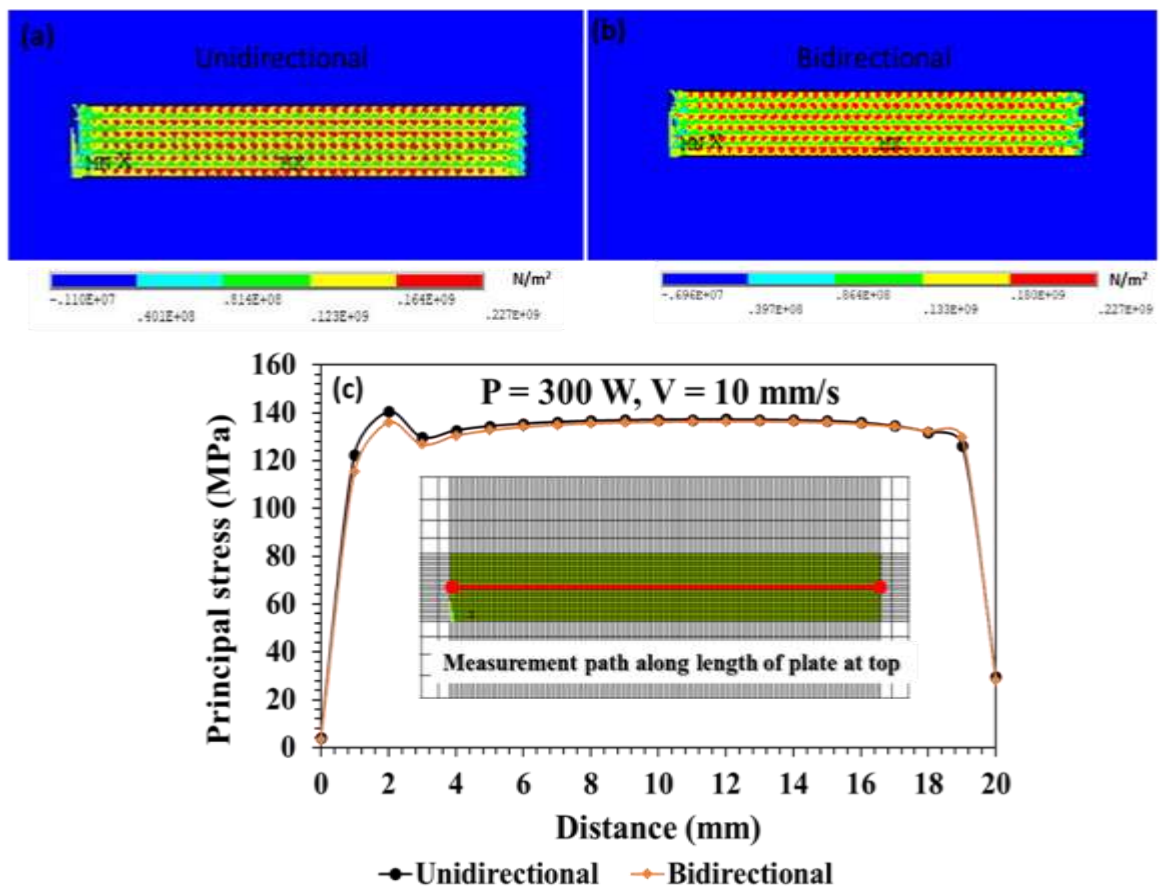
Figure 7.6 (a) First Principal stress contour for unidirectional scan pattern (b) First Principal stress contour for bidirectional scan pattern (c) Comparison of first Principal stress for unidirectional and bidirectional scan strategies

7.2 Summary of the chapter

- Melt pool dimensions (length, width, depth) increased as the laser power increased from 250 to 350 W and decreased as the travel speed increased from 10 to 20 mm/s.

- The edges of the plate experienced slightly higher temperatures (track 1-2176 ºC and track 6-1899 ºC) than the middle tracks.

- Maximum tensile residual stresses were observed in track 1 that are lower than the yield strength (400 MPa) of the material. The magnitude of these stresses decreased from track 2 to 6.

- Trends in residual stress were found to be independent of the scan strategies (Unidirectional and bidirectional) considered in this study.

.

CHAPTER 8

8   CONCLUSIONS AND FUTURE WORK

Residual stress-induced cracking is the primary obstacle to the widespread use of LMD processes for fabricating γ-TiAl components. Control of residual stress during LMD of γ-TiAl alloy has not yet been addressed in literature. Further, no work has been reported in literature wherein computational modeling has been utilized to provide insights into the effect of process variables on thermal conditions and residual stress evolution during LMD of γ-TiAl alloy. To this end, this thesis used a combination of computational modeling and experimental approaches to systematically investigate the effects of process variables on both thermal conditions and evolution of residual stresses during LMD of γ-TiAl alloy.

The value of the laser absorption coefficient (α_A) of γ-TiAl alloy that is required for computational modeling of LMD process was determined by carrying out a laser surface melting (LSM) study on EBM deposited γ-TiAl block. The LSM study also focused on the evolution of residual stresses as cracks were observed in the remelted region.

 Following conclusions were drawn from the laser surface melting study:

- The laser absorption coefficient of γ-TiAl alloy was determined to be $\alpha_A = 0.13$;
- The measured and predicted values of melt pool depth in the laser surface melted samples were in good agreement with a maximum error of 13.6%;
- Microcracks were observed in the remelted region of all the samples. These microcracks were attributed to high tensile stress, which exceeded the yield strength (400 MPa) of the material.

Following the determination of α_A using the LSM study, computational modeling of LMD γ-TiAl thin-wall and plate geometries were carried out. This computational study was complemented by experimental deposition of thin-wall geometries using LENS process which is a LMD technique.

Following conclusions were drawn from the computational modeling and experimental study of LMD γ-TiAl thin-wall structures:

- Thermal gradients increased with an increase in the number of deposited layers, i.e., from the substrate (6,614 ℃/mm) to the last layer (11,284 ℃/mm) for 200 W and 8 mm/s;

- The longitudinal direction has the maximum compressive stress of -301 ± 35.3 MPa at the thin-wall center. However, the minimum compressive stress is found at near ends of the wall. The compressive stress is -291.4 ± 37.5 MPa at the left end and -281 ± 29.5 MPa at the right end of the wall for 200 W and 8 mm/s;

- Along the build direction, with an increase in deposition height, measured compressive stress decreased. The maximum compressive stress of -309 ± 33.8 MPa at the near substrate and minimum compressive stress of -274.1 ± 28.6 MPa at the near topmost layer of the thin-wall for 200 W and 8 mm/s;

- Residual stress distribution obtained from the computational models is in good agreement with experimental measurements with a maximum error of 26% for P = 300 W and V = 10 mm/s;

- Microstructure of as-deposited samples showed fine lamellar structure comprising of γ and α_2 phases in agreement with published literature.

As of today, there has been no work reported in literature on the evolution of residual stress during LMD of γ-TiAl plate geometries. This work is a first attempt in understanding the evolution of residual stress in γ-TiAl plate geometries using computational modeling.

From this study, following conclusions were drawn:

- Melt pool dimensions (length, width, and depth) increased with increase in laser power (250-350 W) and decreased with increase in travel speed (10-20 mm/s);

- During deposition of a layer (which consisted of six tracks), maximum temperature (2176 ℃) in the melt pool was observed in track 1.

- Maximum tensile residual stresses were observed in track 1 that are lower than the yield strength (400 MPa) of the material. The magnitude of these stresses decreased from track 2 to 6;

- Trends in residual stress were found to be independent of the scan strategies (Unidirectional and bidirectional) considered in this study.

In summary, the computational modeling work reported herein can help in identify process parameters for LMD of defect-free γ-TiAl samples, thereby reducing the time and cost of experimentation.

Scope for future work

The primary focus of this research was to understand the effect of process variables on residual stress and microstructure in LMD γ-TiAl components. When this research work commenced, there was no prior literature available relating the deposition process variables to the magnitude and distribution of residual stress in LMD γ-TiAl components. To this end, the present work focused on utilizing thermomechanical finite element models to relate the deposition process variables to the evolution of residual stress during deposition of γ-TiAl components. The thermomechanical finite element model results were validated with experimental measurements of residual stress carried out on laser-deposited γ-TiAl thin-wall geometries. A decent agreement was seen between the predicted and measured residual stresses, thereby emphasizing on the utility of computational modeling to aid in reducing the time and cost of experimentation required to minimize residual stresses in LMD of γ-TiAl components. Despite the progress made in the current research, this work can be further extended. The following tasks have been identified as possible areas for future research:

- Future work can include the effect of fluid flow to understand evolution of microstructure;
- The thermo-mechanical models used in this work can also be extended to cylindrical and other complex geometries to understand the evolution of residual stress during their deposition using LMD process;
- The laser can be modeled as a 3D volumetric heat source to further improve the accuracy of prediction of the melt pool size and temperatures in both the melt pool as well as the heat-affected zone.

REFERENCES

Ahmad, B., Veen, S. V. D. V., Fitzpatrick, M. E., and Guo, H. (2018). "Measurement and modelling of residual stress in wire-feed additively manufactured titanium." *Mater. Sci. Technol.*, 34(18), 2250–2259.

Amine, T., Newkirk, J. W., and Liou, F. (2014). "An investigation of the effect of direct metal deposition parameters on the characteristics of the deposited layers." *Case Stud. Therm. Eng.*, 3(3), 21–34.

ANSYS. (2017a). "SOLID70 three dimensional thermal solid element". https://www.mm.bme.hu/~gyebro/files/ans_help_v182/ans_thry/thy_el70.html (Dec, 24. 2018).

ANSYS. (2017b). "SOLID185 three dimensional structural solid element." https://www.mm.bme.hu/~gyebro/files/ans_help_v182/ans_elem/Hlp_E_SOLID185.html (Dec, 24. 2018).

Appel, F., and Paul, D.H. and Oehring, M. (2011). *Gamma titanium aluminide alloys: Science and technology*. 12, 69469 Weinheim, Germany: Wiley-VCH Verlag GmbH & Co. KGaA.

Azarniya, A., Colera, X. G., Mirzaali, M. J., Sovizi, S., Bartolomeu, F., St Weglowski, M. k., Wits, W. W., Yap, C. Y., Ahn, J., Miranda, G., Silva, F. S., Madaah Hosseini, H. R., Ramakrishna, S., and Zadpoor, A. A. (2019). "Additive manufacturing of Ti–6Al–4V parts through laser metal deposition (LMD): Process, microstructure, and mechanical properties." *J. Alloys Compd.*, 804(2019), 163–191.

Balichakra, M., Bontha, S., Krishna, P., and Balla, V. K. (2019a). "Laser surface melting of γ-TiAl alloy an experimental and numerical modeling study." *Mater. Res. Express*, 6(4), 046543.

Balichakra, M., Bontha, S., Krishna, P., and Balla, V. K. (2019b). "Prediction and validation of residual stresses generated during laser metal deposition of γ titanium aluminide thin wall structures." *Mater. Res. Express*, 6(10), 106550.

Balichakra, M., Bontha, S., Krishna, P., Das, M., and Balla, V. K. (2016). "Understanding thermal behavior in laser processing of titanium aluminide alloys." *Proc. 6th Int. 27th All India Manuf. Technol. Des. Res. Conf.*, 73–77.

Balla, V. K., Das, M., Mohammad, A., and Al-ahmari, A. M. (2016). "Additive manufacturing of g -TiAl : processing, microstructure, and properties." *Adv. Eng. eaterials*, 18(7), 1–8.

Biamino, S., Penna, A., Ackelid, U., Sabbadini, S., Tassa, O., Fino, P., Pavese, M., Gennaro, P., and Badini, C. (2011). "Electron beam melting of Ti-48Al-2Cr-2Nb alloy: microstructure and mechanical properties investigation." *Intermetallics*, 19(6), 776–781.

Bird, R. K., Wallace, T. A., and Sankaran, S. N. (2004). "Development of protective coatings for high-temperature metallic materials." *J. Spacecr. Rockets*, 41(2), 213–220.

Bontha, S., Klingbeil, N. W., Kobryn, P. A., and Fraser, H. L. (2006). "Thermal process maps for predicting solidification microstructure in laser fabrication of thin-wall structures." *J. Mater. Process. Technol.*, 178(1–3), 135–142.

Carcel, B., Serrano, A., Zambrano, J., Amigo, V., and Carcel, A. C. (2014). "Laser cladding of TiAl intermetallic alloy on Ti6Al4V process optimization and properties." *Phys. Procedia*, 56(9), 284–293.

Castellanos, S. D., Cavaleiro, A. J., Jesus, A. M. P. D., Neto, R., and Alves, J. L. (2018). "Machinability of titanium aluminides: A review." *Proc. Inst. Mech. Eng. Part L J. Mater. Des. Appl.*, 233(3), 426–451.

Cegan, T., Szurman, I., Kursa, M., Holesinsky, J., and Vontorova, J. (2015). "Preparation of TiAl-based alloys by induction melting in graphite crucibles." *Kov. Mater.*, 53(2), 69–78.

Cormier, D., Harrysson, O., Mahale, T., and West, H. (2007). "Freeform fabrication of titanium aluminide via electron beam melting using prealloyed and blended powders." *Res. Lett. Mater. Sci.*, 2007(12), 1–4.

Dave, V., Matz, J., and Eagar, T. (1995). "Electron beam solid freeform fabrication of metal parts." *Solid Free. Fabr. Symp.*, 64–71.

Denlinger, E. R., Irwin, J., and Michaleris, P. (2014). "Thermomechanical modeling of additive manufacturing large parts." *J. Manuf. Sci. Eng.*, 136(6), 061007.

Dong, S., Chen, R., Guo, J., Ding, H., Su, Y., and Fu, H. (2014). "Microstructure and room temperature tensile property of as-cast Ti44Al6Nb1.0Cr2.0V alloy." *Trans. Nonferrous Met. Soc. China*, 25(4), 1097–1105.

Du, H., Liu, X. W., Li, J., Tao, P., Jiang, J., Sun, R., and Fan, Z. T. (2015). "Use of spark plasma sintering for fabrication of porous titanium aluminide alloys from elemental powders." *Mater. Manuf. Process.*, 31(6), 725–732.

Fallah, V., Alimardani, M., Corbin, S. F., and Khajepour, A. (2011). "Temporal development of melt-pool morphology and clad geometry in laser powder deposition." *Comput. Mater. Sci.*, 50(7), 2124–2134.

Filippini, M., Beretta, S., Patriarca, L., and Sabbadini, S. (2014). "Effect of the microstructure on the deformation and fatigue damage in a gamma TiAl produced by additive manufacturing." *TMS Proc. -The Miner. Met. Mater. Soc.*, 189–193.

Fitzpatrick, M.E., Fry, A.T., Holdway, P., Kandil, F.A., Shackleton, J., and Suominen, L. (2006). *Determination of Residual Stresses by X-ray Diffraction*. National Physical Laboratory, Middlesex, United Kingdom.

Foroozmehr, E., and Kovacevic, R. (2010). "Effect of path planning on the laser powder deposition process: Thermal and structural evaluation." *Int. J. Adv. Manuf. Technol.*, 51(5–8), 659–669.

Fu, C. H., and Guo, Y. B. (2014). "Three-dimensional temperature gradient mechanism in selective laser melting of Ti-6Al-4V." *J. Manuf. Sci. Eng.*, 136(6), 061004–1.

Gao, W., Zhang, Y., Ramanujan, D., Ramani, K., Chen, Y., Williams, C. B., Wang, C. C. L., Shin, Y. C., Zhang, S., and Zavattieri, P. D. (2015). "The status, challenges, and future of additive manufacturing in engineering." *Comput. Aided Des.*, 69(4), 65–89.

Griffith, M. ., Schlienger, M. ., Harwell, L. ., Oliver, M. ., Baldwin, M. ., Ensz, M. ., Essien, M., Brooks, J., Robino, C. ., Smugeresky, J. ., Hofmeister, W. ., Wert, M. ., and Nelson, D. . (1999). "Understanding thermal behavior in the LENS process." *Mater. Des.*, 20(2–3), 107–113.

Ina, Y., Stephen, G., Daniel, H., and Igor, Y. (2015). "Residual stress in SLM Ti6Al4V alloy specimens." *Mater. Sci. Forum*, 828–829(8), 305–310.

Jeje, S. O., Shongwe, M. B., Maledi, N., Olubambi, P. A., and Babalola, B. J. (2019). "Spark plasma sintering of Ti-48Al intermetallic using elemental powder." *Int. J. Adv. Manuf. Technol.*, 13(5), 3025–3032.

Joshi, V. A. (2006). *Titanium alloys*. CRC Press Taylor & Francis Group Broken Sound Parkway NW.

Kamara, A. M., Marimuthu, S., and Li, L. (2011). "A numerical investigation into residual stress characteristics in laser deposited multiple layer waspaloy parts." *J. Manuf. Sci. Eng.*, 133(3), 031013.

Katsuyuki Yoshikawa, T. K. and T. O. K. S. (1992). "Changes in oxygen contents of titanium aluminides by vacuum induction, cold crucible induction and electron beam melting." *ISIJ Int.*, 32(5), 616–624.

Kelly, T. J., Juhas, M. C., and Huang, S. C. (2003). "Effect of a B2/Gamma structure on the tensile properties of the cast gamma titanium aluminide Ti-48Al-2Cr-2Nb." *Scr. Metall. Mater.*, 29(11), 1409–1414.

Kemerling, B., Lippold, J. C., Fancher, C. M., and Bunn, J. (2018). "Residual stress evaluation of components produced via direct metal laser sintering." *Weld. World*, 62(3), 663–674.

Kothari, K., Radhakrishnan, R., and Wereley, N. M. (2012). "Advances in gamma titanium aluminides and their manufacturing techniques." *Prog. Aerosp. Sci.*, 55(7), 1–16.

Kun, Zhao Yong, Liu Lan, Huang Bin, Jian-be, Li Xiao-peng, Liang Yue-hui, H.

(2014). "Microstructure evolution of hot deformed powder metallurgy Ti-45Al-7-Nb-0.3W alloy during heat treatment." *chinese journals nonferrous Met.*, 24(10), 2506–2511.

Lapin, J. (2009). "TiAl-based alloys: Present status and future perspectives." *Metal*, 19(na), 1–12.

Lasalmonie, A. (2006). "Intermetallics: why is it so difficult to introduce them in gas turbine engines?" *Intermetallics*, 14(10–11), 1123–1129.

Levkulich, N. C., Semiatin, S. L., Gockel, J. E., Middendorf, J. R., DeWald, A. T., and Klingbeil, N. W. (2019). "The effect of process parameters on residual stress evolution and distortion in the laser powder bed fusion of Ti-6Al-4V." *Addit. Manuf.*, 28(1), 475–484.

Leyens, C., and Peter, M. (2003). *Titanium and titanium alloys*. Telford, London: WILEY-VCH Verlag GmbH & Co. KGaA, Weinheim.

Liu, H., Li, M., Qin, X., Huang, S., and Hong, F. (2018). "Numerical simulation and experimental analysis of wide-beam laser cladding." *Int. J. Adv. Manuf. Technol.*, 100(1–4), 237–249.

Liu, H., Sparks, T. E., Liou, F. W., and Dietrich, D. M. (2013). "Numerical analysis of thermal stress and deformation in multi-layer laser metal deposition processes." 577–591.

Liu, W., and Dupont, J. N. (2004). "Fabrication of carbide-particle-reinforced titanium aluminide-matrix composites by laser-engineered net shaping." *Metall. Mater. Trans. A Phys. Metall. Mater. Sci.*, 35(13), 1133–1140.

Loeber, L., Biamino, S., Ackelid, U., Sabbadini, S., Epicoco, P., Fino, P., and Eckert, J. (2011). "Comparison of selective laser and electron beam melted titanium aluminides." *22nd Annu. Int. Solid Free. Fabr. Symp. - An Addit. Manuf. Conf.*, na(na), 547–556.

Loretto, M. H., Hu, D., Huang, A., and Wu, X. (2005). "Heat treatment of cast TiAl-

based alloys." *Mater. Forum*, 29(na), 17–20.

Luo, C., Qiu, J., Yan, Y., Yang, J., Uher, C., and Tang, X. (2018). "Finite element analysis of temperature and stress fields during the selective laser melting process of thermoelectric SnTe." *J. Mater. Process. Technol.*, 261(4), 74–85.

Luo, Z., and Zhao, Y. (2018). "A survey of finite element analysis of temperature and thermal stress fields in powder bed fusion additive manufacturing." *Addit. Manuf.*, 21(12), 318–332.

Ma, Y. (2015). "Fabrication of gamma titanium aluminide alloys by gas tungsten arc welding-based additive layer manufacturing." University of Wollongong.

Ma, Y., Cuiuri, D., Hoye, N., Li, H., and Pan, Z. (2014). "Characterization of in-situ alloyed and additively manufactured titanium aluminides." *Metall. Mater. Trans. B Process Metall. Mater. Process. Sci.*, 45(6), 2299–2303.

Ma, Y., Cuiuri, D., Hoye, N., Li, H., and Pan, Z. (2015). "The effect of location on the microstructure and mechanical properties of titanium aluminides produced by additive layer manufacturing using in-situ alloying and gas tungsten arc welding." *Mater. Sci. Eng. A*, 631(17), 230–240.

Mahamood, R. M., Akinlabi, E. T., Shukla, M., and Pityana, S. (2013). "Characterizing the effect of laser power density on microstructure, microhardness, and surface finish of laser deposited titanium alloy." *J. Manuf. Sci. Eng.*, 135(6), 064502.

Manvatkar, V. D., Gokhale, A. A., Reddy, G. J., and Venkataramana, A. (2011). "Estimation of melt pool dimensions, thermal cycle, and hardness distribution in the laser-engineered net shaping process of austenitic stainless steel." *Metall. Mater. Trans. A*, 42(7), 4080–4087.

Missouri, R. (2012). "Modeling and verification of temperature distribution and residual stress in laser aided metal deposition process." *ISC-GRS*, na.

Moat, R. J., Pinkerton, A. J., Hughes, D. J., Li, L., Withers, P. J., and Preuss, M. (2007). "Stress distributions in multilayer laser deposited waspaloy parts measured using

neutron diffraction." *26th Int. Congr. Appl. Lasers Electro-optics*, na.

Moat, R. J., Pinkerton, A. J., Li, L., Withers, P. J., and Preuss, M. (2010). "Residual stresses in laser direct metal deposited waspaloy." *Mater. Sci. Eng. A*, 528(6), 2288–2298.

Mohammad, A., Al-Ahmari, A. M., Balla, V. K., Das, M., Datta, S., Yadav, D., and Janaki Ram, G. D. (2017). "In vitro wear, corrosion and biocompatibility of electron beam melted γ-TiAl." *Mater. Des.*, 133(11), 186–194.

Mohammadhosseini, A., Masood, S. H., Fraser, D., and Jahedi, M. (2012). "Residual stresses and deformations in electron beam melting process using finite element analysis." *Adv. Mater. Res.*, 576(10), 789–792.

Mukherjee, T., Zuback, J. S., Zhang, W., and Debroy, T. (2017). "Residual stresses and distortion in additively manufactured compositionally graded and dissimilar joints." *Comput. Mater. Sci.*, 143(2), 325–337.

Murr, L. E., Gaytan, S. M., Ceylan, A., Martinez, E., Martinez, J. L., Hernandez, D. H., Machado, B. I., Ramirez, D. a., Medina, F., Collins, S., and Wicker, R. B. (2009). "Characterization of titanium aluminide alloy components fabricated by additive manufacturing using electron beam melting." *Acta Mater.*, 58(5), 1887–1894.

Parry, L., Ashcroft, I. A., and Wildman, R. D. (2016). "Understanding the effect of laser scan strategy on residual stress in selective laser melting through thermo-mechanical simulation." *Addit. Manuf.*, 12(5), 1–15.

Paul, R., Anand, S., and Gerner, F. (2014). "Effect of thermal deformation on part errors in metal powder based additive manufacturing processes." *J. Manuf. Sci. Eng.*, 136(3), 031009.

Porter, J., Wooten, J., Harrysson, O., and Knowlson, K. (2011). "Digital manufacturing of gamma-TiAl by electron beam melting." *Mater. Sci. Technol. Conf. Exhib.*, 1434–1441.

Pratt, P., Felicelli, S. D., Wang, L., and Hubbard, C. R. (2008). "Residual stress

measurement of laser-engineered net shaping AISI 410 thin plates using neutron diffraction." *Metall. Mater. Trans. A Phys. Metall. Mater. Sci.*, 39(13), 3155–3163.

Qu, H. P., Li, P., Zhang, S. Q., Li, A., and Wang, H. M. (2009). "The effects of heat treatment on the microstructure and mechanical property of laser melting deposition γ-TiAl intermetallic alloys." *Mater. Des.*, 31(4), 2201–2210.

Qu, H. P., and Wang, H. M. (2007). "Microstructure and mechanical properties of laser melting deposited γ-TiAl intermetallic alloys." *Mater. Sci. Eng. A*, 466(1–2), 187–194.

Rangaswamy, P., Griffith, M. L., Prime, M. B., Holden, T. M., Rogge, R. B., Edwards, J. M., and Sebring, R. J. (2005). "Residual stresses in LENS ® components using neutron diffraction and contour method." *Mater. Sci. Eng. A*, 399(1), 72–83.

Rao, K. P., Prasad, Y. V. R. K., and Suresh, K. (2011). "Hot working behavior and processing map of a γ-TiAl alloy synthesized by powder metallurgy." *Mater. Des.*, 32(10), 4874–4881.

Roberts, I. A. (2012). "Investigation of residual stresses in the laser melting of metal powders in additive layer manufacturing." University of Wolverhampton.

Roberts, I. A., Wang, C. J., Esterlein, R., Stanford, M., and Mynors, D. J. (2009). "A three-dimensional finite element analysis of the temperature field during laser melting of metal powders in additive layer manufacturing." *Int. J. Mach. Tools Manuf.*, 49(12–13), 916–923.

Sammons, P. M., Bristow, D. A., and Landers, R. G. (2013). "Height dependent laser metal deposition process modeling." *J. Manuf. Sci. Eng.*, 135(5), 054501.

Sanna Fager Franzen, J. K. (2010). "γ-Titanium aluminide manufactured by electron beam melting." Chalmers University of Technology.

Sarkar, S., Datta, S., Das, S., and Basu, D. (2009). "Oxidation protection of gamma-titanium aluminide using glass-ceramic coatings." *Surf. Coatings Technol.*, 203(13), 1797–1805.

Sarkar, S., Mitra, S., and Bhattacharyya, B. (2005). "Parametric analysis and

optimization of wire electrical discharge machining of γ-titanium aluminide alloy." *J. Mater. Process. Technol.*, 159(3), 286–294.

Schajer, G. S. (2013). *Practical residual stress measurement methods*. West Sussex, PO19 8SQ, United Kingdom: A John Wiley & Sons, Ltd.

Schuster, J. C., and Palm, M. (2006). "Reassessment of the binary aluminum-titanium phase diagram." *J. Phase Equilibria Diffus.*, 27(3), 255–277.

Seidel, A., Davids, A., Polenz, S., Straubel, A., Maiwald, T., Moritz, J., Schneider, J., Marquardt, A., Saha, S., Riede, M., Lopez, E., Brueckner, F., and Leyens, C. (2019). "Surface modification of additively manufactured gamma titanium aluminide hardware." *J. Laser Appl.*, 31(2), 022517.

Semiatin, S. L., Gross, M. E., Matson, D. W., Bennett, W. D., Bonham, C. C., Ustinov, a. I., and Ballard, D. L. (2012). "Microstructure evolution and composition control during the processing of thin-gage metallic foil." *Metall. Mater. Trans. A Phys. Metall. Mater. Sci.*, 43(12), 4819–4834.

Sharman, A. R. C., Hughes, J. I., and Ridgway, K. (2018). "Characterisation of titanium aluminide components manufactured by laser metal deposition." *Intermetallics*, 93(11), 89–92.

Sheng, L.R. Wei-jun, L. Fei, X. Hua-bing, W. (2007). "Numerical simulation of the thermal behavior during laser metal deposition shaping technology." *Trans. nonferrous Met. Soc. china*, 18(3), 691–699.

Soleymani, A. (2015). "Thermal model for prediction of deposition dimension of a deposited nickel superalloy." *Int. J. Eng. Adv. Technol.*, 4(4), 191–196.

Srivastava, D. (2002). "Microstructural characterization of the γ-TiAl alloy samples fabricated by direct laser fabrication rapid prototype technique." *Bull. Mater. Sci.*, 25(7), 619–633.

Srivastava, D., Hu, D., Chang, I. T. H., and Loretto, M. H. (1999). "Influence of thermal processing route on the microstructure of some TiAl-based alloys." *Intermetallics*,

7(10), 1107–1112.

Tang, H. P., Yang, G. Y., Jia, W. P., He, W. W., Lu, S. L., and Qian, M. (2015). "Additive manufacturing of a high niobium-containing titanium aluminide alloy by selective electron beam melting." *Mater. Sci. Eng. A*, 636, 103–107.

Thomas, M., Malot, T., and Aubry, P. (2017). "Laser metal deposition of the intermetallic TiAl alloy." *Metall. Mater. Trans. A*, 48(6), 1–16.

Tlotleng, M. (2018). "Microstructural properties of heat-treated LENS in situ additively manufactured titanium aluminide." *J. Mater. Eng. Perform.*, 28(2), 701–708.

Vasinonta, A., Beuth, J. L., and Griffith, M. L. (2001). "A process map for consistent build conditions in the solid freeform fabrication of thin-walled structures." *J. Manuf. Sci. Eng. Trans. ASME*, 123(4), 615–622.

Voisin, T., Monchoux, J.-P., Durand, L., Karnatak, N., Thomas, M., and Couret, A. (2015). "An innovative way to produce γ-TiAl blades: Spark plasma sintering." *Adv. Eng. Mater.*, 17(10), 1408–1413.

Wang, G., Xu, L., Wang, Y., Zheng, Z., Cui, Y., and Yang, R. (2011). "Processing maps for hot working behavior of a PM TiAl alloy." *J. Mater. Sci. Technol.*, 27(10), 893–898.

Wang, J. N., Yang, J., Xia, Q., and Wang, Y. (2002). "On the grain size refinement of TiAl alloys by cyclic heat treatment." 329–331(6), 118–123.

Wang, L., Felicelli, S. D., and Craig, J. E. (2007). "Thermal modeling and experimental validation in the LENSTM process." *Proc. SFF*, 9–20.

Wang, L., Felicelli, S. D., and Pratt, P. (2008a). "Residual stresses in LENS-deposited AISI 410 stainless steel plates." *Mater. Sci. Eng. A*, 496(1), 234–241.

Wang, L., Felicelli, S., Gooroochurn, Y., Wang, P. T., and Horstemeyer, M. F. (2008b). "Optimization of the LENS® process for steady molten pool size." *Mater. Sci. Eng. A*, 474(1–2), 148–156.

Wang, Z., Denlinger, E., Michaleris, P., Stoica, A. D., Ma, D., and Beese, A. M. (2017). "Residual stress mapping in Inconel 625 fabricated through additive manufacturing: Method for neutron diffraction measurements to validate thermomechanical model predictions." *Mater. Des.*, 113(10), 169–177.

Wimler, D., Lindemann, J., Clemens, H., and Mayer, S. (2019). "Microstructural evolution and mechanical properties of an advanced γ-TiAl based alloy processed by spark plasma sintering." *Materials (Basel).*, 12(9), 1–12.

Withers, P. J., and Bhadeshia, H. K. D. H. (2001). "Residual stress. Part 2 – Nature and origins." *Mater. Sci. Technol.*, 17(4), 366–375.

Xia, M., Gu, D., Yu, G., Dai, D., Chen, H., and Shi, Q. (2016). "Influence of hatch spacing on heat and mass transfer, thermodynamics and laser processability during additive manufacturing of Inconel 718 alloy." *Int. J. Mach. Tools Manuf.*, 109(7), 147–157.

Yan, L., Li, W., Chen, X., Zhang, Y., Newkirk, J., Liou, F., and Dietrich, D. (2016). "Simulation of cooling rate effects on Ti-48Al-2Cr-2Nb crack formation in direct laser deposition." *Proc. 27th Annu. Int. Solid Free. Fabr. Symp. Addit. Manuf. Conf.*, 680–690.

Yang, G., Jia, W., Zhao, P., Jia, L., Liu, N., Wang, J., and Tang, H. (2016). "Microstructures of as-fabricated and post heat treated Ti-47Al-2Nb-2Cr alloy produced by selective electron beam melting (SEBM)." *Rare Met. Mater. Eng.*, 45(7), 1683–1686.

Ye, R., Smugeresky, J. E., Zheng, B., Zhou, Y., and Lavernia, E. J. (2006). "Numerical modeling of the thermal behavior during the LENS ® process." *Mater. Sci. Eng.*, 428(4), 47–53.

Yilbas, B. S., Karatas, C., Arif, A. F. M., and Abdul Aleem, B. J. (2011). "Laser control melting of alumina surfaces and thermal stress analysis." *Opt. Laser Technol.*, 43(4), 858–865.

Yin, H., Wang, L., and Felicelli, S. D. (2008). "Comparison of two-dimensional and

three-dimensional thermal models of the LENS ® process." *J. Heat Transfer*, 130(10), 1–7.

Zekovic, S., Dwivedi, R., and Kovacevic, R. (2005). "Thermo-structural finite element analysis of direct laser metal deposited thin-walled structures." *Solid Free. Fabr.*, 338–355.

Zhang, A., Qi, B., Shi, B., and Li, D. (2015). "Effect of curvature radius on the residual stress of thin-walled parts in laser direct forming." *Int. J. Adv. Manuf. Technol.*, 79(1), 81–88.

Zhang, X. D., Brice, C., Mahaffey, D. W., Zhang, H., Schwendner, K., Evans, D. J., and Fraser, H. L. (2001). "Characterization of laser-deposited TiAl alloys." *Scr. Mater.*, 44(10), 2419–2424.

Zhao, H., Zhang, G., Yin, Z., and Wu, L. (2011). "Three-dimensional finite element analysis of thermal stress in single-pass multi-layer weld-based rapid prototyping." *J. Mater. Process. Technol.*, 212(1), 276–285.

Zyl, V.I., Yadroitsava, I., Yadroitsev, I. (2016). "Residual stress in Ti6Al4V objects produced by direct metal laser sintering." *South African J. Ind. Eng.*, 27(4), 134–141.

LIST OF PUBLICATIONS

S. No.	Title of the paper	Authors (in the same order as in the paper. Underline the Research Scholar's name)	Name of the Journal/ Conference, Vol., No., Pages	Month, Year of Publication	Category *
1.	Laser surface melting of γ-TiAl alloy an experimental and numerical modeling study	**Mallikarjuna Balichakra**, Srikanth Bontha, Prasad Krishna and Vamsi Krishna Balla	Material Research Express (IOP Science, **1.929, SCIE, SCOPUS**)	January 2019	1
2.	Prediction and validation of residual stresses generated during laser metal deposition of γ titanium aluminide thin wall structures	**Mallikarjuna Balichakra,** Srikanth Bontha, Prasad Krishna and Vamsi Krishna Balla	Material Research Express (IOP Science, **1.929, SCIE, SCOPUS**)	August 2019	1
3.	Numerical modelling of laser additive manufacturing processes.	Barsha Hazarika, **Mallikarjuna Balichakra,** Prasad Krishna, Vamsi Krishna Balla, Srikanth Bontha	NAFEMS Conference on Engineering Analysis, Modeling, Simulation and 3D-Printing Nimhans convention center, Bangalore, India	August 2016	3
4.	Understanding thermal behavior in laser processing of titanium aluminide alloys.	**Mallikarjuna Balichakra,** Prasad Krishna, Vamsi Krishna Balla, Mitun Das and Srikanth Bontha	6th International and 27th All India Manufacturing, Technology, Design and Research conference (AIMTDR), Pune India	December 2016	3

No.					
5.	Numerical modelling of residual stress in direct metal deposition of Ti6Al4V alloy.	**Mallikarjuna Balichakra,** Prasad Krishna, Vamsi Krishna Balla, Mitun Das and Srikanth Bontha	71st Annual Technical Meeting and International Symposium on Lightweighting for Defence, Aerospace, and Transportation, held at BITS Pilani, Goa, India	November 2017	4
6.	Thermomechanical finite element analysis of direct metal deposition process	**Mallikarjuna Balichakra,** Prasad Krishna, Vamsi Krishna Balla, Mitun Das and Srikanth Bontha	International Conference on Digital Fabrication 3D Printing, Industry 4.0 and beyond, held at IIT Hyderabad campus, India	March 2018	4

*Category: 1: Journal paper, full paper reviewed 2: Journal paper, Abstract reviews 3: Conference/Symposium paper, full paper reviewed
4: Conference/Symposium paper, abstract reviewed 5: others (including papers in Workshops, NITK Research Bulletins, Short notes etc.)

Mallikarjuna

Research Scholar

Name & Signature with Date

Dr. Srikanth Bontha

Research Guide

Name & Signature with Date

Prof. Prasad Krishna

Research Guide

Name & Signature with Date

BIO-DATA

1. **Name** : Mallikarjuna

2. **Father's Name** : Nagappa

3. **Date of Birth** : 5th September 1986

4. **Nationality** : Indian

5. **Marital Status** : Unmarried

6. **Address** : Department of Mechanical Engineering

      National Institute of Technology Karnataka

      Surathkal, P.O. Srinivasnagar-575 025

      Karnataka, India.

7. **Mobile Number** : +91-8310405141

8. **E-mail id.** : *mallubalichakra@gmail.com*

9. **Educational Qualification:**

Qualification	University/Institute	Year of Passing
Ph.D. (Mechanical Engineering)	National Institute of Technology Karnataka, Surathkal (India)	Pursuing
M.Tech. (Mechanical Engineering)	M.S. Ramaiah Institute of Technology, Bengaluru, Karnataka (India)	2013
B.E. (Mechanical Engineering)	Khaja Bandanawaz College of Engineering, Kalaburagi, Karnataka (India)	2011